

**FINITE ELEMENT MODELING
OF RESIDUAL STRESSES
IN ELECTROSLAG BUTT WELDS**

Final Report

SPR 356



Oregon Department of Transportation

**FINITE ELEMENT MODELING
OF RESIDUAL STRESSES
IN ELECTROSLAG BUTT WELDS**

Final Report

SPR 356

by

David Atteridge, M. Becker, K. Khan, L. Meekisho
B. Tahmasebi, and L. Zhang

Oregon Graduate Institute of Science and Technology
Department of Materials Science and Engineering
Portland, OR 97291-1000

for

Oregon Department of Transportation
Research Group
200 Hawthorne SE, Suite B-240
Salem, OR 97301-5192

and

Federal Highway Administration
400 Seventh Street SW
Washington, DC 20590

March 2000

1. Report No. FHWA-OR-RD-00-12		2. Government Accession No.		3. Recipient's Catalog No.	
4. Title and Subtitle FINITE ELEMENT MODELING OF RESIDUAL STRESSES IN ELECTROSLAG BUTT WELDS				5. Report Date March 2000	
				6. Performing Organization Code	
7. Author(s) David Atteridge, M. Becker, K. Khan, L. Meekisho, B. Tahmasebi, and L. Zhang Oregon Graduate Institute of Science and Technology Department of Materials Science and Engineering P.O. Box 91000, Portland, OR 97291-1000				8. Performing Organization Report No.	
9. Performing Organization Name and Address Oregon Department of Transportation Research Group 200 Hawthorne SE, Suite B-240 Salem, OR 97301-5192				10. Work Unit No. (TRAVIS)	
				11. Contract or Grant No. SPR 356	
12. Sponsoring Agency Name and Address Oregon Department of Transportation Federal Highway Administration Research Group and 400 Seventh Street SW 200 Hawthorne SE, Suite B-240 Washington, CD 20590 Salem, OR 97301-5192				13. Type of Report and Period Covered Final Report	
				14. Sponsoring Agency Code	
15. Supplementary Notes					
16. Abstract Shop fabricated electroslag (ES) welds used in bridge construction have had a history of low toughness in the fusion and heat affected zones. In addition, conventional inspection of ES weldments under shop fabrication conditions fail to consistently detect and/or correctly size weld discontinuities. These problems have led to a Federal Highway Administration requirement for removal, re-enforcement, or re-evaluation of the integrity of ES weldments in existing Federal bridges. This study was initiated in partial response to this requirement by the Oregon Department of Transportation. The specific tasks of this study were: a) to develop an understanding of ES weld-induced residual stresses for A36 steel with an emphasis on assessment of bridge-specific weld parameters and residual stress measurement; and b) computational modeling of ES welding and the resultant stress distribution. The ES weldments assessed in this study were those used in the fabrication of the Oregon State I-205 West Linn Bridge. This research was performed by numerical modeling based on unknown welding operation parameters. Experimental assessment of fusion zone characteristics was used as input data for the computational modeling work. Selective etching techniques were used to reveal the solidification bands formed at the fusion line interface during ESW. Analysis of these solidification bands allowed determination of weld pool profiles formed during welding, which are a direct function of the welding parameters. The results indicated that the operation procedures for all of the assessed ES welds were nominally the same. Two-dimensional (2D) and three-dimensional (3D) models were developed using FEA methods to simulate the ESW process and to analyze the effect of operating conditions on residual stress distribution. Both Lagrangian (stationary) and Eulerian (moving) coordinate systems were assessed in the FEA analysis. Modeling using Eulerian coordinates was found to be 100 over times more efficient than Lagrangian coordinates. Thus all 3D thermal-mechanical modeling was done using Eulerian coordinates. Both two-dimension (2D) and three-dimension (3D) thermal heat transfer ESW finite element analysis (FEA) models were developed using the Lagrangian system, only 3D thermal models were developed using the Eulerian coordinate systems. The thermal modeling effort included accounting for the latent heat of solidification. All 3D model results were in agreement, and agreed with experimentally determined ESW-induced thermal histories previously measured at the Oregon Graduate Institute. The weld-induced transient temperature fields predicted by the thermal heat transfer models were used as input into the Lagrangian Coordinate 2D mechanical two dimensional analysis and into the Eulerian mechanical three dimensional analysis of the thermally-induced mechanical response resulting in estimation ES weld-induced residual stresses. The 3D modeling using Eulerian coordinates predicts low tensile or compressive residual stresses are present in the as-welded ESW condition. The 2D Lagrangian coordinate system modeling predicts yield strength or greater tensile residual stresses. Thus 2D modeling was found to give incorrect residuals stress predictions and should not be used to predict ESW-induced residual stresses. Experimental assessment of bridge-specific residual stress fields was attempted. Coring and subsequent sectioning techniques were used to measure residual stresses associated with the ES weldments. However, the presence of continuous fusion line weld repairs perturbed the underlying ESW residual stress field. Thus, even though the results tend to support the 3D FEA residuals stress analysis, the experimental results can not be used to validate or invalidate the computational results. Surface residual stress assessment by the blind hole drilling method was unsuccessful.					
17. Key Words Electroslag welds, ESW, ES wealds, residual stress, finite element analysis, FEA, A36 steel, butt welds, modeling, heat transfer, bridges			18. Distribution Statement Copies available from NTIS		
19. Security Classification (of this report) unclassified		20. Security Classification (of this page) Unclassified		21. No. of Pages 146	22. Price

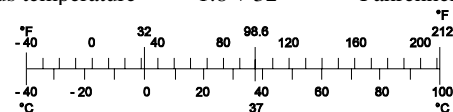
SI* (MODERN METRIC) CONVERSION FACTORS

APPROXIMATE CONVERSIONS TO SI UNITS

Symbol	When You Know	Multiply By	To Find	Symbol
<u>LENGTH</u>				
in	inches	25.4	millimeters	mm
ft	feet	0.305	meters	m
yd	yards	0.914	meters	m
mi	miles	1.61	kilometers	km
<u>AREA</u>				
in ²	square inches	645.2	millimeters squared	mm ²
ft ²	square feet	0.093	meters squared	m ²
yd ²	square yards	0.836	meters squared	m ²
ac	acres	0.405	hectares	ha
mi ²	square miles	2.59	kilometers squared	km ²
<u>VOLUME</u>				
fl oz	fluid ounces	29.57	milliliters	mL
gal	gallons	3.785	liters	L
ft ³	cubic feet	0.028	meters cubed	m ³
yd ³	cubic yards	0.765	meters cubed	m ³
NOTE: Volumes greater than 1000 L shall be shown in m ³ .				
<u>MASS</u>				
oz	ounces	28.35	grams	g
lb	pounds	0.454	kilograms	kg
T	short tons (2000 lb)	0.907	megagrams	Mg
<u>TEMPERATURE (exact)</u>				
°F	Fahrenheit temperature	$5(F-32)/9$	Celsius temperature	°C

APPROXIMATE CONVERSIONS FROM SI UNITS

Symbol	When You Know	Multiply By	To Find	Symbol
<u>LENGTH</u>				
mm	millimeters	0.039	inches	in
m	meters	3.28	feet	ft
m	meters	1.09	yards	yd
km	kilometers	0.621	miles	mi
<u>AREA</u>				
mm ²	millimeters squared	0.0016	square inches	in ²
m ²	meters squared	10.764	square feet	ft ²
ha	hectares	2.47	acres	ac
km ²	kilometers squared	0.386	square miles	mi ²
<u>VOLUME</u>				
mL	milliliters	0.034	fluid ounces	fl oz
L	liters	0.264	gallons	gal
m ³	meters cubed	35.315	cubic feet	ft ³
m ³	meters cubed	1.308	cubic yards	yd ³
<u>MASS</u>				
g	grams	0.035	ounces	oz
kg	kilograms	2.205	pounds	lb
Mg	megagrams	1.102	short tons (2000 lb)	T
<u>TEMPERATURE (exact)</u>				
°C	Celsius temperature	$1.8 + 32$	Fahrenheit	°F



* SI is the symbol for the International System of Measurement

ACKNOWLEDGMENTS

The authors would like to thank the members of the ODOT Research Group for their assistance in the preparation of this report.

DISCLAIMER

This document is disseminated under the sponsorship of the Oregon Department of Transportation and the United States Department of Transportation in the interest of information exchange. The State of Oregon and the United States Government assume no liability of its contents or use thereof.

The contents of this report reflect the views of the authors, who are responsible for the facts and accuracy of the data presented herein. The contents do not necessarily reflect the official policies of the Oregon Department of Transportation or the United States Department of Transportation.

The State of Oregon and the United States Government do not endorse products of manufacturers. Trademarks or manufacturers' names appear herein only because they are considered essential to the object of this document.

This report does not constitute a standard, specification, or regulation.

FINITE ELEMENT MODELING OF RESIDUAL STRESSES IN ELECTROSLAG BUTT WELDS

TABLE OF CONTENTS

1.0 PROJECT OVERVIEW.....	1
1.1 BACKGROUND.....	1
1.2 MEASUREMENT OF RESIDUAL STRESS	5
2.0 FUSION BOUNDARY ASSESSMENT	7
2.1 INTRODUCTION.....	7
2.2 CORE REMOVAL	8
2.3 ASSESSMENT OF FUSION ZONE CHARACTERISTICS	12
2.4 CONCLUSIONS.....	24
3.0 NUMERICAL ANALYSIS OF RESIDUAL STRESS INDUCED BY THE ELECTROSLAG WELDING PROCESS	25
3.1 BACKGROUND.....	25
3.2 PROGRAMMATIC COMPUTATIONAL MODELING OVERVIEW.....	29
3.3 MOVING COORDINATE SYSTEM IN WELD MODELING	30
3.4 COMPARISON OF FIXED AND MOVING COORDINATE SYSTEMS IN 3D THERMAL MODELS	32
3.5 RESIDUAL STRESS RESULTS FOR 3D MODELS WITH MOVING COORDINATE SYSTEMS.....	50
3.6 MODELING RESULTS	55
3.7 CONCLUSIONS.....	67
4.0 EXPERIMENTAL RESIDUAL STRESS ASSESSMENT	69
4.1 INTRODUCTION.....	69
4.2 RESIDUAL STRESS DETERMINATION FROM CORING.....	69
4.3 CORE REMOVAL AND SUBSEQUENT SECTIONING	70
4.3.1 Relief Strains from Coring	79
4.3.2 Residual Stresses from Coring	80
4.3.3 Residual Stresses from Coring and Sectioning	84
4.4 COMPARISON OF EXPERIMENTAL AND PREDICTED RESIDUAL STRESS.....	89
4.5 RESIDUAL STRESS DETERMINATION FROM HOLE DRILLING.....	91
4.5.1 Introduction	91
4.5.2 Experimental Results	93
4.5.3 Discussion	95
4.5.4 Conclusions	96
5.0 FUTURE WORK	97
5.1 COMPUTER MODELING STUDIES.....	97
5.2 EXPERIMENTAL RESIDUAL STRESS STUDIES	97

5.3 FRACTURE TOUGHNESS STUDIES	98
6.0 REFERENCES.....	101

APPENDICES

APPENDIX A: CORE-RELATED RELIEF STRAIN RESULTS
APPENDIX B: GRAPHS OF CORE-RELATED RELIEF STRAIN RESULTS
APPENDIX C: BRIDGE-RELATED RESIDUAL STRESSES

LIST OF TABLES

Table 2.1: Core mechanical property testing type identification number and description	11
Table 2.2: Difference between widest fusion zone and narrowest fusion zone 2PT and position of fusion line on top of HAZ specimens CD_{top}	23
Table 3.1: Parameters for three dimension numerical analysis of ESW process.....	50
Table 4.1: Core identification number and description.....	71
Table 4.2: Description of strain gage type used for coring and slicing strain change measurements.....	77
Table 4.3: Bridge coring strain gage and stress relief information.....	78
Table 4.4: Comparison of 3D model surface predictions and experimental coring and sectioning ESW residual stress results.....	89

LIST OF FIGURES

Figure 1.1: Schematic of consumable guide electroslag welding process.	1
Figure 1.2: Schematic representation of instrumented electroslag weld plate with sump and runoff.	2
Figure 2.1: Schematic illustration of the West Linn bridge showing relationship of the main channel crossing structure to support piers and approach structures.	8
Figure 2.2: Schematic illustration of the main channel crossing support structure illustrating the independence of the north-bound and south-bound lanes, and the placement of the box girders.....	9
Figure 2.3: Cross-sectional view of the box girders illustrating their labeling sequence.....	9
Figure 2.4: Schematic illustration of the box girder sections bolted together to make up the main channel crossing structure.....	10
Figure 2.5: Schematic illustration of the box girder section 1 and the electroslag welds needed in the fabrication of the girder section.	10
Figure 2.6: Schematic illustration of the electroslag weld core position taken from the bottom flange of box girder section D.	12
Figure 2.7: Typical etched electroslag weld microstructure.	13
Figure 2.8: Schematic illustration of the fusion line shape for WCL cores.....	14
Figure 2.9: Schematic illustration of the fusion line shape for HAZ cores.....	15
Figure 2.10: Relationship of fusion zone width with thickness for WCL cores	16
Figure 2.11: Solidification band shape for WCL cores	17
Figure 2.12: Relationship of fusion line position with thickness for HAZ cores.....	18
Figure 2.13: PT and CD positions for HAZ cores.....	21
Figure 2.14: Relationship between weld number and 2pt, CD_{top} and D_{max} (C7B1, B7B1, B7B2, B3B2 and D3B2 for weld number 1 to 5 sequentially)	22
Figure 2.15: Weld pool shape during electroslag welding	23
Figure 3.1: Schematic representation of plate electrode.....	28
Figure 3.2: Schematic representation of 3-D model.....	28

Figure 3.3: Schematic illustration of the Eulerian coordinate system trajectory motion in the case of a welding process.....	30
Figure 3.4: Mesh for ANSYS fixed and moving coordinate system and SYSWELD moving 2D thermal calculation models	33
Figure 3.5: Illustration of the 3D model geometry for the fixed and moving coordinate Systems	36
Figure 3.6: Temperature profiles for ANSYS fixed coordinate system thermal model calculations as a function of time after weld initiation	41
Figure 3.7: Temperature profile for ANSYS moving coordinate system thermal model calculation.....	46
Figure 3.8: Comparison of thermal history predictions between ANSYS 3D moving and fixed coordinate system models	47
Figure 3.9: Comparison of thermal history predictions between ANSYS and SYSWELD 3D moving coordinate system models	49
Figure 3.10: Temperature dependent thermal conductivity.....	52
Figure 3.11: Temperature dependent enthalpy.....	52
Figure 3.12: Temperature dependent mechanical properties.....	53
Figure 3.13: Temperature dependent Poisson's ratio	55
Figure 3.14: Temperature profiles for SYSWELD 3D moving coordinate system thermal model calculation.....	56
Figure 3.15: Von Mises stress profile for SYSWELD 3D moving coordinate system thermal mechanical model calculation	58
Figure 3.16: Mid-plane and surface residual stress perpendicular to WCL for SYSWELD 3D model	59
Figure 3.17: ANSYS 2D fixed coordinate system model residual stress results	60
Figure 3.18: ANSYS 2D fixed coordinate system model set-up	61
Figure 3.19: SYSWELD 3D model predicted residual stress parallel to weld.....	62
Figure 3.20: SYSWELD 3D model predicted through-thickness residual stress at WCL for 8 cm thick weld.....	63
Figure 3.21: SYSWELD 3D model predicted welding speed effect on surface residual stress perpendicular to welding direction.....	64
Figure 3.22: SYSWELD 3D model predicted welding speed effect on maximum residual stress perpendicular to welding direction in the HAZ/fusion zone	65
Figure 3.23: SYSWELD 3D model predicted welding speed effect on heat input.....	65
Figure 3.24: SYSWELD 3D model predicted plate thickness effect on surface residual stress perpendicular to welding direction.....	66
Figure 3.25: SYSWELD 3D model predicted plate thickness effect on maximum residual stress perpendicular to welding direction in the HAZ/fusion zone	67
Figure 4.1: Strain gage positions, cutting sequence, and slice thickness for West Linn Bridge cores. Gage labels A – F refer to the gage type given in Table 4.1.....	72
Figure 4.2: Calculated residual stress for the base metal cores. TN = 2.5 in. thick plate; TK = 3.5 in. thick plate; PAR = parallel; PER = perpendicular; 90 = 90° two-gage rosette.	81
Figure 4.3: Calculated residual stress for the weld centerline cores. PAR = parallel; PER = perpendicular; 90 = 90° two-gage rosette.	82
Figure 4.4: Calculated residual stress for the weld centerline cores minus the stress due to dead load (total stress – [-10 ksi] perpendicular to the welding direction). PAR = parallel; PER = perpendicular; 90 = 90° two-gage rosette.	82
Figure 4.5: Calculated residual stress for the heat affected zone cores. PAR = parallel; PER = perpendicular; 90 = 90° two-gage rosette.	83
Figure 4.6: Calculated residual stress for the heat affected zone cores minus the stress due to dead load (total residual stress – [-10ksi] perpendicular to the welding direction). PAR = parallel; PER = perpendicular; 90 = 90° two-gage rosette.	84
Figure 4.7: Calculated residual stress for the base metal cores. THIN = 2.5 in. thick plate; THICK = 3.5 in. thick plate.....	85
Figure 4.8: Calculated residual stress for the weld centerline cores. The two sets of values for each core are due to the two strain gage rosettes on each core. PAR = parallel; PER = perpendicular.	86
Figure 4.9: Calculated residual stress for the weld centerline cores segregated by strain gage type. PAR = parallel; PER = perpendicular; 90 = 90° two-gage rosette; 45 = 45° three gage rosette.....	87

Figure 4.10: Calculated residual stress for the weld centerline cores minus the stress due to dead load (total residual stress – [-10 ksi]). The two sets of values for each core are due to the two strain gage rosettes on each core. PAR = parallel; PER = perpendicular. 87

Figure 4.11: Calculated residual stress for the seven heat affected zone cores. The two sets of values for each core (1, 1; 2, 2; etc.) are due to the two strain gage rosettes on each core. PAR = parallel; PER = perpendicular..... 88

Figure 4.12: Calculated residual stress for the heat affected zone cores segregated by strain gage type. PAR = parallel; PER = perpendicular; 90 = 90° two-gage strain rosette; 45 = 45° three-gage strain rosette. 88

Figure 4.13: Calculated residual stress for the heat affected zone cores minus the stress due to dead load (total residual stress – [-10 ksi]). PAR = parallel; PER = perpendicular. 89

Figure 4.14: Predicted surface residual stress changes perpendicular to the welding direction as a function of distance from the weld centerline. 90

Figure 4.15: Predicted surface residual stress changes parallel to the welding direction as a function of distance from the weld centerline. 90

Figure 4.16: Envelope of expected strain changes for a uniform through-thickness stress state as determined by the blind-hole-drilling method as a function of normalized hole depth..... 93

Figure 4.17: Measured strain for a hole drilled one inch from the weld centerline compared with the expected uniform through-thickness stress envelope as a function of normalized hole depth..... 94

Figure 4.18: Calculated change in residual stress for a hole drilled one inch from the weld centerline as a function of normalized hole depth. 94

Figure 4.19: Estimated surface residual stress as a function of stress direction, hole drilling set, and distance from the weld centerline. SIGMA MAX-1 = nominal stress parallel to the welding direction for set one readings; SIGMA MAX-2 = nominal stress parallel to the welding direction for set two readings; SIGMA MIN-2 = nominal stress perpendicular to the welding direction for set two readings. 95

1.0 PROJECT OVERVIEW

1.1 BACKGROUND

Oregon has two steel bridges that were fabricated using electroslag welding (ESW). One is the West Linn Bridge on Interstate-205. The other is the approach structure to the Fremont Bridge on I-405.

Electroslag welding was developed by Paton and his coworkers in the Paton Electric Welding Institute, USSR, in the early 1950's.^[1] Research organizations in various countries, such as the Bratislava Institute of Welding in Czechoslovakia, Arcos Corporation in Belgium,^[2] the British Welding Institute,^[3] the U.S. Steel Corporation,^[4] and the Oregon Graduate Institute (OGI)^[5-26] have performed research on the electroslag butt welding processes.

There are two types of electroslag (ES) welds: consumable and non-consumable ESW.^[27] The type of ESW of interest here is the consumable guide electrode welding system, as shown in Figure 1.1. In this technique the consumable wire electrode guide (or in some cases, a plate electrode guide) is consumed as the process progresses. The wire electrode material feeds continuously down the guide and melted into a molten slag pool. The pool is resistively heated by the current that passes from the electrode wire/guide, through the molten slag and the molten metal pool below the slag pool, to the base plates. Two water-cooled copper shoes provide a mold through which a major portion of the thermal energy is removed from the system. The shoes assure that the molten metal and slag remain contained between the plate edges being welded.

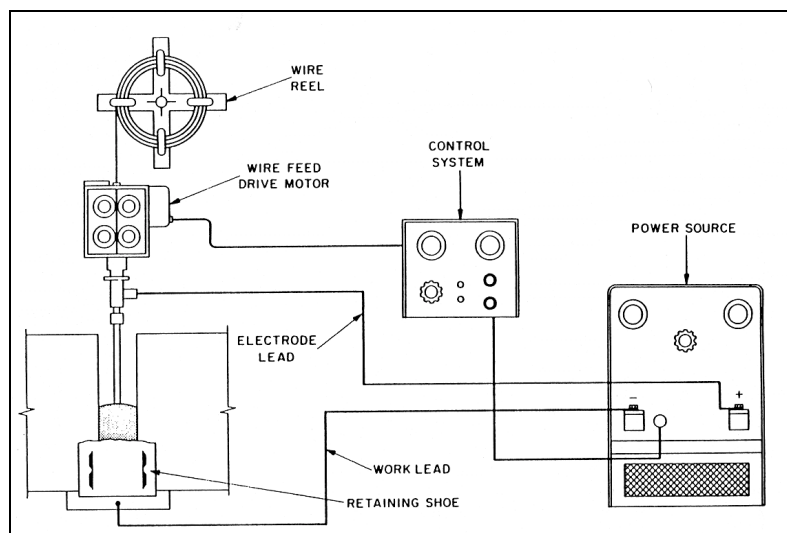


Figure 1.1: Schematic of consumable guide electroslag welding process.

The process is initiated by an electric arc between the electrode and the bottom of the weld. Powder flux is then added and melted by the heat of the arc. Once a 3.8 - 5.1 cm. (1.5 to 2 inches) layer of molten slag is established, the arc stops and a 500 to 700 amp welding current passes from the electrode through the slag pool by electrical conduction. At the start, the guide tube is positioned with its tip at about 3.8 cm. (1.5 inches) above the weld pool. During the processes, the guide tube is consumed in the weld pool. This method involves no moving parts except the welding electrode.

Electroslag welds are performed in the vertical or the near vertical welding position. The welding technique utilizes a starting sump and a runoff out block to minimize defects associated with the initiation and the termination of the process, as shown in Figure 1.2. This practice also results in the weld being in quasi-steady-state once the weld reaches the bottom of the plates to be welded and allows the weld to remain in quasi-equilibrium clear to the top of the plates to be welded.

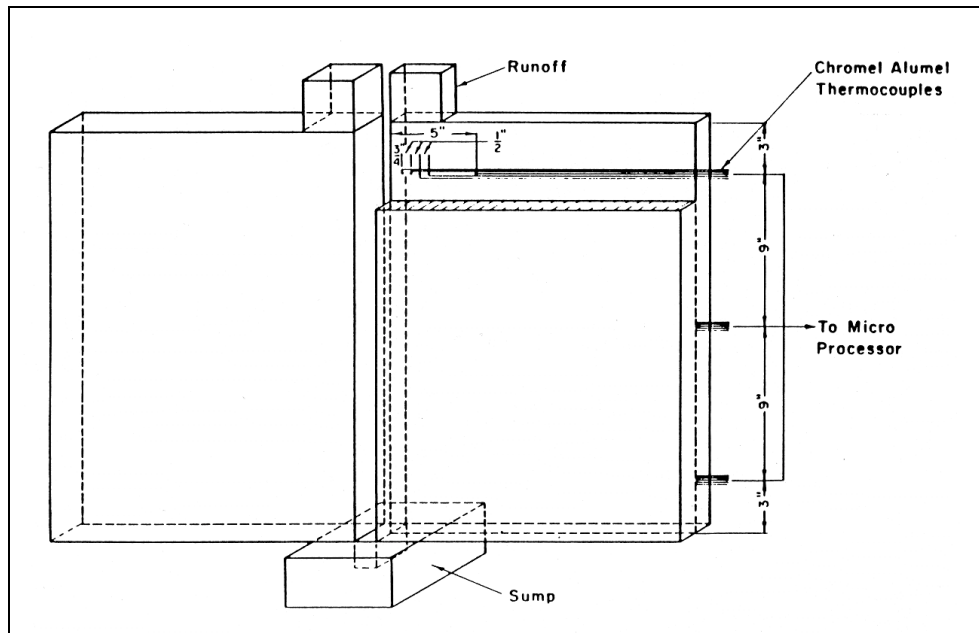


Figure 1.2: Schematic representation of instrumented electroslag weld plate with sump and runoff.

All welds exhibit a start-up region that is far from the equilibrium state of the weld, which is established a considerable time after and/or distance from the start. ESW uses a starting sump to minimize this start-up effect. The sump allows the weld/slag pool to reach its equilibrium size and shape prior to reaching the bottom of the plates to be welded. The sump region also allows time/distance for the thermal field associated with the molten region to approach equilibrium. However, thermal equilibrium is not achieved until the weld travels from the sump region to the region contained by the ends of the pieces being joined and the copper plates.

Nevertheless, the near-molten-zone isotherms are well established in a relatively short time and remain nominally constant up to the molten region's entry into the run-off sump at the end of the weld. Thus the ESW process is considered to be a quasi-equilibrium/steady state process for the majority of its length.

The ESW process is a good method for the welding of thick plates, which includes construction of ships, storage tanks, pressure vessels, bridges, buildings and other heavy structures. Sections that are several inches thick can be welded in a single pass by selecting a suitable number of electrodes or by using electrode oscillation. The sections being welded do not need any special surface preparation. Flame cutting is suitable because ESW is more forgiving of surface finish and side wall perturbations than are other welding techniques. Preheating is generally not needed. Distortion is minimal when compared with other welding processes. If properly controlled, the slag-metal reaction involved in the ESW processes results in sound, "defect-free" welds.

Low fracture toughness and difficulties in detecting weld defects are the main reasons for the ESW process not being used more extensively. The large heat input associated with the process results in a coarse-grained cast structure with a wide coarse grained region in the heat affected zone (HAZ). The cast structure has anisotropic mechanical properties. Grain orientation and segregation can lead to hot cracking near the weld center-line. This coarse-grained structure is more susceptible to brittle fracture than the parent material. According to fracture mechanics, once a critical-size flaw or crack is formed, this type of structure is susceptible to catastrophic failure. When this critical size is reached, the crack propagates in a brittle fashion.

Evaluation of structural safety is primarily based on determining the size of existing defects and correctly identifying the critical size. Fracture toughness calculations are used to evaluate a weld-specific critical crack size. The larger the critical crack size makes it easier to reliably detect defects in the weld. The major factor in determining critical crack size is the residual stresses created by the welding process. When calculating critical crack size this residual stress field needs to be added to the live and dead loads.

It is generally assumed that the weld-induced stress field is tensile and of yield strength magnitude. This assumption greatly reduces the allowable flaw size, especially when compared to the allowable flaw size when design stresses are considered alone. Electroslag welds tend to have poor fracture toughness, especially at the weld center-line and HAZ interface. The calculated critical crack size for ES welds, based on yield stress magnitude residual stress, may be smaller than cracks that can be reliably detected by standard non-destructive testing techniques. Thus, there is a need for determining actual residual stresses associated with ESW.

The total stress state at the tip of a crack is one of the most important factors influencing the mechanisms of fatigue, brittle fracture, and stress corrosion cracking. In all of these failure mechanisms, the residual stress in the weldment makes a major contribution to the stress field at a crack tip.

Conventional inspection of ES weldments under shop fabrication conditions has historically failed to consistently detect and/or correctly size weld discontinuities. For this reason the Federal

Highway Administration (FHWA) banned ESW on all fracture critical members in steel bridges in 1977.

The FHWA has recommended that the Oregon Department of Transportation (ODOT) either research the critical flaw size associated with ES welds on its bridges to demonstrate that the bridges are safe, or bolt splice the ES flange welds located in the tensile portion of the spans. The bolt splice option for the West Linn Bridge alone is estimated to cost \$4 million - \$8 million dollars. Because of this high cost, an effort is currently underway to evaluate the ES welds on the West Linn Bridge. In the future the Fremont approach structure will be evaluated as well, and this study is part of that effort.

The objective of this study was to develop a computational and experimental assessment of the residual stress state of the ES weldments present in the West Linn Bridge. This work entailed the following tasks:

- development of finite element analysis (FEA) predictive models for ES weld-induced residual stress fields.
- experimental determination of bridge-specific ES weldment fusion zone characteristics.
- experimental determination of bridge-related residual stress values.

Residual stresses can be defined as the self-equilibration of internal stresses existing in a free body with no external loads or restraints. Residual stresses are formed when portions of a member undergo non-uniform permanent dimensional change. The permanent dimensional change usually occurs as plastic deformation.

Residual stresses in weldments occur due to uneven heating and cooling and also uneven distribution of non-elastic strains.^[33-35] Residual stresses arise from the difference in shrinkage of differently heated and cooled areas of a welded joint. The weld metal, originally subjected to the highest temperature, upon cooling tends to contract more than all other areas. This is hindered by the other parts of the joint, thus resulting in the formation of residual stress fields in the vicinity of the weld.

Residual stresses can also arise from phase transformations that occur during cooling if the transformations are accompanied by an increase in specific volume of the material being transformed. This expansion is hindered by the cooler surrounding material and thus causes residual stresses.

A reasonable amount of experimental and computational research has been done towards assessing multi-pass weld induced residual stresses, and it is generally assumed that one has tensile yield stress residual stresses in the fusion zone region. Much less is known about the residual stress distribution of ES weldments. ESW is a single pass thick-section welding technique with much higher weld heat inputs than used in multi-pass welds. ESW has a much wider melt zone and much slower cooling rates than standard multi-pass welding techniques.

Thus the ESW residual stress fields would be expected to be lower in magnitude with shallower stress gradients than conventional multi-pass weldments. Therefore there is a potential for larger allowable flaw sizes than can be predicted by simply assuming yield strength level residual stresses in the complete fusion zone and near fusion zone-heat affected zone. In fact, if some region of the weldment is in compression, flaws in compression won't propagate. Even if the stress field is found to be tensile in nature, but less than yield strength magnitude, increased accuracy estimates of critical flaw size can be made which would be expected to greatly increase the expected critical flaw size.

Programmatic residual stress estimates were made experimentally as well as computationally. Experimental measurements were made in the hopes of developing a residual stress model validation database. The experimental techniques used to measure the residual stresses are presented below and discussed in detail in later section of the report.

1.2 MEASUREMENT OF RESIDUAL STRESS

Many techniques have been developed to measure residual stress. They can be classified into two types:

- destructive or semi-destructive measuring methods, and
- non-destructive measuring methods.

Destructive and semi-destructive measuring methods were used in this study. During measurement, residual stress is treated as a macrostress contained within a metallic component or specimen. These stresses can be represented as a statistical average of stresses across a particular finite length in a component.

The most common and representative destructive technique is the "sectioning method" in which strain gage rosettes are attached to a structure at axial and circumferential (or parallel and perpendicular) positions within the boundaries of a selected specimen geometry. After the specimen is removed from the structure, more strain gages may be attached to the specimen prior to a series of slicing operations. The change in strain data from removing and slicing the specimen can potentially be used to assess surface residual stresses as well as the variation of residual stresses through the thickness.^[38] This method is applicable to non-axisymmetric as well as axisymmetric residual stress distributions. A variation of this technique was used in this study.

The hole drilling method was also used in this study. It is referred to as a semi-destructive residual stress measuring method. It was proposed by Mathar in 1934.^[37] The hole drilling method is based upon measurement of the change in surface strain caused by stresses relieved by machining a shallow hole in the test piece. Bonded electrical resistance strain gages (rosettes) are used to measure the strain change. It is the most widely used modern technique for measuring residual stress. The measuring procedure has been standardized in ASTM Standard Test Method E837-85^[38]. The hole size typically ranges from 1.5 to 3.0 mm (1/16 to 1/8 in.) in both diameter and depth. In most practical applications of the method, the drilled hole is blind

with a depth about equal to its diameter and small compared to the thickness of the test object. Most applications have been done on flat plate or cylindrically round parts. ^[39-41]

The sectioning technique was used on cylindrical cores removed from the bridge structure and subsequently cut into smaller slabs, while the hole drilling method was performed in situ on the bridge. The use of the sectioning technique was limited to the middle of the weld fusion zone and a short (arbitrary) distance out from the fusion zone. Thus the most one could expect from the results of this technique were residual stress results at and close to the fusion zone. It was also desired to experimentally determine surface residual stress values as a function of distance from the weld centerline (WCL) in order to validate residual stress computations. This was attempted using the hole drilling technique in situ on the West Linn Bridge.

The following chapters present the work as follows:

2. Assessment of fusion zone characteristics;
3. Computational residual stress modeling results;
4. Assessment of surface stresses by the experimental stress analysis techniques;
5. Conclusions.

2.0 FUSION BOUNDARY ASSESSMENT

2.1 INTRODUCTION

The welded plates of the West Linn Bridge have been in service for over 30 years; the bridge was built in 1968. The ESW process was used to shop-weld plates together to form the top and bottom flanges of the box girders. One generally develops weld models based on a set of operating parameters. The operation parameters that were used during the ESW process for the welded plates on the West Linn Bridge are not known, however. The size and shape of the molten pool are the most important factors in determining the weldment properties and residual stress distribution. Thus if one can determine the molten weld pool shape present during welding of the plates, the residual stress distribution inside the plates can be estimated without detailed information of welding process operation parameters. Experimental work was performed to determine the molten pool shape and size present during the West Linn Bridge-specific ESW process. This information was subsequently used as input for numerical analysis of the residual stress field.

It is well known that the welded region in general can be classified into three zones: fusion zone, heat affected zone (HAZ) and base metal. The easiest to distinguish is the fusion line from weldments using microanalysis. It is very difficult to identify the extent of the HAZ, as its etching characteristics grade into those of the base metal. The HAZ lies between base metal and fusion zone. The width of the HAZ is several millimeters, which is negligible compared to the fusion zone dimension of centimeters. Thus, in this study the fusion line position was measured without assessing the HAZ.

The results of preliminary FEA research reveal that molten pool shape and size are very important to the accuracy of simulating a welding process. During the solidification process, liquid does not solidify continuously. Solidification bands form because of segregation of elements during the discontinuous solidification process. The shapes of the bands reflect the shape of the molten pool when the bands are formed. These bands can subsequently be detected by etching techniques. The shape of the molten metal pool during welding can be inferred from the geometry of solidification bands.

The West Linn Bridge-specific ES weld fusion zone characteristics were assessed at Oregon Graduate Institute of Science and Technology (OGI) by analysis of cores removed from the weld area by ODOT personnel for subsequent material toughness assessment. This core material was macro-etched to reveal the fusion zone structure.

2.2 CORE REMOVAL

Multiple cores were removed from box girders of the West Linn Bridge. Plate girders versus box girders support the approach structures to the Bridge. Two box girders support each traffic deck on the main channel crossing structure, with each traffic direction deck structure being totally independent of the other, as shown in Figure 2.1 and 2.2. The four box girders are sequentially lettered from A to D, starting with A-girder on the external, downstream side of the southbound traffic deck, as shown in Figure 2.3. The 14 support piers for the approach structures and main channel crossing structure are numbered sequentially from 1 to 14, beginning on the east side of the river and ending on the west side of the river. The main channel crossing structure begins at pier 3 and ends at pier 6. Multiple girder sections make up a given main channel crossing box girder. In fact, each box girder is made up of nine shop-fabricated girder sections that were field bolted together to make the main channel crossing girder.

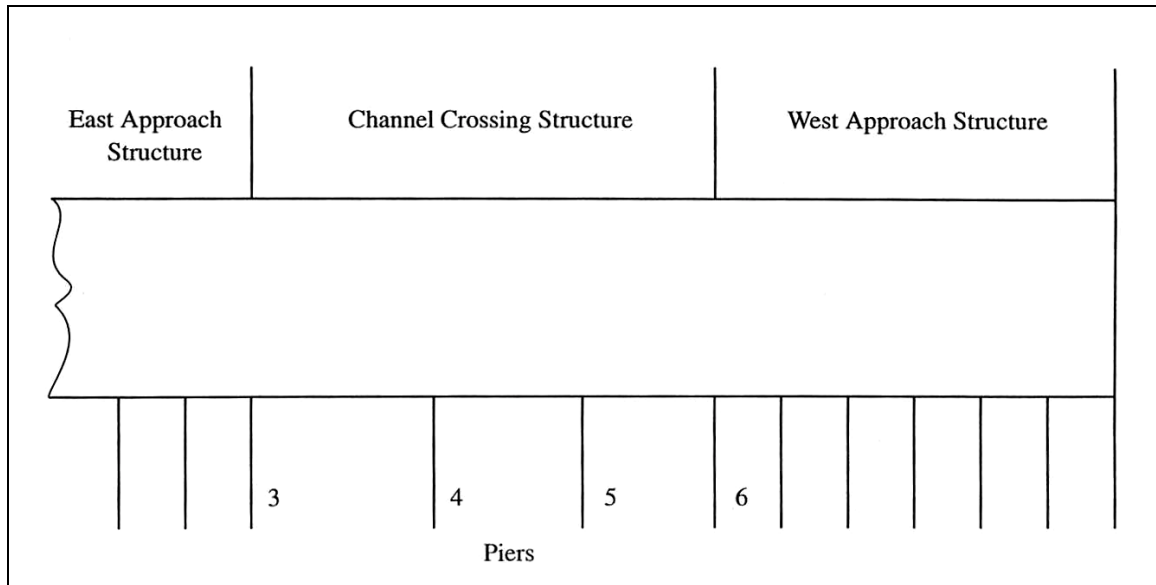


Figure 2.1: Schematic illustration of the West Linn bridge showing relationship of the main channel crossing structure to support piers and approach structures.

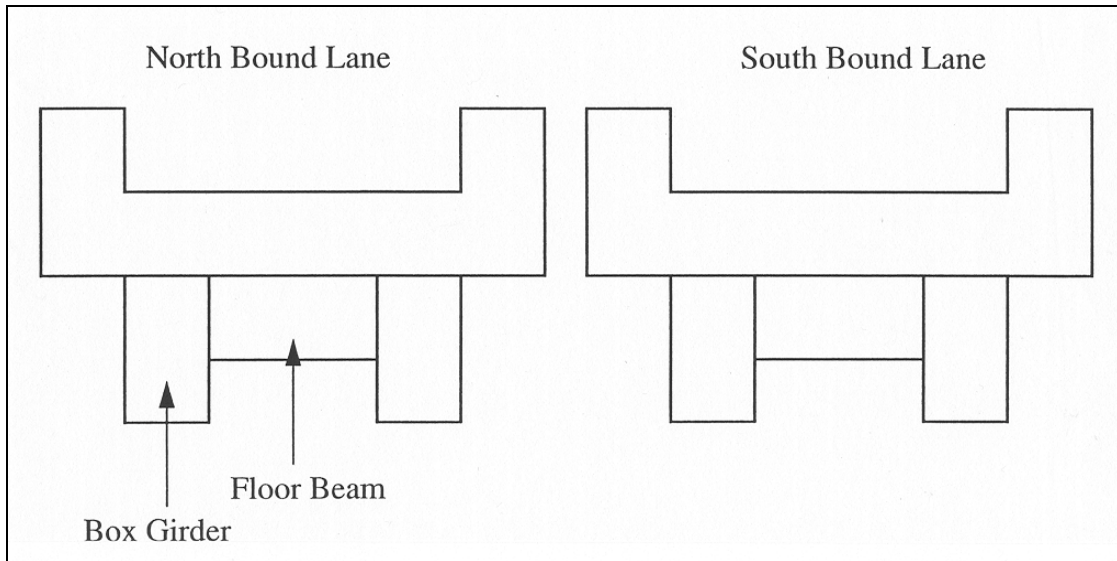


Figure 2.2: Schematic illustration of the main channel crossing support structure illustrating the independence of the north-bound and south-bound lanes, and the placement of the box girders.

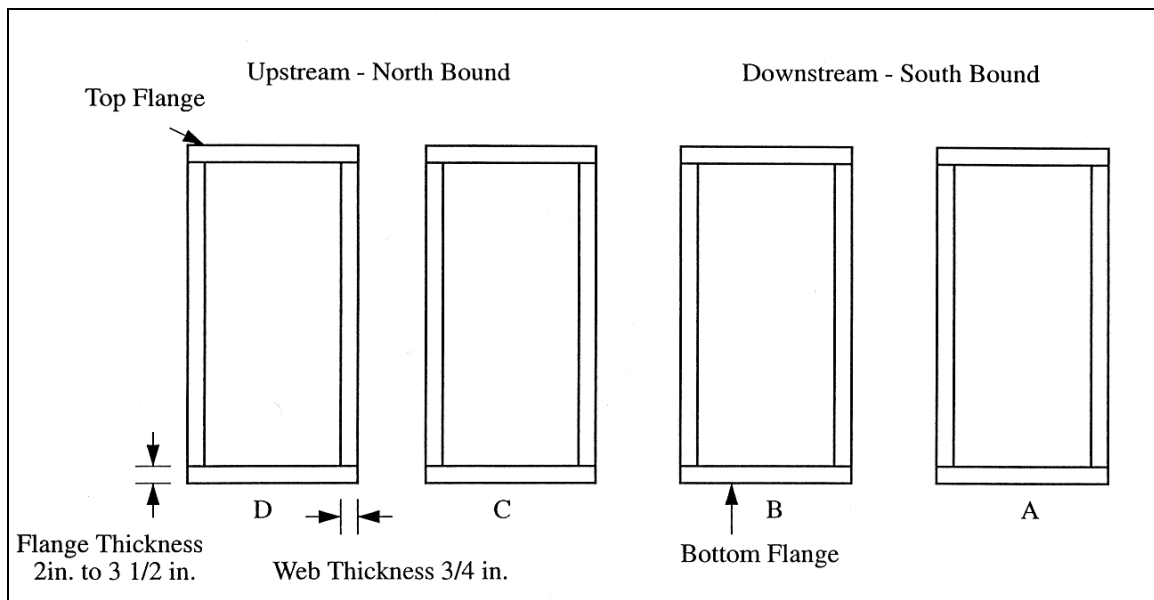


Figure 2.3: Cross-sectional view of the box girders illustrating their labeling sequence.

The individual box girder sections are numbered 1 to 9, starting on the east side of the river and running to the west side of the river, as shown in Figure 2.4. Each individual girder section is further characterized by a letter designation from A to D before the girder section number, to identify the specific box girder with which it is associated. The shop-fabricated electroslog weldments for each girder section are identified by position and number of welds from the east

end of the girder section, as well as the overall girder section number. The position identification designates whether the weldments are at the top of the box girder (T), and thus under the roadway, or at the bottom of the box girder (B), thus facing down to the river, as shown in Figure 2.5. An example of a complete ES weldment identification number would be D3B1; this weldment is the first weldment from the east side in the third box girder section in the external, up-river side box girder under the northbound traffic deck of the main channel crossing support structure.

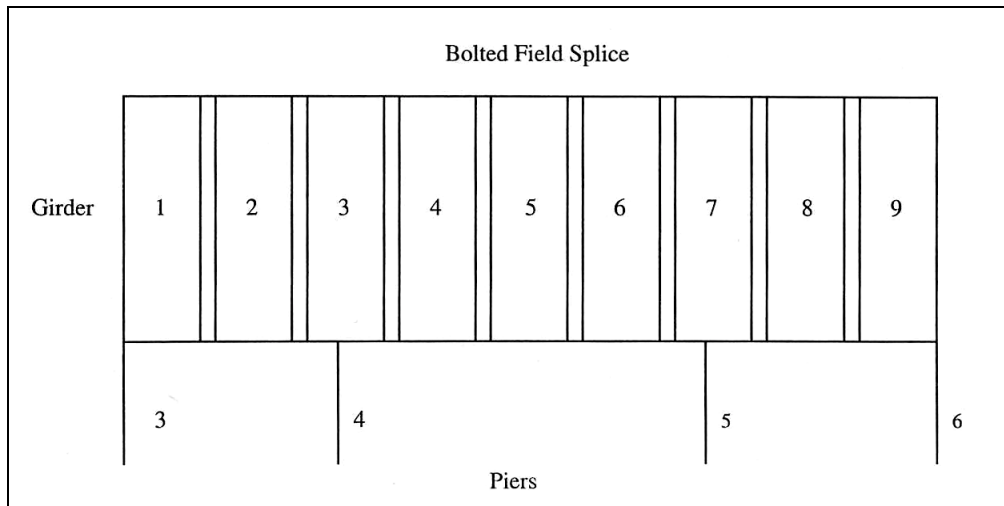


Figure 2.4: Schematic illustration of the box girder sections bolted together to make up the main channel crossing structure.

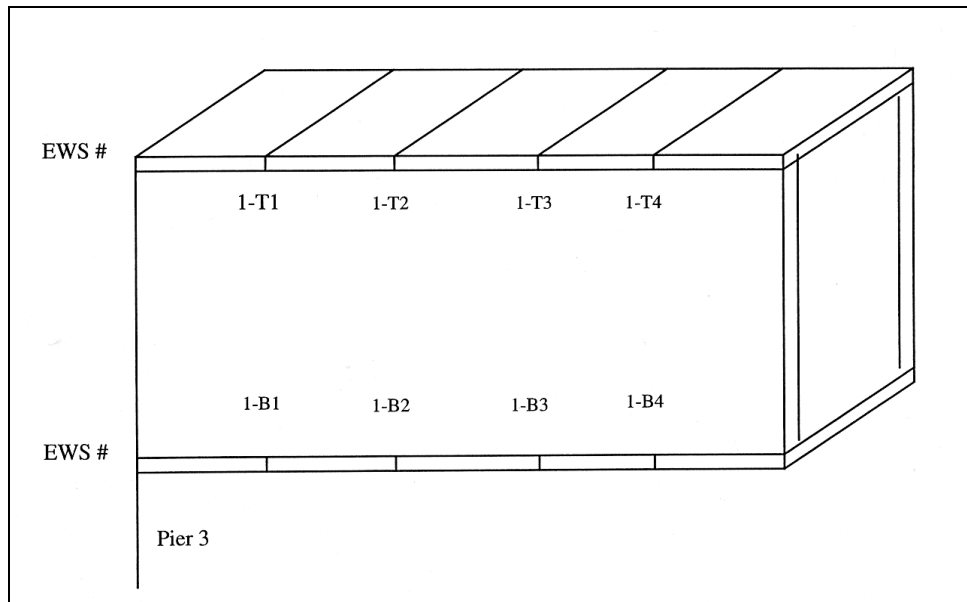


Figure 2.5: Schematic illustration of the box girder section 1 and the electroslag welds needed in the fabrication of the girder section.

The bolted connections attaching one box girder section to another are designated as "field splices" and are numbered 1 through 8, starting at the splice between the eastern-most box girder sections (Girders 1 and 2) and ending at the western-most box girder sections (girders 8 and 9).

The cores were taken from three out of four of the box girders of the channel crossing structure (B, C and D) from ES weldments which were in compression loading on the bottom floor of the box girder. A core drilling machine was placed over the spot to be core-drilled and bolted in place using 5/8 inch (1.6 cm) bolts screwed 1 to 1-1/2 inches (2.5 - 3.8 cm) into the box girder plate in threaded holes specially pre-drilled for this operation. The girder was 3.5 inches (8.9 cm) thick, and the core diameter was 3.5 inches (8.9 cm). It took about 1 to 1- 1/2 minutes to drill each core.

The core was drilled from inside the box girder toward the outside, or down toward the Willamette River. A hydraulic bucket was positioned below the expected point of exit, and the cores were "caught" as they fell away from the bottom of the girder bottom plate. Special compression load-bearing devices were installed into the core holes after each core was drilled. The two-piece units were pulled together by turning a connection bolt until they snugly contacted the core hole edges. The drilling machine bolt holes were assumed to have essentially no effect on subsequent load distribution and were simply filled with grease to deter liquid penetration.

Fourteen cores were removed from the bridge. Two were base metal cores, five were weld centerline specimens, and seven were HAZ specimens, which had the core center point 1/2 inch (1.8 cm) out from the fusion line edge. One base metal core was drilled 8 feet (2.4 m) from the D3B1 core. The other base metal core was drilled on B girder 72 inches (1.8 m) from the end. The base metal cores were assumed not to be affected by the ESW process. The base metal cores were drilled to allow assessment of the stress distribution inside the plate without the effect of thermal stress from the welding process. The actual core designations are given in Table 2.1. The core drilling position is determined by core identification number. For example, the position of cores taken from the bottom flange of box girder, section D, on the welded plate is shown in Figure 2.6.

Table 2.1: Core mechanical property testing type identification number and description

Number	Specimen ID	Mechanical Test Type	Core Type
1	B1+4	Fracture Toughness	Base Metal
2	B3B1	Fracture Toughness	Weld Center Line
3	B3B2	Fracture Toughness	Weld HAZ
4	B7B1	Fracture Toughness	Weld HAZ
5	B7B2	Fracture Toughness	Weld HAZ
6	C3B1	Fracture Toughness	Weld HAZ
7	C3B2	Fracture Toughness	Weld Center Line
8	C7B1	Fracture Toughness	Weld HAZ
9	C7B2	Fracture Toughness	Weld Center Line
10	D3B1+8	Charpy Impact	Base Metal
11	D3B1	Fracture Toughness	Weld Center Line
12	D3B2	Charpy Impact	Weld HAZ
13	D7B1	Fracture Toughness	Weld HAZ
14	D7B2	Charpy Impact	Weld Center Line

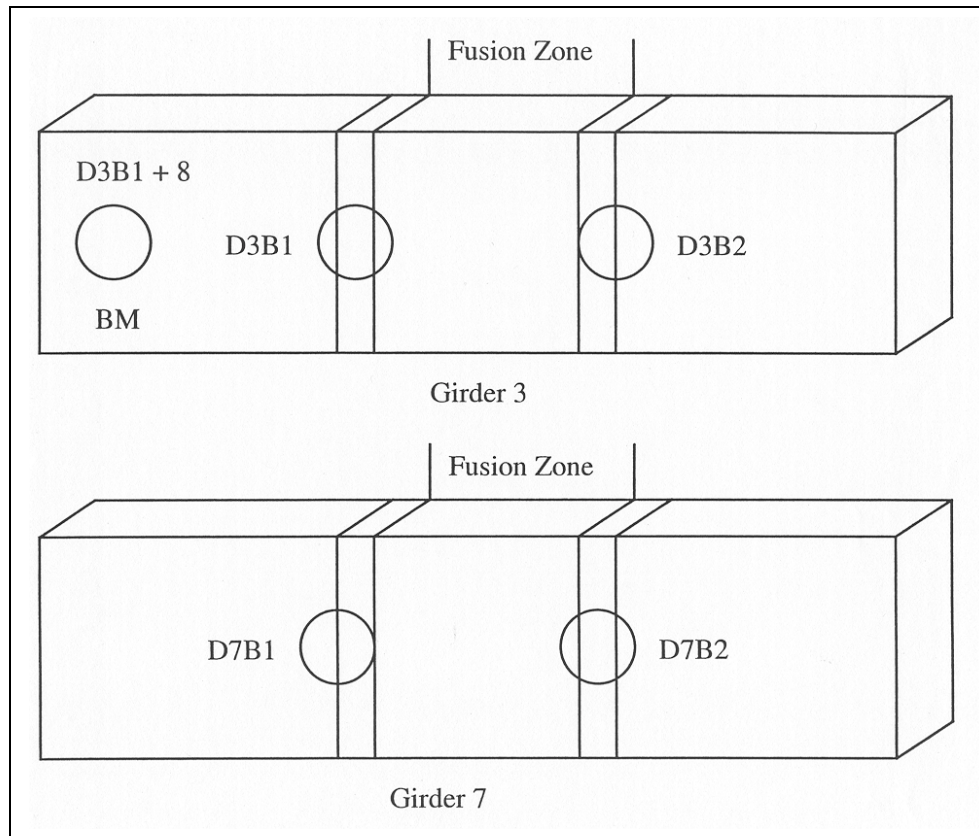


Figure 2.6: Schematic illustration of the electroslag weld core position taken from the bottom flange of box girder section D.

2.3 ASSESSMENT OF FUSION ZONE CHARACTERISTICS

The core specimens were cut into several slices using a band saw. The thickness of each slice was decided by the type of mechanical test to be performed on specimens machined from the slice. For example, if the slice was to be machined into a fracture toughness test specimen after being cut from core, a one-inch plus clean-up thickness was used during the slice cutting. If the slice was to be used for Charpy-V-Notch (CVN) test specimens, a 0.394 inch (10 mm) CVN specimen thickness plus clean-up was the slice thickness. The core mechanical property testing type identification number and their descriptions are given in Table 2.1. All of the cores were cut at the same slow cutting speed with water cooling during the cutting process.

Selected core slices were polished and etched to reveal the ES weld solidification structure. A 5% nitric acid solution was used to etch each slice. After each etching, the fusion line and solidification bands could be seen. The microstructure after etching a WCL specimen is shown in Figure 2.7a while a HAZ is shown in Figure 2.7b. Typical weld solidification bands are shown in Figure 2.7c along with their relationship to current spikes during ESW welding.

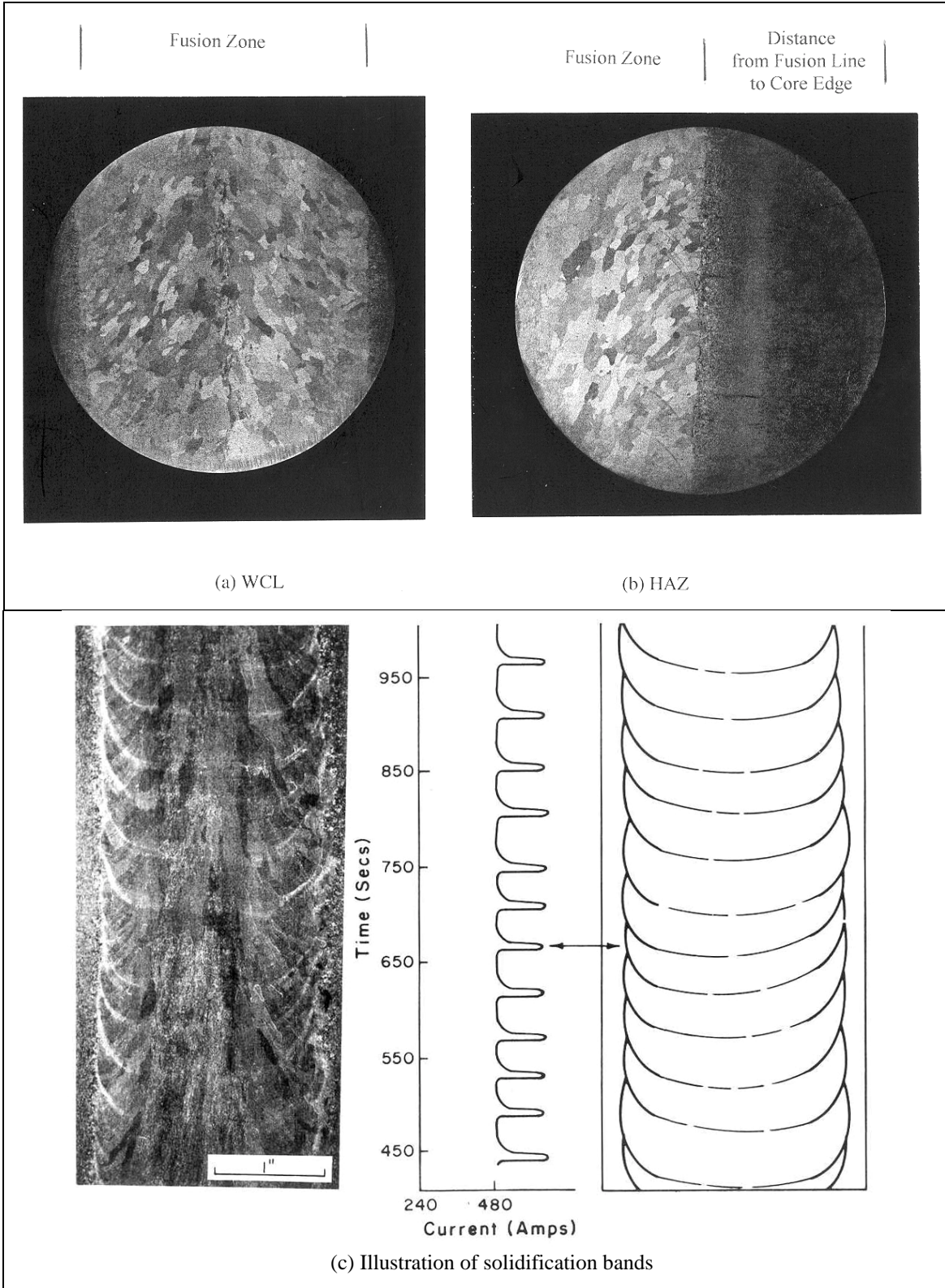


Figure 2.7: Typical etched electroslag weld microstructure.

The position of the fusion line from the WCL and the width of the solidification bands were used to characterize the through-thickness molten pool. Weld centerline specimens are better candidates for this work because the complete fusion zone is present in analysis of slices. Assessment of weld centerline specimens indicated that the fusion zone was symmetrical. Thus, under the assumption of weld symmetry, HAZ cores could be used to measure the fusion line position through-thickness, knowing the HAZ core position relative to the welded plate.

Each core exhibited slightly different operation parameters during the welding process. For example, some cores had an obvious restart operation during the welding process that led to a double fusion line. Fusion line shape variation allows assessment of the consistency between welds. Even though the operator is fabricating each weld according to the same welding code, operating variations may cause different operation results in practice.

Two kinds of WCL specimen fusion line shapes were found, as shown in Figure 2.8. B3B1 and D3B1 cores were drilled slightly off center and have incomplete fusion zones, as shown in Figure 2.8a. C7B2 and C3B2 cores contain the complete fusion zone as shown in Figure 2.8b. The reason for the fusion line shape difference between Figure 2.8a and Figure 2.8b is the drilling position deviation for cores C7B2 and C3B2 on welded plate. This deviation occurred because the presence of fusion line weld repairs made it impossible to correctly judge where the actual ESW surface fusion line was when the core was drilled.

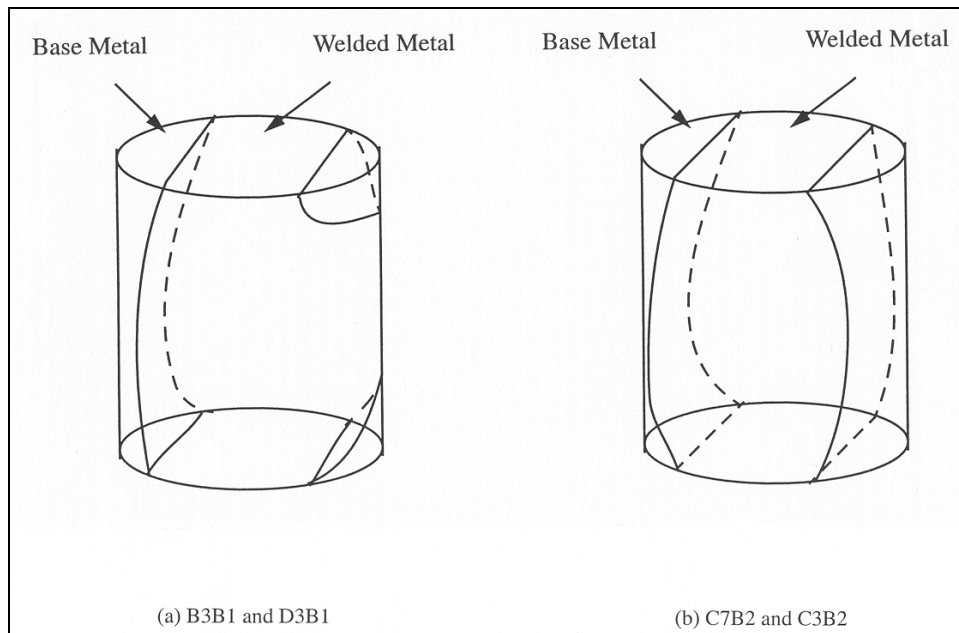


Figure 2.8: Schematic illustration of the fusion line shape for WCL cores.

Three kinds of HAZ specimen fusion line shapes were found, as shown in Figure 2.9. C7B1, B7B1, B7B2, B3B2 and D3B2 core specimens have one distinct fusion line shape over the complete specimen length as shown in Figure 2.9a. The fusion line shape of D7B1 exhibits a

"double" fusion line near the bottom of the specimen with a distinct difference in the bottom surface intercept placement between the two fusion line as shown in Figure 2.9b. The fusion line shape of C3B1 core specimen exhibits a double fusion line with the same bottom surface intercept placement as shown in Figure 2.9c.

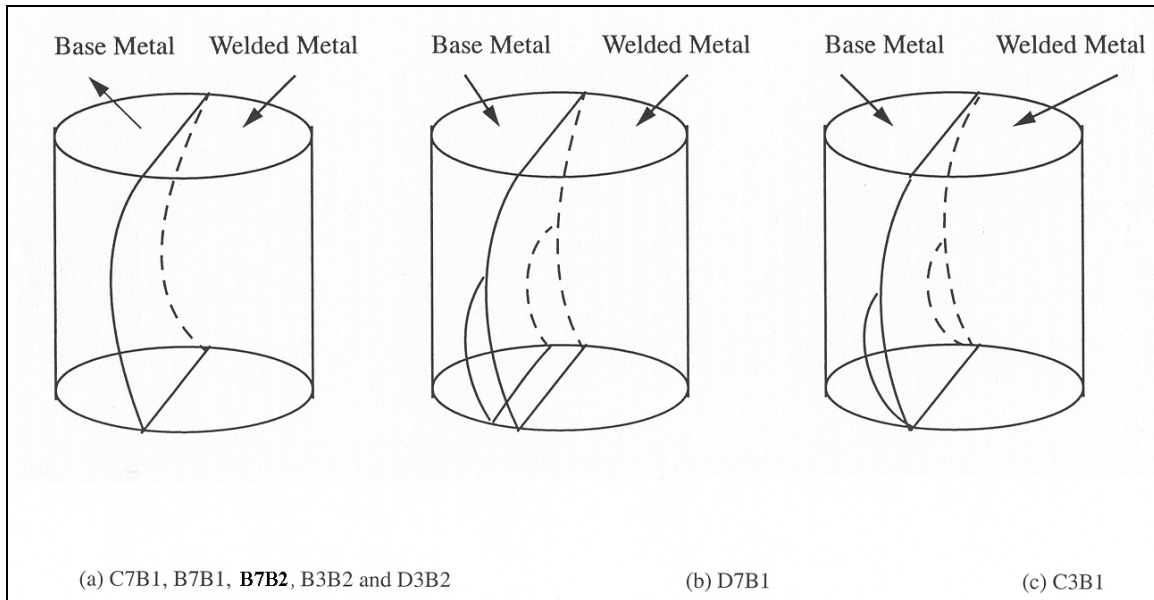
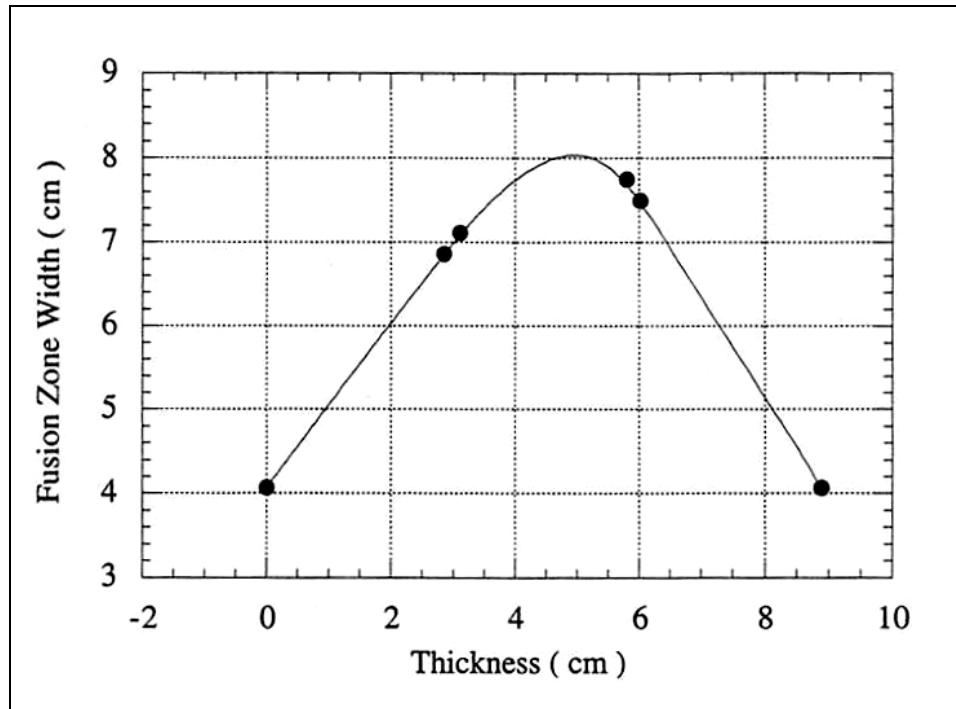
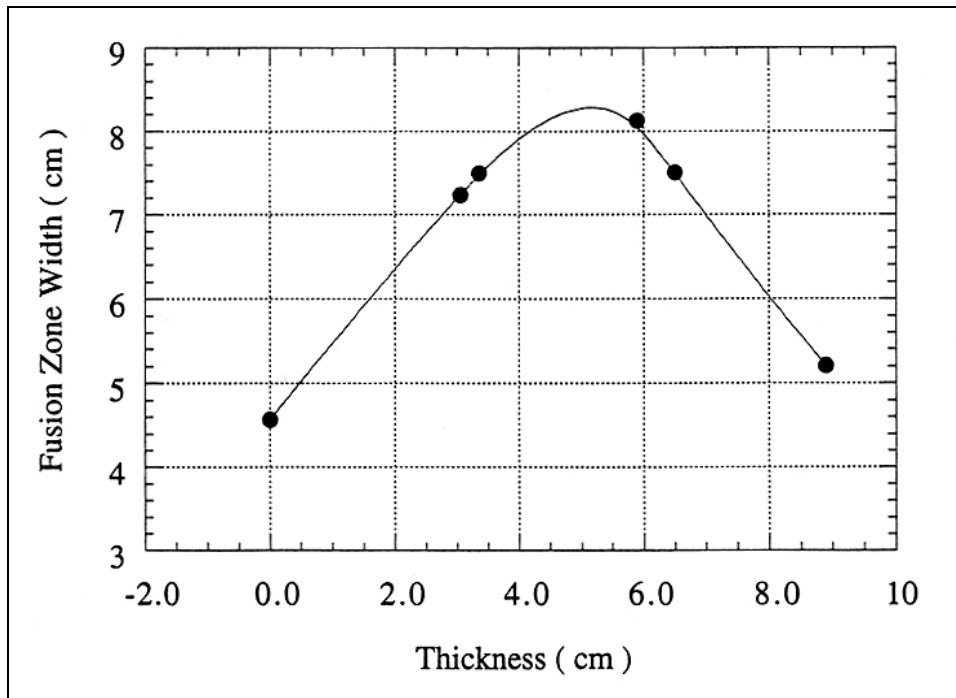


Figure 2.9: Schematic illustration of the fusion line shape for HAZ cores.

Fusion zone width, as determined by metallographic analysis, varies through the plate (core) thickness. The relationship between fusion zone width and etched slice surface distance from the core surface is shown in Figure 2.10a and b for WCL cores B3B1 and D3B1. Solidification band shapes, determined using solidification bands from the etched cross-sections of the cores, for the WCL cores B3B1 and D3B1 are shown in Figure 2.11a and b, respectively.

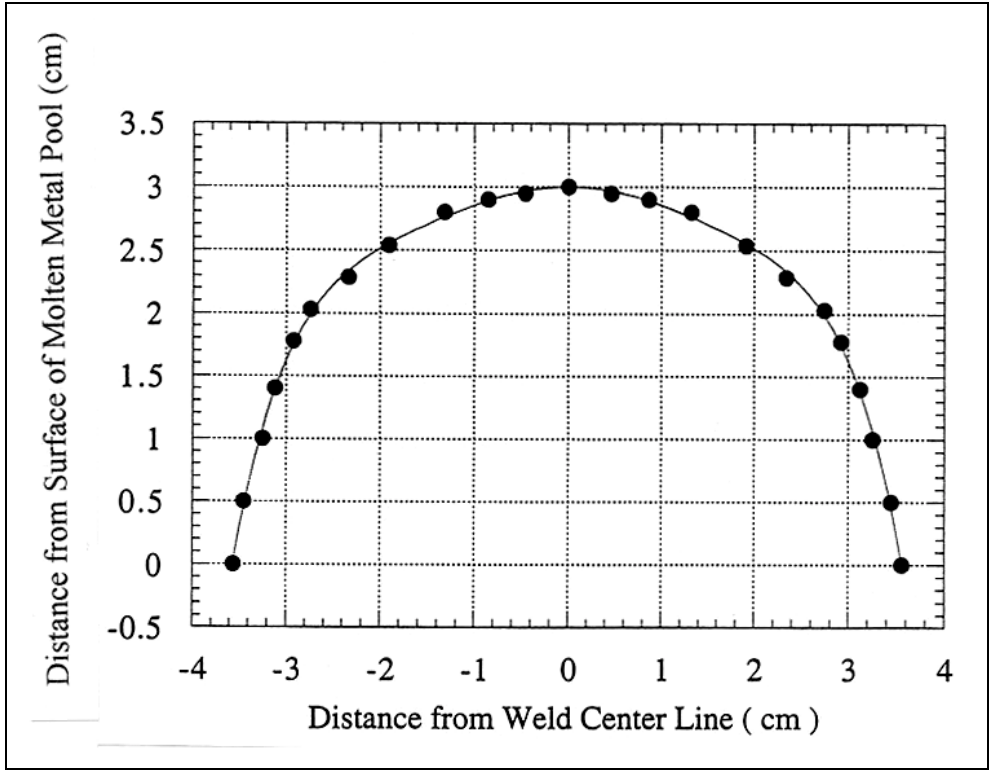


(a)B3B1

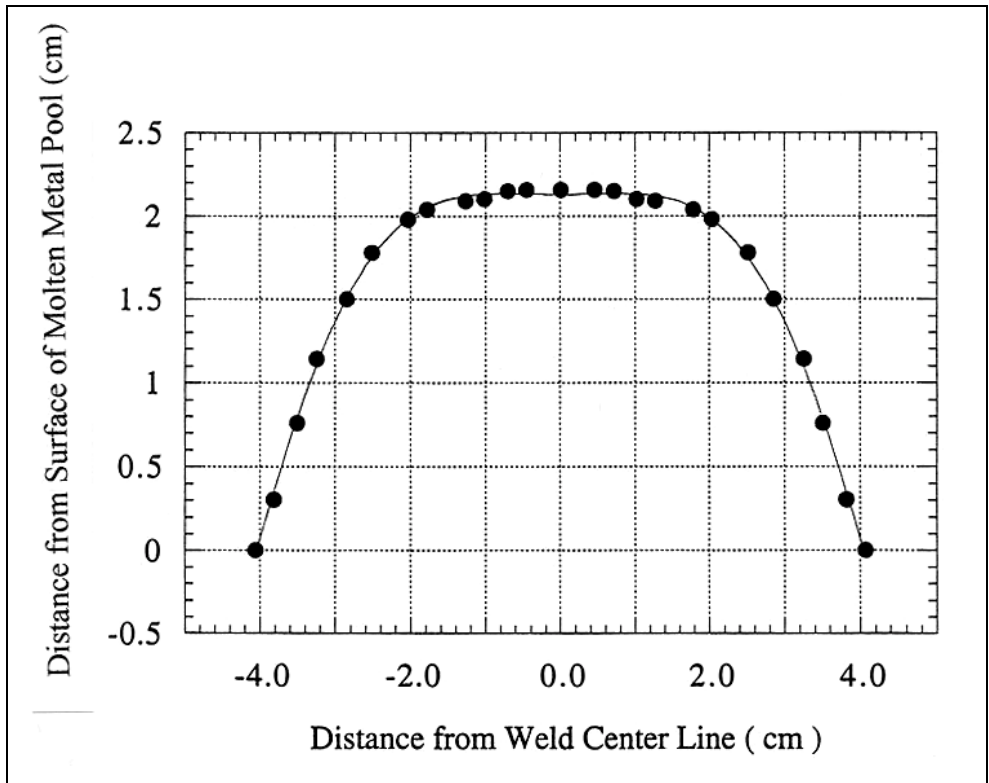


(b)D3B1

Figure 2.10: Relationship of fusion zone width with thickness for WCL cores



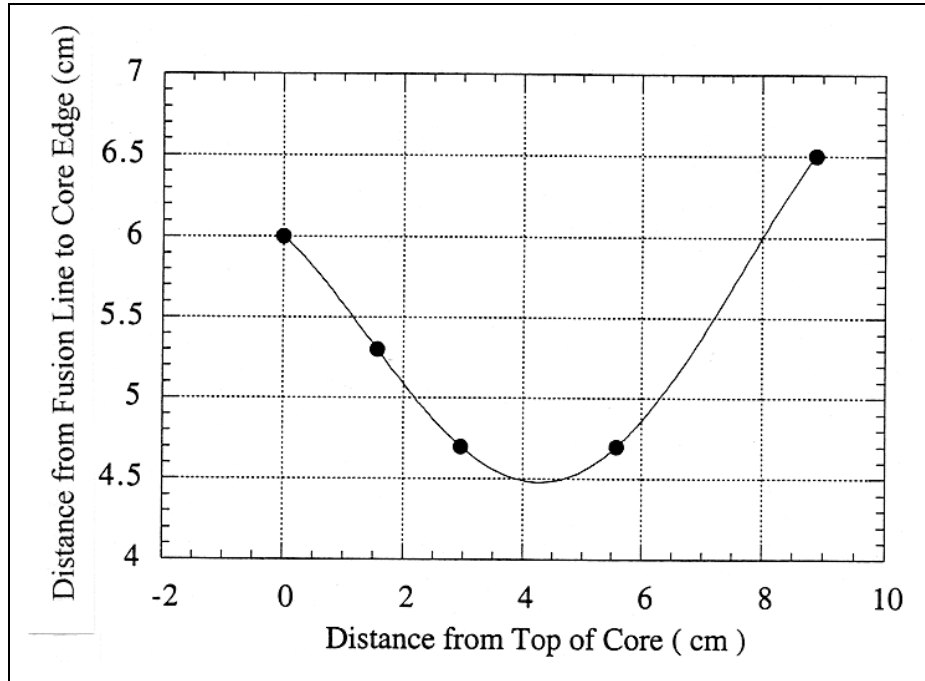
(a)B3B1



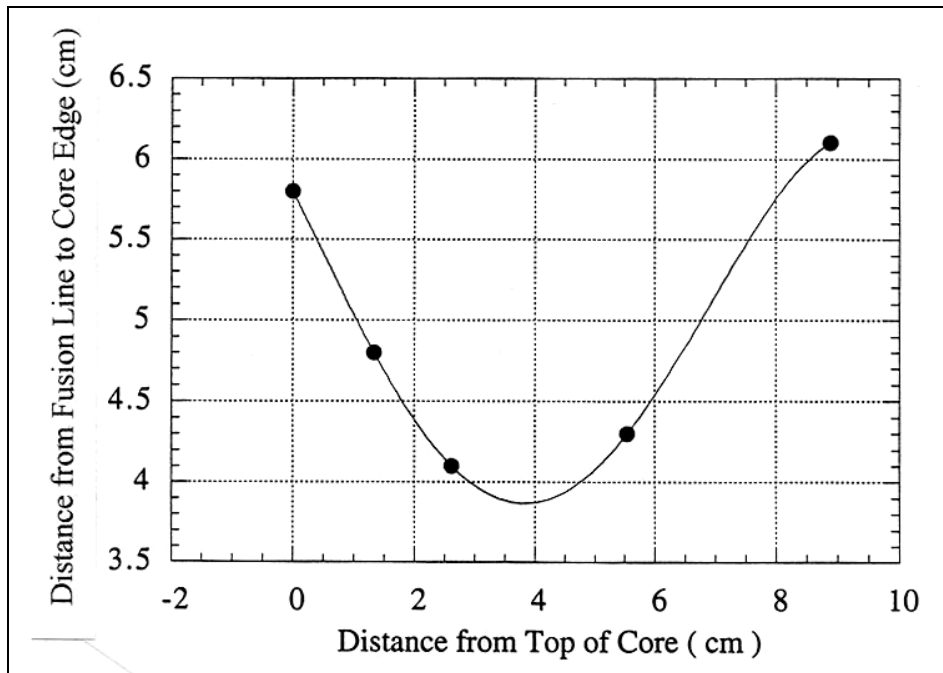
(b)D3B1

Figure 2.11: Solidification band shape for WCL cores

The through-thickness fusion line position was measured as a function of distance from the top of the core surface of HAZ core specimens (C7B1, B7B1, B7B2 B3B2 and D3B2). The results are shown in Figure 2.12a to e. The relative position of the fusion line for each etched slice surface to the core surface was measured by determining the centerline distance from fusion line to the cylindrical edge of each slice perpendicular to fusion line direction, as illustrated in Figure 2.7b.

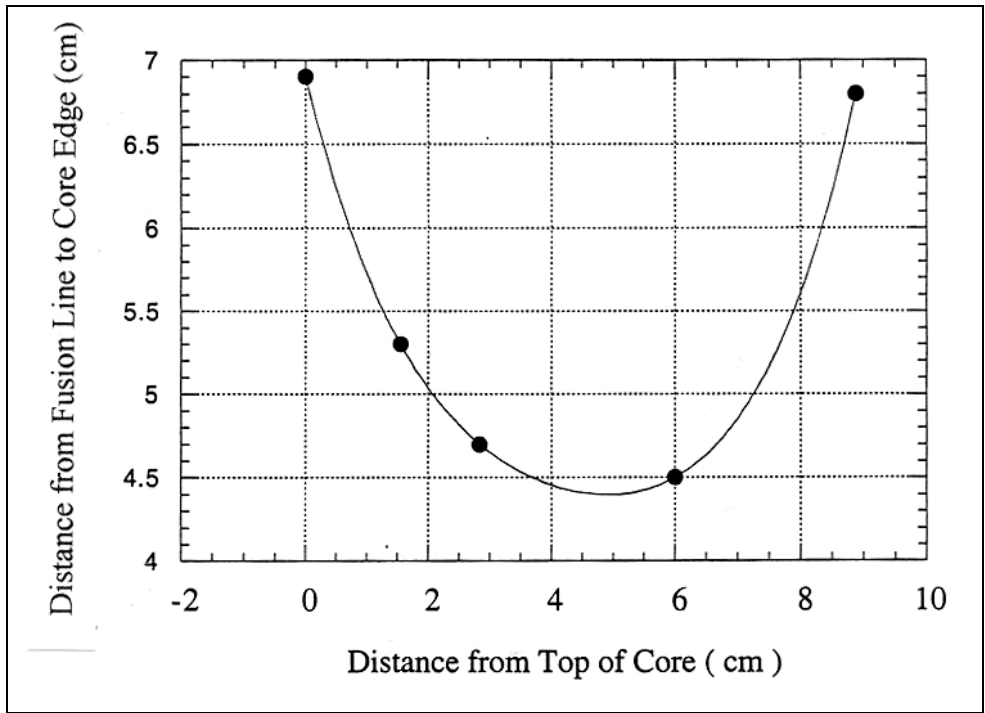


(a)C7B1

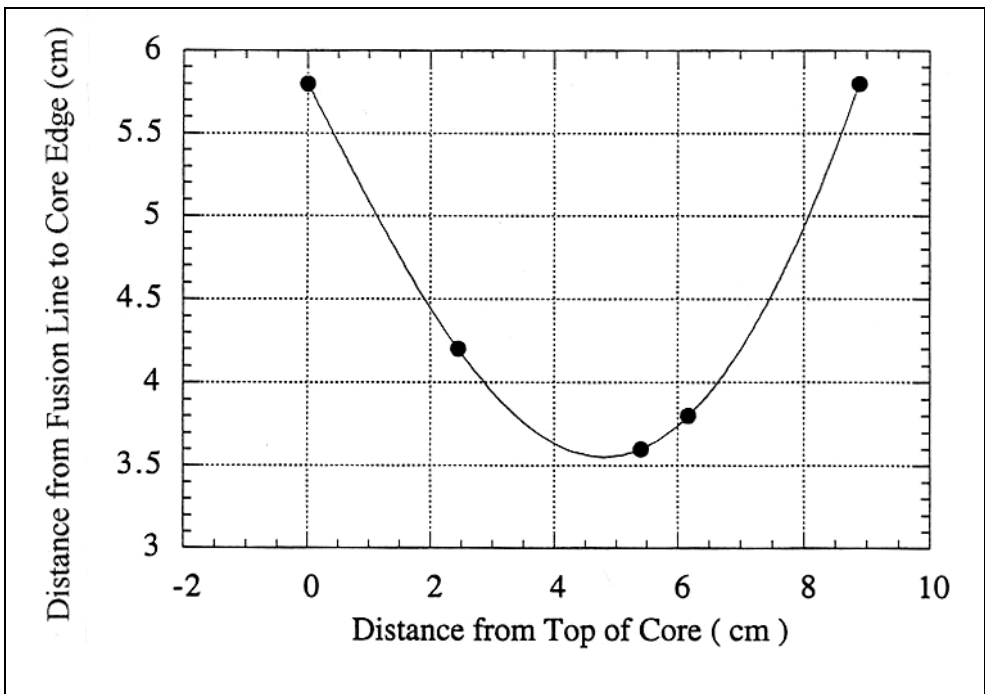


(b)B7B1

Figure 2.12: Relationship of fusion line position with thickness for HAZ cores

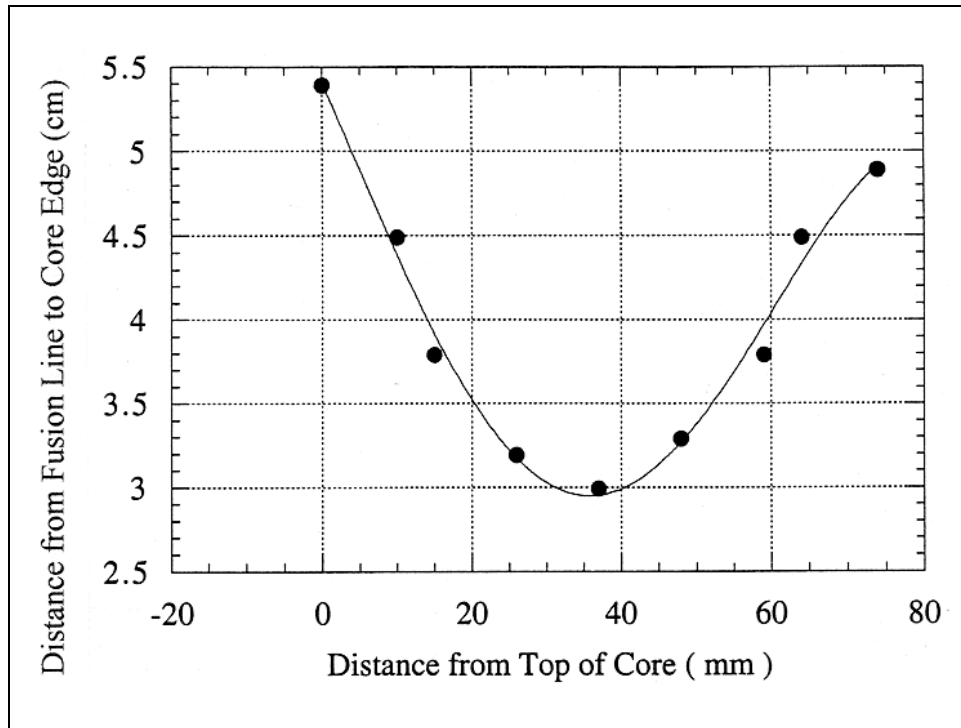


(c)B7B2



(d)B3B2

Figure 2.12 (continued): Relationship of fusion line position with thickness for HAZ cores



(e)D3B2

Figure 2.12 (continued): Relationship of fusion line position with thickness for HAZ cores

The difficulty in detecting the solidification band line varies from weld to weld. The reason for the detection difference is due to slightly different welding conditions. A major variable is differences in oscillation of the weld pool caused by mechanical oscillation of the electrode during welding. Bigger weld pool oscillation will lead to a greater distance between solidification band lines while smaller weld pool oscillation will lead to a finer solidification band structure. The greater the distance between solidification bands, the easier post-etch detection becomes. Another factor contributing to the spacing between the solidification band lines is wire guide arcing to the slag pool surface.^[27] Also the presence of double fusion lines in these welds made fusion zone size and shape interpretation difficult. This can be caused by from improper electrode oscillation during the welding process as well as in-process re-starts.

Fusion line shape reveals the operation procedure characteristics during the welding process. Weldments associated with the WCL cores appear to exhibit reasonably stable welding conditions, Figure 2.9. HAZ core specimens C7B1, B7B1, B7B2, B3B2 and D3B2 also appear to exhibit a good, steady welding process. HAZ cores D7B1 and C3B1 exhibit two different fusion line shapes at the bottom of the core, Figure 2.9. Core D7B1 has two distinct fusion line intersections with the bottom surface of the core, Figure 2.9b. This weld perturbation was probably caused by a stop and restart operation during welding process. The C3B1 core has a double fusion line near the bottom of the core, but the two fusion lines intersect at the core surface, Figure 2.9c. This weld perturbation was caused by improper electrode oscillation during the welding process.

It can be seen that the fusion line shape is not the same for all of the specimens through the thickness of the welded plate. The width of the fusion zones at the top and bottom plate surface remained nominally constant, but the mid-thickness width of the weldments was found to vary. Point P on the fusion line, as shown in Figure 2.13, defines where the weld was the widest. Assume the distance from P to a projection of the fusion line position on the top surface is PT , as defined in Figure 2.9. The measured PT values can be classified into two groups: one with $PT > 4$ cm as shown in Figure 2.10a and b, and 2.12a, c and d; the other one with $PT < 4$ cm as shown in Figure 2.12b and e. The relationship between weld number and PT values is illustrated in Figure 2.14.

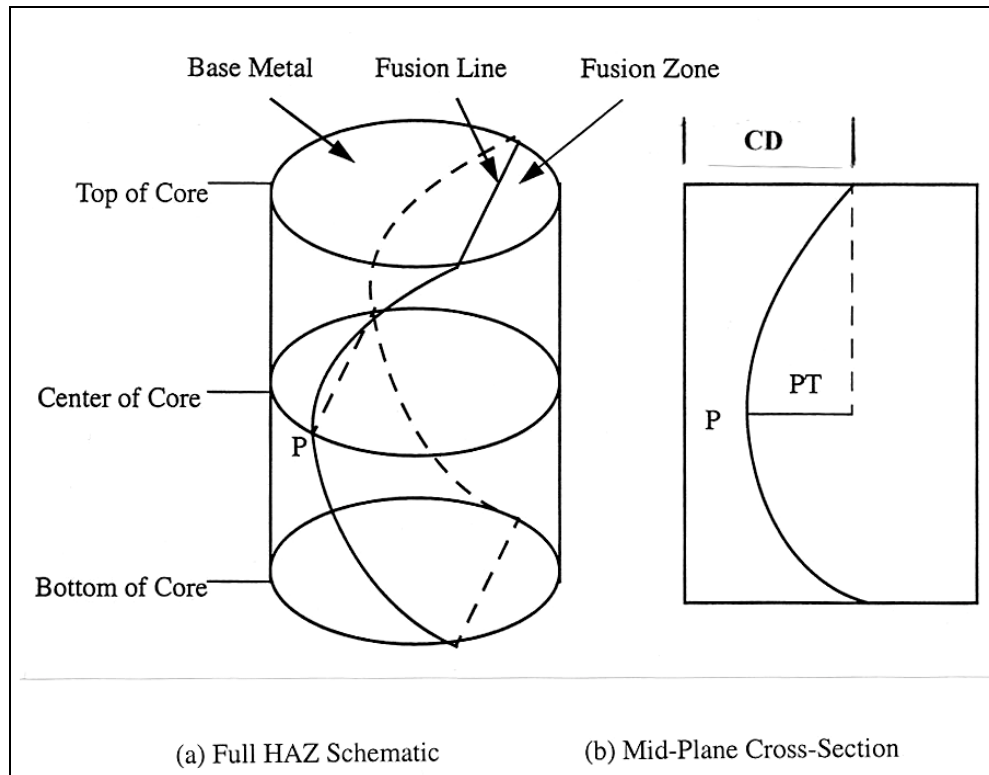


Figure 2.13: PT and CD positions for HAZ cores

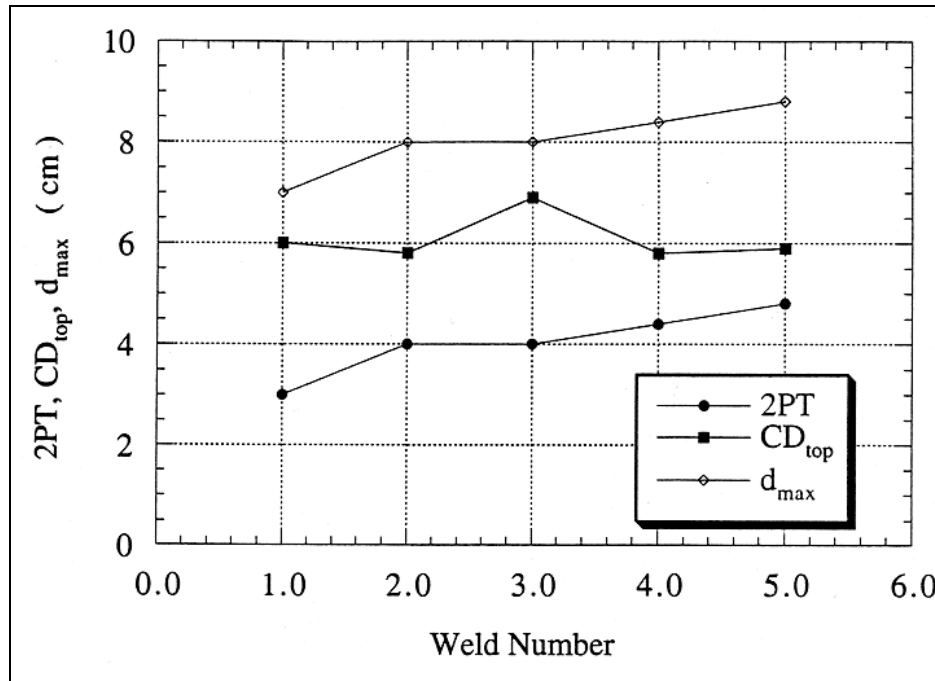


Figure 2.14: Relationship between weld number and 2pt, CD_{top} and D_{max}(C7B1, B7B1, B7B2, B3B2 and D3B2 for weld number 1 to 5 sequentially)

The fusion line shape through the thickness of the core specimens reveals the effectiveness of the heat transfer of the copper shoes during the ESW process; thus the fusion zone width (as well as the HAZ width) is smallest near the plate edge and largest at the plate center. In conjunction with the through-thickness results, the solidification band line shape reveals the heat transfer property effect along the weld pool depth direction and along the welded plate longitudinal direction. From Figures 2.10, 2.11 and 2.12, it can be seen that the fusion line shape is steeper in the through-thickness direction than along the weld pool depth direction or along welded plate longitudinal direction. That is to say, the heat loss is much greater through the copper shoes than in any other direction.

A main weld characteristic in ESW is the width of the weld b (see Figure 2.15). As applied to ESW, the term "depth of penetration" loses much of its meaning since welding is usually done in the vertical position. It is therefore legitimate to speak of the "depth of the weld pool" but not of the depth of penetration. The form factor ψ , which is the ratio of the width of the weld to the depth of the weld pool h (see Figure 2.15), is an extremely important characteristic in ESW and to a great extent determines the resistance of the weld to intergranular cracks. The width or depth of penetration can vary according to the thickness of the metal. However, if the welding procedure is correctly chosen, these variations are negligible. The weld-form factor in ESW may vary between 0.8 and 10; the mean value is 1.5 to 4. From Figure 2.11 a and b, it can be seen that the weld form factor for these tests vary in the mean value range, with b being measured along the x axis at $y=0$ and h being measured along the y axis from $y=0$ and $x=0$. The weld form factor is about 2.5 for

the B3B1 weld centerline specimen. The weld form factor is about 3.8 for the D3B1 weld centerline specimen.

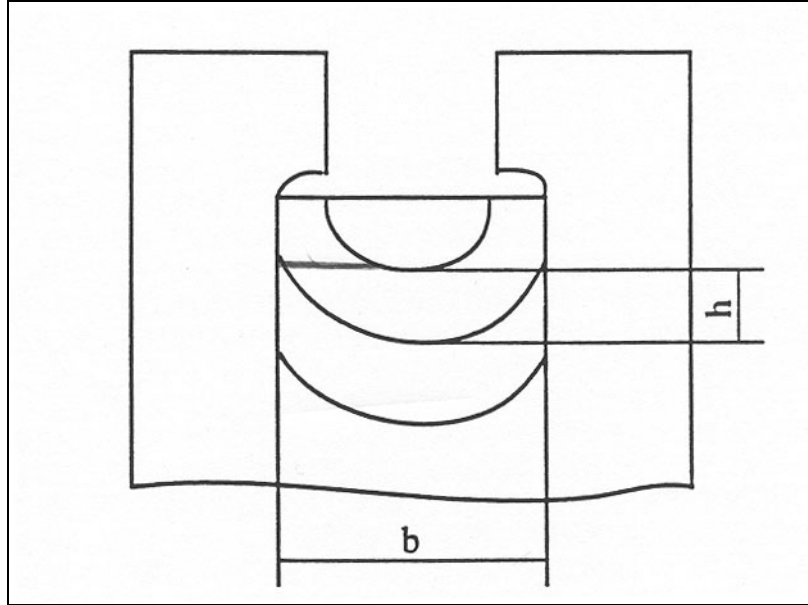


Figure 2.15: Weld pool shape during electroslag welding

From Figure 2.10, it can be seen that the narrowest width of the fusion zone is about 4 cm and the widest width of the fusion zone is about 8 cm for fusion zone cores. For the HAZ cores, the width of the widest fusion zone d_{max} can be calculated from Figure 2.12. If the fusion zone width at the top of the core is d_{min} , and if the difference between the fusion line on top and at the center of the core along the welded plate longitudinal direction is PT , then $d_{max} = d_{min} + 2PT$. The measured PT for each core is given in Table 2.2. It can be seen that $2PT$ is about 4 cm and d_{max} is about 8cm, with good agreement between weld centerline cores and HAZ cores.

Table 2.2: Difference between widest fusion zone and narrowest fusion zone $2PT$ and position of fusion line on top of HAZ specimens CD_{top}

Specimen ID	$2PT$ (cm)	CD_{top} (cm)	d_{max} (cm)
C7B1	3	6	7
B7B1	4	5.8	8
B7B2	4	6.9	8
B3B2	4.4	5.8	8.4
D3B2	4.8	5.9	8.8

The position of the fusion line on top of the HAZ specimens reveals the actual drilling position. If all of the HAZ cores had been drilled in the same position, i.e., 0.5" out from the fusion line at the center of the core, then all of the fusion line positions should have the same CD length on top of

the core. Table 2.2 also gives the value of CD length on top of HAZ cores. From the values, it can be seen that most cores were drilled at nominally the same position, with B7B2 being drilled farther away from the fusion zone than other cores. This variation is mainly due to the difficulty in determining the ESW fusion line on the plate surface in situ by macro-etching the welds. This difficulty was caused by the cosmetic weld repairs along the fusion lines on both sides of the welds to compensate for lack of fill due to poor shoe design.

2.4 CONCLUSIONS

1. The operation parameters that were used during ESW process were slightly different from weld to weld.
2. The heat loss is much greater through the copper shoes than any other direction.
3. The weld form factor is in the mean value range.
4. The widest fusion zone width is about 8cm. The fusion zone width at the surface of the welded plates is about 4 cm.
5. The depth of the weld pool at mid-thickness is expected to vary from 2.1 to 3.2 cm, based on 8 cm as average maximum width and a form factor variation of 2.5 to 3.8 cm.

3.0 NUMERICAL ANALYSIS OF RESIDUAL STRESS INDUCED BY THE ELECTROSLAG WELDING PROCESS

3.1 BACKGROUND

Beginning in the 1930's, researchers have tried to give a mathematical representation of the welding process. The work consists of two parts: heat flow analysis and thermal stress analysis. Both analytical models and numerical models have been used to predict temperatures and thermal stresses during the welding process.

Two different sets of coordinates can be used for weld modeling. One set is stationary with respect to the earth. The other coordinate set is stationary with respect to the heat source. Rosenthal^[42,43] was the first one to give a closed form solution for heat flow analysis. He argued that, in the second coordinate system, the temperature profile around the observer does not change after the initial period of welding. This phenomenon is called a quasi-steady state condition.

In many modeling situations, including welding, the governing equations may be readily derived, but their solutions by closed form methods may be difficult or impossible. With the advancement of computer technology, numerical simulation has developed quickly. It can, in principle, permit nearly any complexity to be taken into account; however, economic requirements set a limit in practical terms.^[44] Finite difference, finite element and boundary element analyses are the three strong candidates of numerical analysis. Most recent weld modeling work, as well as the work reported herein, uses the finite element method.

The weld-induced thermal history must first be modeled prior to the prediction of final residual stress state. One great advantage of numerical modeling is that it allows use of a distribution model of the heat source. However, the use of a heat distribution model requires a knowledge of the parameters used in welding and their effect on the fusion zone size and shape. This knowledge was not available for the welds under consideration for this project, so the fusion zone boundary was used as the heat input for the model work reported herein. The surface size and shape was based on the determination of the West Linn Bridge-specific ES weldment fusion zone and was defined as being at a melt temperature of 1500C. Note that the only portion of the fusion molten zone that is defined using the fusion boundary definition technique is the geometry of the fusion zone boundary. The rest of the fusion zone is not defined and, in this modeling scenario, does not exist. The prescribed temperature and natural boundary conditions are used to solve the energy equation.

Non-linear material properties have been used for the modeling work reported herein, as well as in other recent welding numerical simulation work. Room temperature material properties are

readily available for most materials. Intermediate temperature properties are available for selected materials. High temperature material properties are generally not available.

Thus high temperature material properties, which are critical for correctly modeling weldments, are generally extrapolated, estimated, and/or “adjusted” to yield model properties that match experimental results.

The predicted thermal history is used to determine elastic and plastic strains/stresses associated with welding. There are three elastic theories: elasticity, hyperelasticity, and hypoelasticity. Elasticity is based on the thermodynamic equilibrium principle. Hyperelasticity theory is based on assuming reversible thermodynamics, i.e., strain energy density is an analytic function of strain and temperature. Hypoelastic theory is based on assuming irreversible thermodynamics. The stress and strain relationship depends on the previous stress state. This theory is also called the rate theory. As for the welding process, the stress and strain relationship strongly depends on the welding procedure, stress relief, etc. So only the hypoelastic theory is applicable to the welding process.

Elasticity is only applicable for sufficiently small strains. For large strains, new phenomena occur and other theories are needed to describe them. For welding mechanics problems, a plasticity or viscoplasticity theory should be used, so a thermo-elasto-plasticity theory has been widely used to analyze welding mechanics.

At the end of the 1970's, efforts were begun to develop analytical models to predict the thermal-mechanical response of welded structures. Before that time, various approaches had been taken to establish empirical methods for understanding material behavior during welding.

Analytical models for calculating stresses during welding have been developed based on the line heat source and moving point heat source.^[45-53] These techniques generally show good agreement between residual stresses of the model and experimental data but are often limited to single pass or bead-on-plate welds. As for complex welding processes – involving irregular geometries, inelastic material response and material loading, unloading, etc. – the problem can not be solved with a closed-form solution. Numerical methods need to be used to analyze residual stress in welded structures. The finite element method has been applied to study the behavior of welded structures.

Post-weld residual stress requires the presence of plastic strain during the weld cycle. When the yield point is reached, according to the Von Mises Yield Criterion, an associated flow rule is employed to calculate incremental plastic strains. Among the kinematic hardening model, the isotropic hardening model and the isotropic-kinematic hardening model, the kinematic hardening model is used to characterize the material behavior during welding. The reasons for this are as follows:

- 1) The kinematic hardening theory is the simplest theory to simulate the reverse plasticity effect and the Bauschinger effect, which are expected to occur during welding. For this theory, work-hardening in the plastic region is linearized to be a constant.

2) Although the combined isotropic-kinematic hardening model is more accurate than the kinematic model,^[54-,55] unless more accurate stress-strain curves are available, it will not improve the accuracy of the results.

3) During the welding process, the time that the material stays at a high temperature is short, so time dependent creep effects are generally not considered.^[56]

The material properties required for the stress analysis are the elastic (Young's) modulus, Poisson's ratio, virgin yield stress (yield strength), tangent plastic modulus, and the average coefficient of thermal expansion. The molten material is assumed to re-solidify as a damage-free material, so the material properties which affects the weldments are limited to below the melting temperature only. As the properties above melting temperature have no effect on the residual stress, one only needs the temperature dependent material properties up to melting temperature.

The virgin yield stress and tangent modulus are the critical material properties. For the kinematic hardening model, the tangent modulus is set to zero at temperatures above the melting temperature so that the molten metal can re-solidify as damage-free material. The virgin yield stress at the melting temperature should be very small but not zero, which would result in a divide by zero situation. It was found that a value of about 0.5% of the room temperature value could be used above the melting temperature. The virgin yield stress value and the tangent modulus can be computed by assuming that the tangent modulus/Young's modulus ratio remains constant up to the welding temperature.

Modeling results give increasingly reasonable simulation results of residual stresses with increasing distance from the weld fusion line.^[57] This is because the weld fusion line experiences high temperature cycles during the welding process producing the highest plastic strain. At the same time, the absence of accurate thermal and mechanical material properties and accurate work-hardening data at high temperatures leads to added inaccuracy in residual stress results.

The thermal history of single-pass electroslag welds differs markedly from that of conventional multi-pass arc welds. That leads to the potential for using different analysis methods. Electroslag welding began in the 1950's, but low fracture toughness in the fusion and heat affected zones restricted its wide use. Thus the modeling work on the ESW process is not as detailed as for the arc welding processes.

The most detailed modeling work of the ESW process has been done by Dilawari, Szekely, and Eagar of M.I.T. Their work can be divided into two parts. One part emphasizes the role of the electromagnetic and buoyancy fields in determining the velocity and temperature profiles of the molten metal in the weld pool^[58,59]. In this part of their work, idealized two-dimensional (axisymmetrical or plate-like) systems have been used. (see Figure 3.1). The rectangular system modeled is a reasonably good approximation of electroslag welding with a strip electrode. Only the shape of the metal pool appears to be over-idealized.

It was found that the buoyancy and electromagnetic forces produce vigorous agitation in the molten weld pool. The nature of this agitation is markedly affected by the geometry. When the current field is non-parallel, as in the case of wire electrodes, the electromagnetic force field

plays a major role, while for parallel fields, as produced by flat plates, the flow field is driven essentially by buoyancy forces. This part of the work established the existence of vigorous agitation in the weld pool and indicated the important role played by the system geometry.

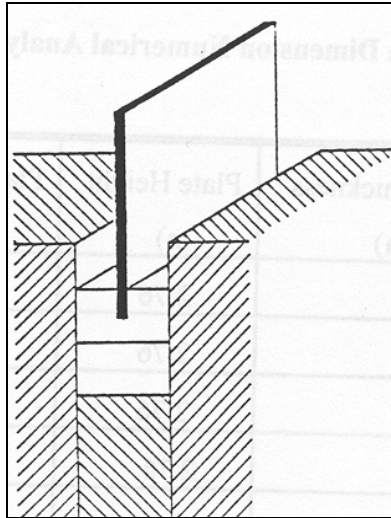


Figure 3.1: Schematic representation of plate electrode

The other part of their work uses three-dimensional modeling to examine the heat generation patterns and the resultant temperature distribution in the molten slag, the metal pool, heat affected zone and base metal^[60,61]. The idealized three-dimensional model for heat flow analysis is schematically illustrated in Figure 3.2. However, their work did not consider the phase transformation effect during heat flow, and the shape of the molten pool is idealized in their model. At the same time, all of their modeling work is based on known welding operation parameters and their effect on slag/weld pool shape.

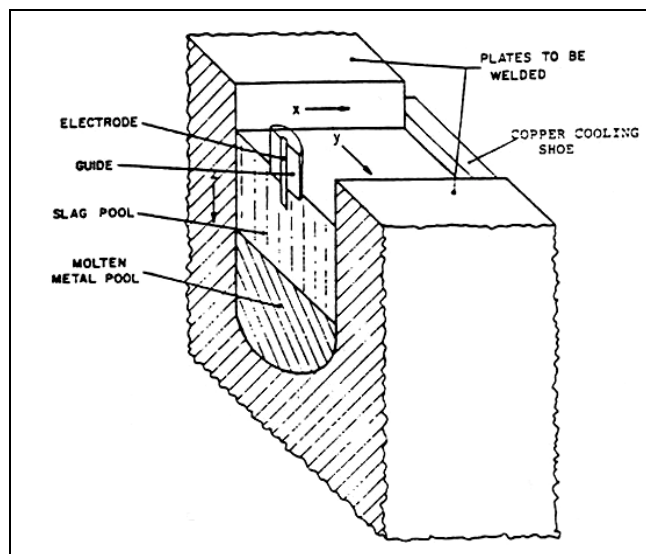


Figure 3.2: Schematic representation of 3-D model

3.2 PROGRAMMATIC COMPUTATIONAL MODELING OVERVIEW

Programmatic 2D fixed coordinate system modeling of the ESW process was carried out using the ANSYS commercial finite element computer code, while the 3D fixed coordinate system model was also being developed using ANSYS^[62]. The reason ESW was first modeled using 2D versus 3D was due to model development simplification issues and the expectation that full 3D model calculation would quite possibly be too time consuming to allow sufficient model iteration to bound the desired parametric study. It was hoped that parametric changes could be assessed using 2D modeling and selected 3D model results could be used to bench mark the 2D results.

Initial 2D and 3D modeling calculations were done using the classical fixed (Langrangian) coordinate method. This modeling coordinate system yields modeling results directly comparable to the actual physical weldment set-up. Specifically, the heat source moves from the bottom to the top of the plate. The heat source then extinguishes, and the plate is allowed to cool down naturally. Thus, this type of coordinate system allows one to model initial start-up conditions, central portion steady state conditions, and shut down conditions.

Two 2D models were developed. One was a cross-sectional model and the other was a mid-plane model. Each 2D model only partially characterizes the ESW process with other significant effects being ignored. The mid-plane model does not consider the effect of copper shoes which are pressed against the plate surface during welding and are a significant heat sink. The cross-sectional model does not consider the thermal conductivity or restraint due to the plate material above or below the plane of the weld. The results of the 2D model work is discussed in detail in Zhang's Ph.D. thesis.^[63]

The discrepancies found between the 2D model results led to the determination that 3D modeling must be used to realistically model ESW.^[63] A 3D thermal model was successfully developed in fixed coordinates using ANSYS with a run time of over two weeks. However, 3D thermally-induced strain calculation modeling using the fixed coordinate system proved to take entirely too long to be practical for parametric change assessment. It is estimated that a complete 3D mechanical calculation would take over a month to complete using the OGI dedicated workstation. Thus a different methodology for conducting 3D strain/stress calculations was sought.

Becker et. al. illustrated that a moving (Eulerian) coordinate system could be used for steady state problem conditions^[64,65]. Here the heat source stays stationary, and the plate to be welded moves by the heat source. Thus, the classical fixed coordinate of weld length becomes a "time after the heat source has passed" coordinate axis, Figure 3.3. This technique improved accuracy and greatly increased computational speed compared to using a fixed coordinate system. Thus it was decided to conduct ESW strain/stress calculations as well as thermal history predictions using the moving coordinate system.

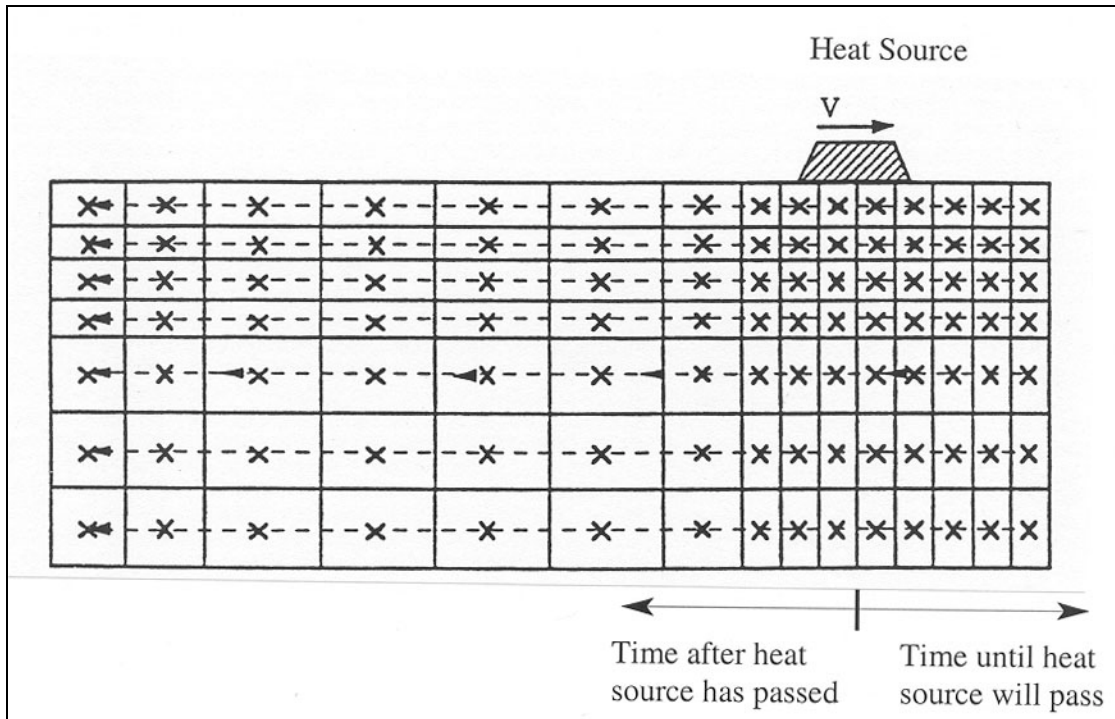


Figure 3.3: Schematic illustration of the Eulerian coordinate system trajectory motion in the case of a welding process

3.3 MOVING COORDINATE SYSTEM IN WELD MODELING

The use of the moving coordinate system to solve weld-oriented heat transfer problems was started in 1941 by Rosenthal.^[42,43] He was the first one to use the moving coordinate system to get an analytic solution for the heat transfer problem with a moving point heat source. A review of the open literature on the moving coordinate system to get analytical solutions was given by Radaj^[66] in 1992. It reveals that when a thermal process involves movement of a heat source at a constant velocity, the analysis may be changed from a dynamic condition to an equivalent, steady-state condition. The time derivatives can be replaced by equivalent spatial derivatives. In practice, steady-state, continuous processes are very common, i.e. welding, joining, brazing and continuous casting.

Because of its direct relationship to reality and the limited number of codes capable of implementing moving coordinate problems, most finite element analysis is based on the fixed coordinate system. Fixed coordinate system problems require a very dense mesh around the heat source along the complete heat source path. Moving coordinate system problems require much less data storage capacity because the very dense mesh is only needed at the one location where the heat source is positioned. At the same time, with fewer nodes, fewer element numbers and use of the steady-state calculational condition (instead of the transient analysis calculational condition for the fixed coordinate system), the computational time is dramatically reduced. In addition, the moving coordinate system is more accurate when compared with a comparable

fixed coordinate system problem in simulating heat source movement activity.^[64,65] This is because the moving coordinate system simulates the heat source moving continuously, which is the true case in practice, while the fixed coordinate system requires the heat source to move in jumps as a function of time in order to move it along the heat source path. Thus the fixed coordinate system simulates the process with many time steps. During each time step the problem is calculated in the fixed state. In order to be close to the real continuous moving process, fine time steps are required, which increases the computational time as described previously.

To analyze heat transfer, stress, and strain, Bergheau and Leblond incorporated moving coordinates into the computer code SYSWELD used by the French company FRAMASOFT/CSI.^[67] The first result they reported was the application of laser surface treatment. The moving reference frame enables one to connect nodes and elements in order to account for a rate.^[68] Thus, the metallurgical and mechanical equations are not solved in the fixed coordinate system but in a moving coordinate system. Figure 3.3 illustrates the procedure, which is based on the definition of element trajectories and on integration point trajectories. The trajectories are parallel to the heat source moving direction. In this way, the thermal and mechanical history of each point in the structure can be determined and accounted for. The non-linear, thermal equations are solved by changing the time derivative to a spatial derivative. With the thermal results, the mechanical equations are solved with help of a procedure which defines each integration point sequence. The initial values are those of the previous integration point if the moving direction of the material is considered.

Gu, Goldak and Hughes reported the results of thermal analysis in a moving coordinate system using the finite element method^[69-71]. They assumed that the material properties were not dependent on temperature and position of the structure, i.e., uniform material properties. With these assumptions, the following equation can be applied to heat transfer analysis.

$$T = T_0 + \phi \exp\left(\frac{vx}{2\alpha}\right) \quad (3-1)$$

where,

T = Temperature

T_0 = Initial temperature

ϕ = Variable

v = Speed of heat source

x = Dimension value along x coordinate system

α = Thermal diffusivity

The analysis involved symmetric matrices and was conducted with a conventional computer code. The authors compared an analysis using a moving heat source within a fixed coordinate system with an analysis using a steady-state temperature profile within a moving coordinate system. With the moving coordinate system, the calculation efficiency dramatically increased, and the results were accurate enough to be accepted.

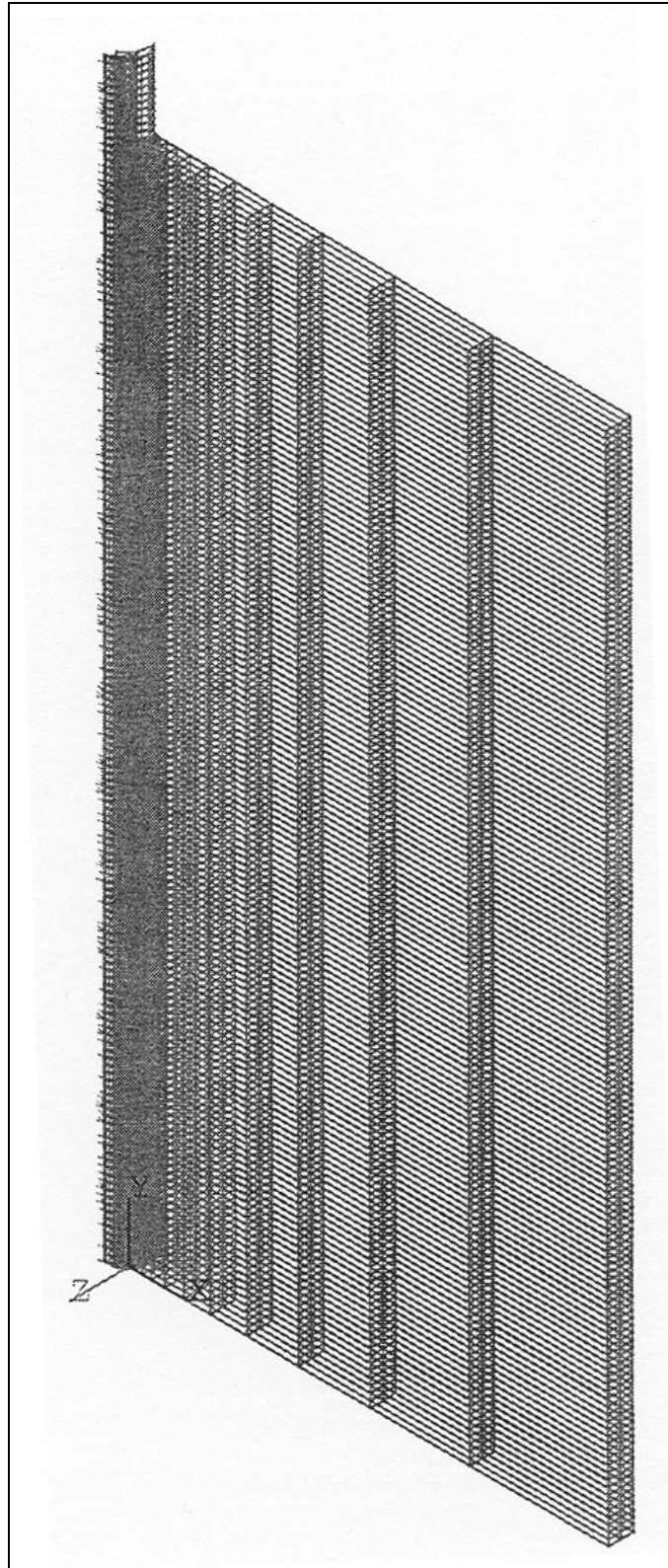
3.4 COMPARISON OF FIXED AND MOVING COORDINATE SYSTEMS IN 3D THERMAL MODELS

The desire to use a moving coordinate system versus a fixed coordinate system resulted in the need to compare comparable results from both coordinate systems as well as to assess the use of alternative commercial finite element codes. Becker used the ANSYS fluid flow option to simulate moving coordinates for thermal analysis.^[64,65] The difficulty with continuing programmatic work using ANSYS was that the moving coordinate, thermal analysis results could not be used as input into the ANSYS mechanical solver. Consequently, ANSYS could be used for thermal history assessment but not for residual stress analysis. However, moving coordinate programming options are built directly into the SYSWELD thermal/mechanical programming options.^[68] Thus, SYSWELD was used to assess ESW-induced residual stress.

It was first desired to validate the use of the moving coordinate system by comparing it with results from the fixed coordinate system. Three-dimensional, fixed coordinate system thermal history calculations for the work herein were first done using ANSYS. These results were then compared to 3D thermal moving coordinate system results done using ANSYS. Next, the ANSYS 3D moving coordinate thermal history results were compared to SYSWELD 3D moving coordinate thermal history results.

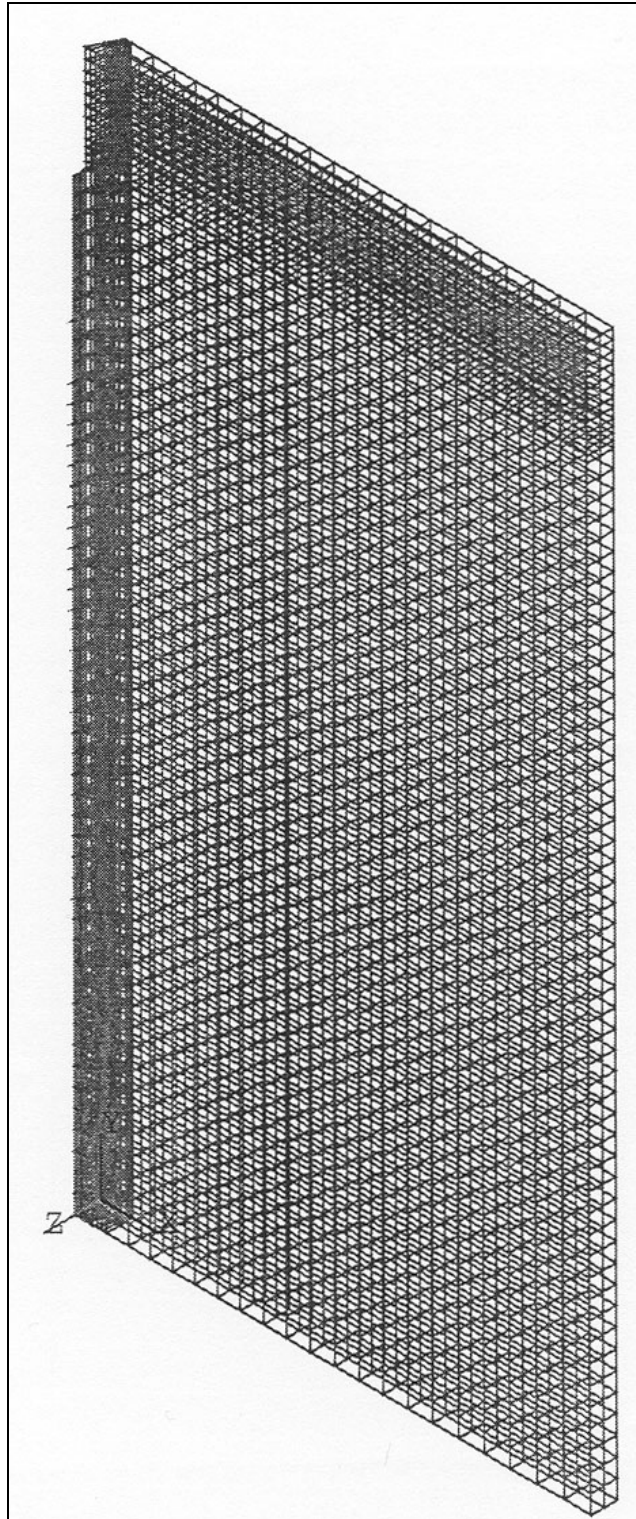
The fixed and moving coordinate models for the ANSYS and SYSWELD programs had different mesh densities but the same basic model geometry, as illustrated in Figures 3.4 and 3.5. As for mesh, weld metal and HAZ regions were discretized with smaller elements than regions far from the heat source. Both the height of the weldment and the effect of the copper shoe were simulated in the static coordinate ANSYS 3D model. The effect of the copper shoe and the time after welding at a specific location in the welded plate were simulated in the moving coordinate ANSYS and SYSWELD 3D models. The effect of the copper shoes was simulated with a high heat transfer coefficient.

The shape of the heat source remained the same for every increment of time for the fixed coordinate system analysis. A non-uniform mesh with 5568 elements and 8901 nodes was generated over the domain for the fixed coordinate, ANSYS model, Figure 3.4a. A non-uniform mesh with 3476 elements and 5490 nodes was used in the moving coordinate, ANSYS model, Figure 3.4b. A non-uniform mesh with 8112 elements and 10650 nodes was used for the SYSWELD models, Figure 3.4c.



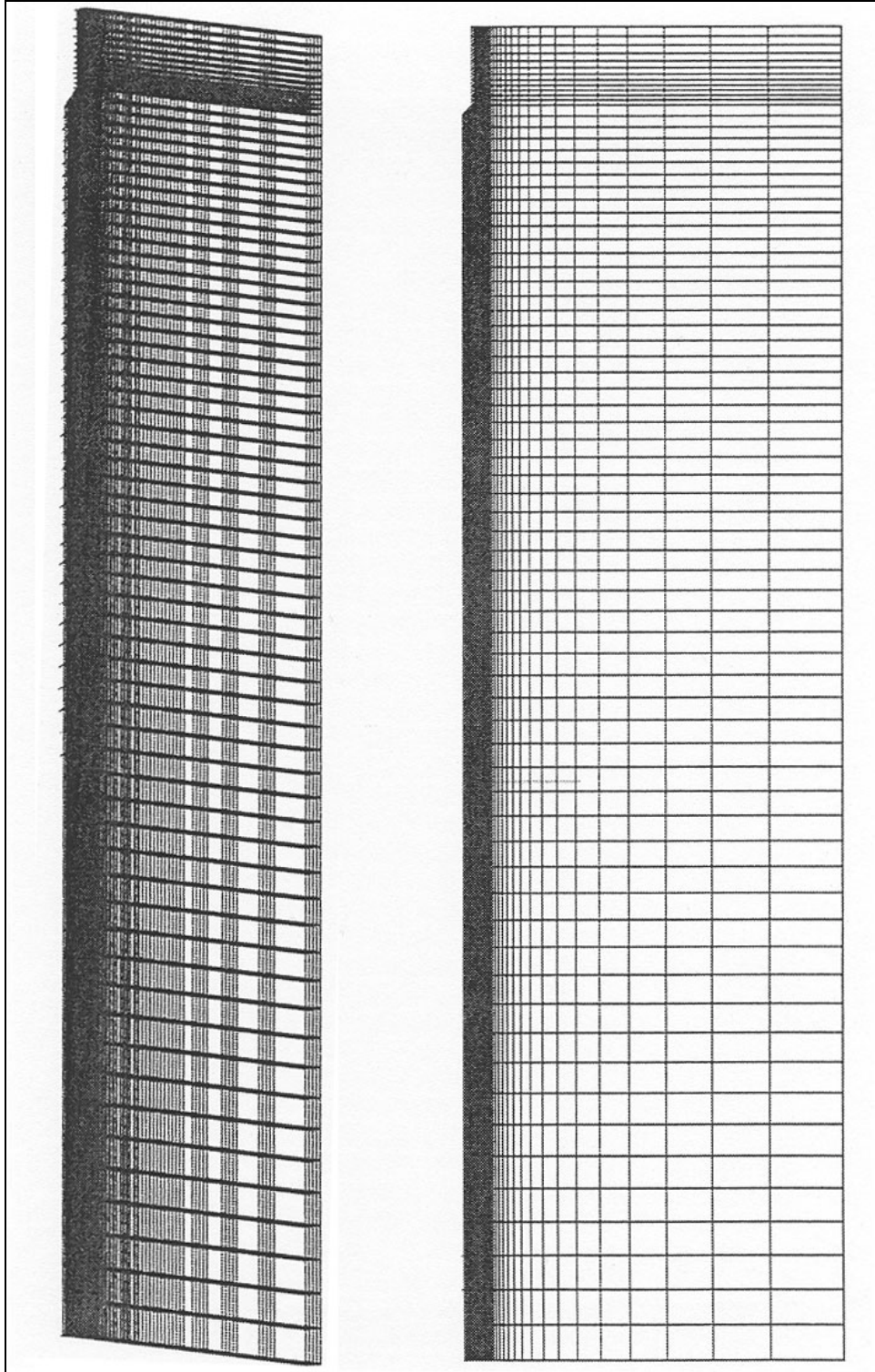
(a)ANSYS fixed coordinate model

Figure 3.4: Mesh for ANSYS fixed and moving coordinate system and SYSWELD moving 2D thermal calculation models



(b)ANSYS moving coordinate model

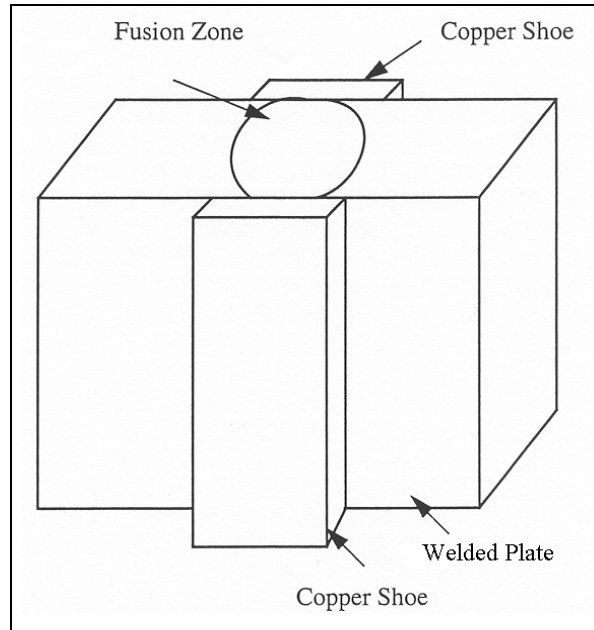
Figure 3.4 (continued): Mesh for ANSYS fixed and moving coordinate system and SYSWELD moving 2D thermal calculation models



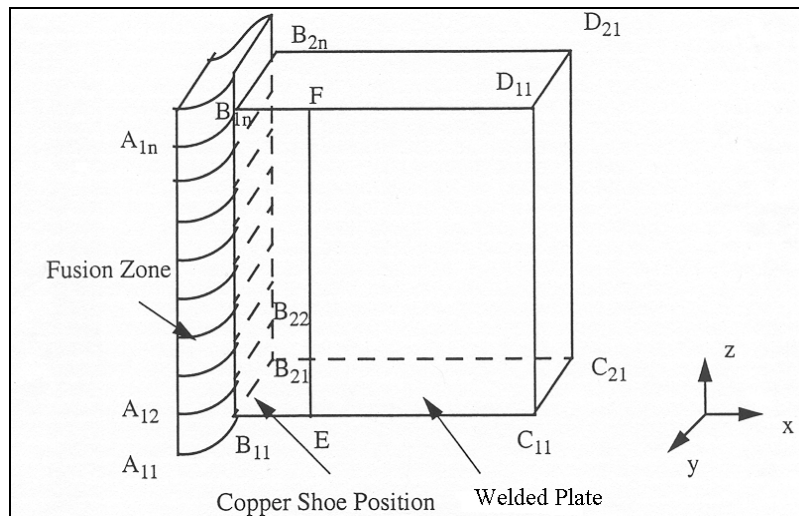
(c)SYSWELD moving coordinate model

Figure 3.4 (continued): Mesh for ANSYS fixed and moving coordinate system and SYSWELD moving 2D thermal calculation models

Only a part of the welded plate was modeled, i.e., a quarter of the welded plate was used in 3D models in order to save calculation time. Plane $A_{11}A_{1n}A_{21}A_{2n}$ and Plane $B_{2n}D_{21}C_{21}B_{21}$ are the WCL and mid-plane symmetric planes, respectively, in the models, Figure 3.5b and c. Plane $C_{11}D_{11}D_{21}C_{21}$ is not the actual end of the welded plate. The heat flow behavior through the unmodeled part of the welded plate was simplified by utilizing a heat convection boundary condition. The only additional step necessary was to calculate the convection coefficient from the conductivity and length of the welded plate, i.e., $h=k/L$ was prescribed as the convection coefficient on the $C_{11}D_{11}D_{21}C_{21}$ plane, where k is the thermal conductivity and L is the unmodeled plate length.

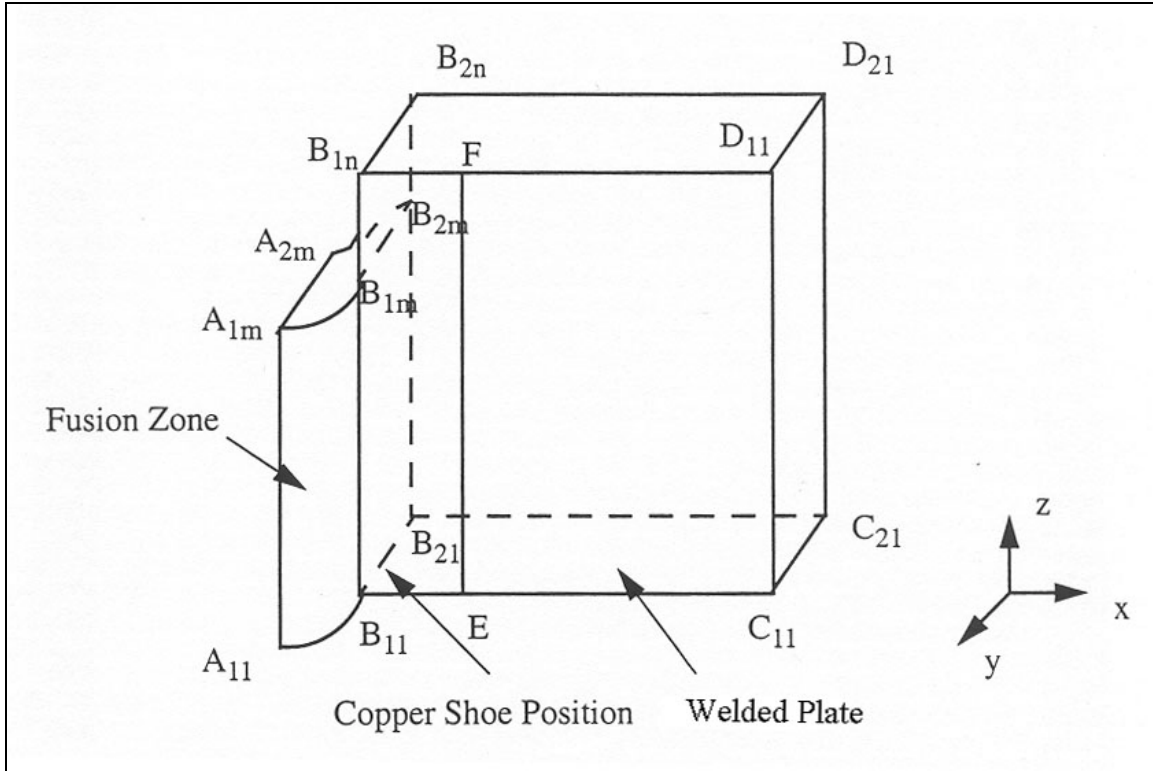


(a)ESW schematic



(b)Fixed coordinate system model

Figure 3.5: Illustration of the 3D model geometry for the fixed and moving coordinate Systems



(c) Moving coordinate system model

Figure 3.5 (continued): Illustration of the 3D model geometry for the fixed and moving coordinate Systems

The heat source distribution can be modeled by utilizing the essential boundary condition $T(x, y, z) = T_s(x, y, z)$. The melting temperature of the welded plate is represented by $T_s(x, y, z)$. That is to say, a temperature boundary versus a heat flux heat source model was used in this study.

For example, the nodes on both the $A_{12}A_{22}B_{12}B_{22}$ and $B_{11}B_{12}B_{21}B_{22}$ planes where the heat source was positioned at a certain time step in Figure 3.4b were prescribed as the melting temperature of the metal for the fixed coordinate model. Just one heat source was present in the moving coordinate model, see Figure 3.5c. The nodes on both the $A_{1n}A_{2n}B_{1n}B_{2n}$ and $B_{11}B_{12}B_{21}B_{22}$ planes where the heat source was positioned were set at the prescribed melting temperature of the metal.

The welding process was modeled in moving coordinates with the following assumptions:

1. The melting point of the metal was used as the boundary conditions at the contact layers between molten metal/base metal, molten metal/plate, and molten slag/plate.
2. The heat generated by the deformed solid was negligible.
3. All of the thermal coefficients that were used in this study remained constant throughout the welding process simulation.
4. The material was isotropic and homogeneous.

5. The piece was infinite except in the directions specifically noted.
6. Welding conditions analyzed remained steady with time, i.e., this was a representation of being in the middle of a long weld where heat input, travel speeds, etc. are constant.
7. The heat source was assumed to be a zero-volume area.
8. There was no Joule ($I^2 R$) heating.

All of the above conditions except (6), the condition of steady state, were assumed for the fixed coordinate models as well.

The fundamental principle for the heat flow analysis used in the fixed coordinate system was as follows:

$$\frac{\partial}{\partial x} (K_x \frac{\partial T}{\partial x}) + \frac{\partial}{\partial y} (K_y \frac{\partial T}{\partial y}) + \frac{\partial}{\partial z} (K_z \frac{\partial T}{\partial z}) + Q = \rho C \frac{\partial T}{\partial t} \quad (3-2)$$

where,

Q = Internal heat generation rate per unit volume (w/m^3)

K_x, K_y, K_z = Thermal conductivities along x, y and z principal axes direction respectively ($W/m \text{ } ^\circ C$)

ρ = Density of material (kg / m^3)

C = Mass specific heat ($J / kg \text{ } ^\circ C$)

With the moving coordinate system, the time derivative can be replaced by the spatial derivative:

$$\rho C \frac{\partial T}{\partial t} = \rho C v \frac{\partial T}{\partial x} \quad (3-3)$$

where,

T = Temperature ($^\circ C$)

v = Heat source moving velocity (m/s)

x = Dimensional value along x coordinate system (m)

ρ = Density of material (kg / m^3)

C = Mass specific heat ($J / kg \text{ } ^\circ C$)

t = Time (s)

With Equation 3-3, Equation 3-2 can be rewritten as the following equation:

$$\frac{\partial}{\partial x} \left(K_x \frac{\partial T}{\partial x} \right) + \frac{\partial}{\partial y} \left(K_y \frac{\partial T}{\partial y} \right) + \frac{\partial}{\partial z} \left(K_z \frac{\partial T}{\partial z} \right) + Q + \rho C v \frac{\partial T}{\partial x} = 0 \quad (3-4)$$

where,

Q = Internal heat generation rate per unit volume (W/m^3)

K_x, K_y, K_z = Thermal conductivities along x, y and z principal axes direction respectively ($\text{W/m}^\circ\text{C}$)

ρ = Density of material (kg/m^3)

C = Mass specific heat ($\text{J/kg}^\circ\text{C}$)

T = Temperature ($^\circ\text{C}$)

v = Heat Source moving velocity (m/s)

x = Dimensional value along x coordinate system (m)

The heat transfer field equation was solved under the given initial and boundary conditions. Essential natural and adiabatic boundary conditions were used during the thermal analysis. Only symmetry boundary conditions were used for the mechanical analysis.

Room temperature ($T=298\text{ K}$) was prescribed to all points in the domain except the points at the heat source boundary as the initial condition for the thermal calculation. The melting temperature of the welded plate, $T=1773\text{ K}$, was prescribed at the heat source boundary. That is to say, a temperature boundary versus a heat flux heat source model was used in this study.

The heat transfer through the surrounding medium was specified through the heat transfer coefficients:

$$K_n \frac{\partial T_s}{\partial n} + h_c (T_s - T_A) = 0 \quad (3-5)$$

where,

K_n = Thermal conductivity normal to the surface

h_c = Film coefficient for convectional heat transfer at the boundary

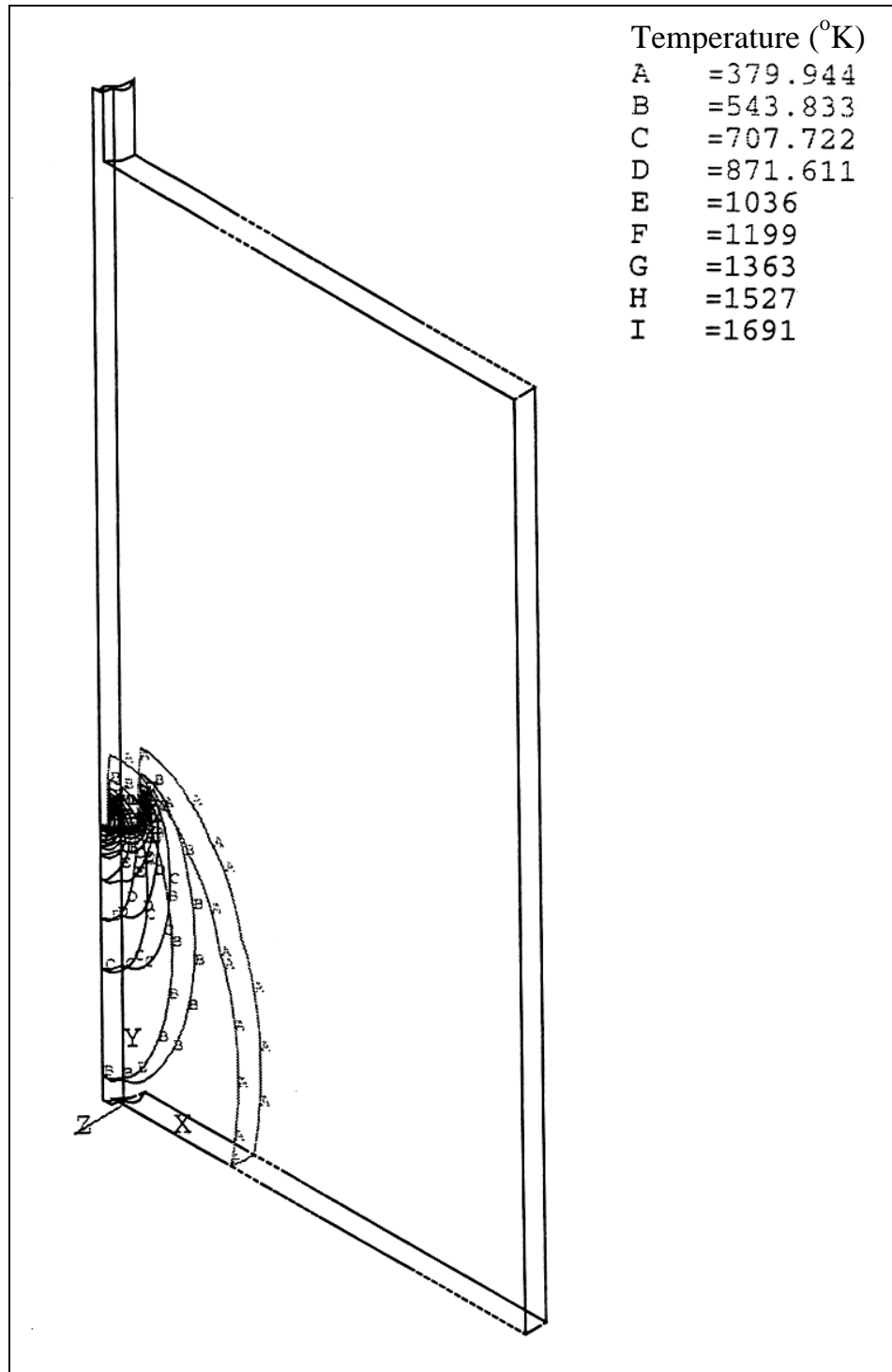
T_s = Surface temperature

T_A = Ambient temperature

The convection heat transfer boundary condition for the fixed coordinate model, Figure 3.5b, was prescribed by the $B_{12}B_{22}B_{1n}B_{2n}$, $B_{1n}B_{2n}D_{21}D_{11}$, $D_{11}D_{21}C_{21}C_{11}$, $B_{21}C_{21}C_{11}B_{11}$ and $B_{1n}D_{11}C_{11}B_{11}$ planes when the heat source was at the position on the $A_{11}A_{21}B_{11}B_{21}$ surface and $B_{11}B_{12}B_{21}B_{22}$ plane. The convection heat transfer boundary condition for the moving coordinate system analysis model (Figure 3.5c) was prescribed by the $B_{1m+1}B_{1n}B_{2m+1}B_{2n}$, $B_{1n}B_{2n}D_{21}D_{11}$, $D_{11}D_{21}C_{21}C_{11}$, $B_{21}C_{21}C_{11}B_{11}$, $B_{1n}D_{11}C_{11}B_{11}$, and $A_{11}B_{11}A_{1m}B_{1m}$ planes. A higher thermal coefficient was used in the copper shoe area to simulate the effect of copper shoe as mentioned above. According to Eagar's temperature field calculation results, a convective heat transfer coefficient value of 130 J/msK on $A_{1n}B_{1n}B_{11}A_{11}$, $A_{1m}B_{1m}B_{11}A_{11}$ and $B_{1n}FEB_{12}$ planes was used in this study; a value of 84 J/msK was used for the rest of the plate surface^[60-62]. The $A_{1n}B_{1n}B_{11}A_{11}$ and $B_{1n}FEB_{12}$ planes located the position where the copper shoe was pressed to the welded plate for the fixed coordinate system analysis model. The $A_{1m}B_{1m}B_{11}A_{11}$ and $B_{1n}FEB_{12}$ planes located the position where the copper shoe was pressed to the welded plate for the moving coordinate system analysis model. The $B_{1n}FEB_{12}$ plane was the position where the copper shoe contacted the base metal and the $A_{1n}B_{1n}B_{11}A_{11}$ and $A_{1m}B_{1m}B_{11}A_{11}$ planes located the position where the copper shoe contacted the fusion zone.

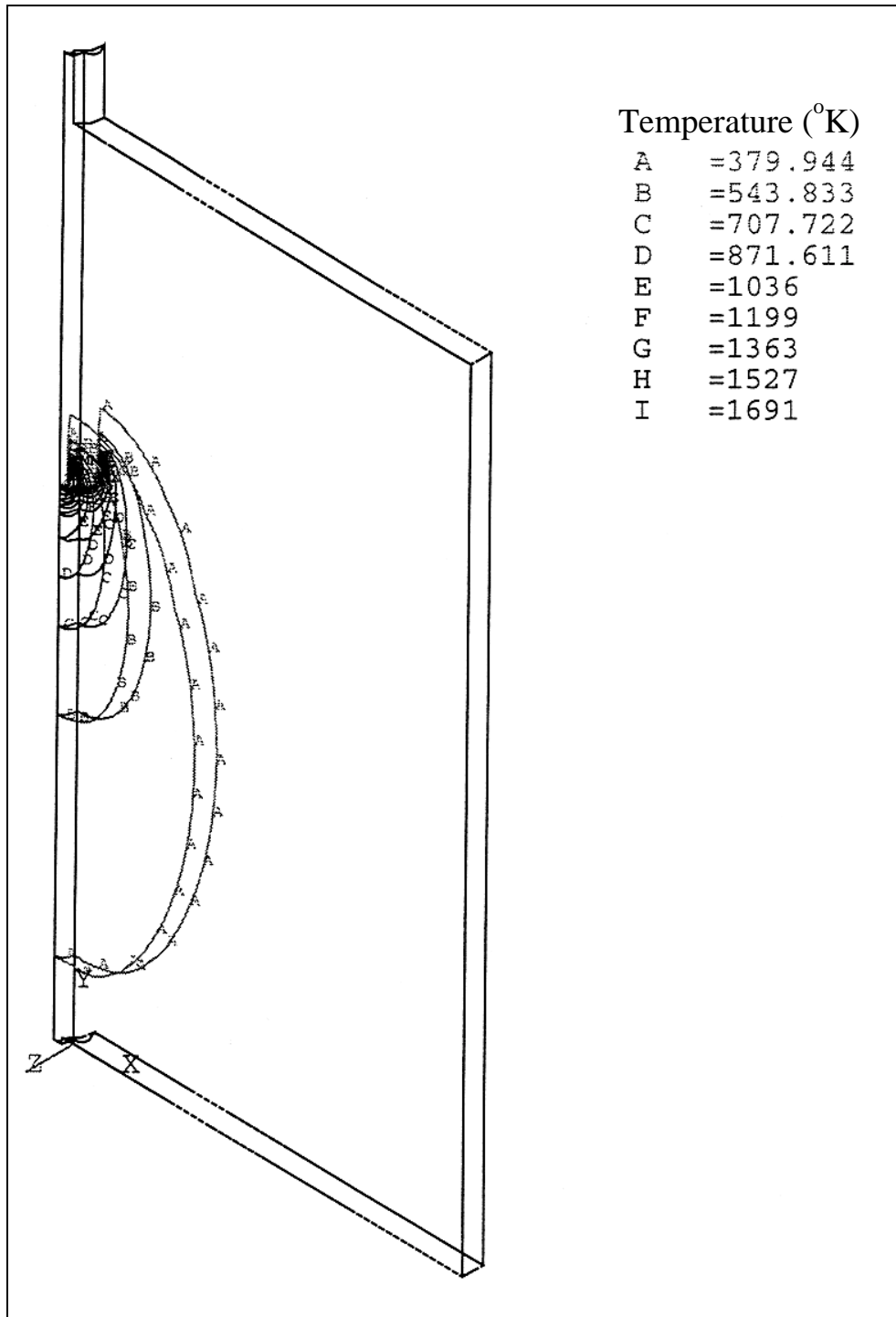
The symmetry surfaces in the ANSYS and SYSWELD program were prescribed by the adiabatic boundary condition. Planes $A_{11}A_{1n}A_{21}A_{2n}$ and $B_{2n}D_{21}C_{21}B_{1n}$ for both models were the symmetry planes where adiabatic boundary conditions were prescribed.

The temperature profiles for the ANSYS fixed coordinate system and the moving coordinate system during the welding process are shown in Figures 3.6 and 3.7 respectively. Note that the yz plane defined the WCL while the XY plane defined the weld mid-plane. From Figure 3.6, it can be seen that the temperature profile around the heat source was nominally the same for the different time steps when the heat source moved from plate bottom to plate top. It was consistent with the assumption of steady-state heat transfer for the majority of the ES weldment plate length. Figure 3.7 illustrates the temperature profile for the moving coordinate calculation system. The results were comparable with the fixed coordinate system, but the calculation time for the fixed coordinate system was more than one hundred times that of the moving coordinate system.



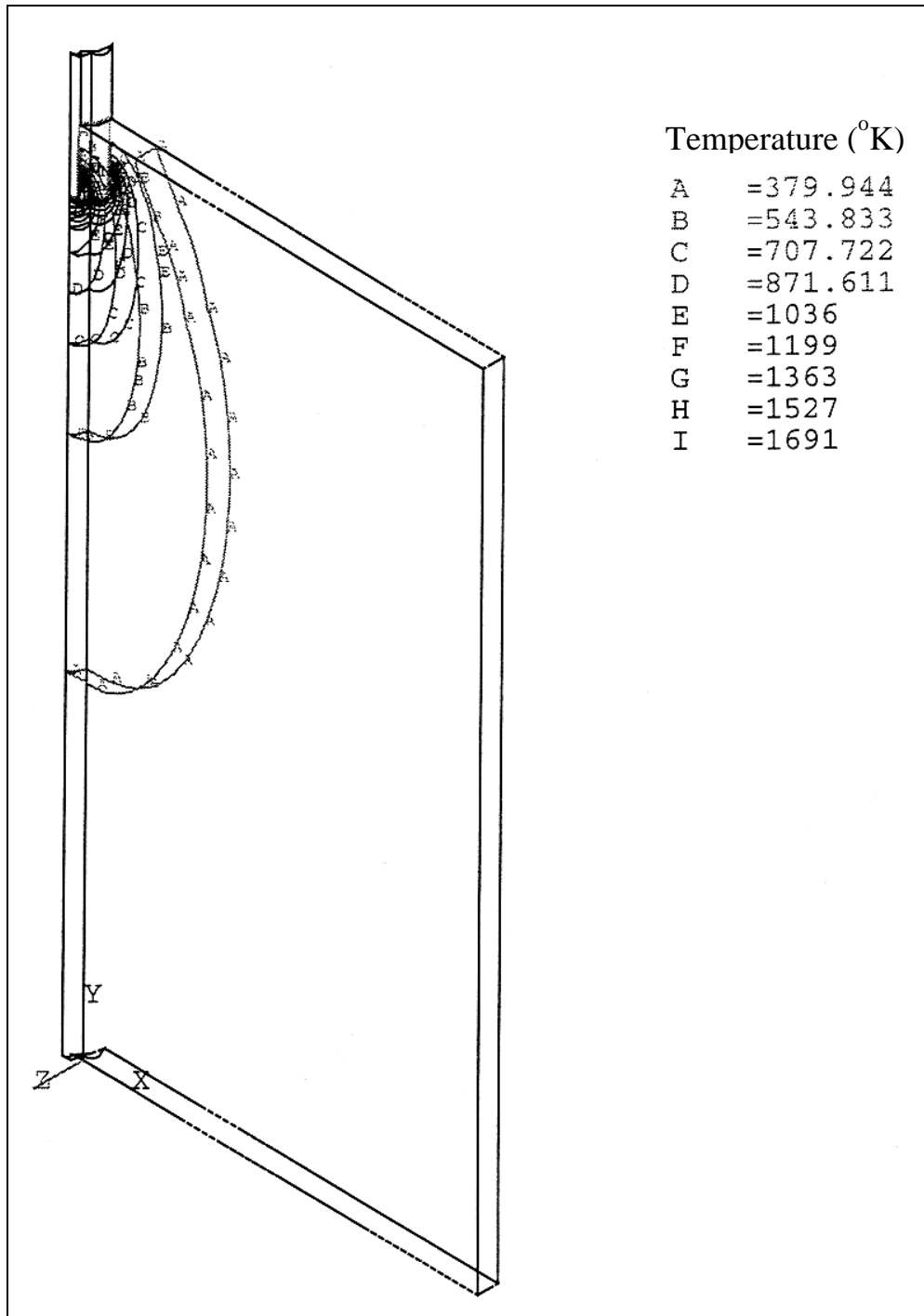
(a)Time = 1600 seconds

Figure 3.6: Temperature profiles for ANSYS fixed coordinate system thermal model calculations as a function of time after weld initiation



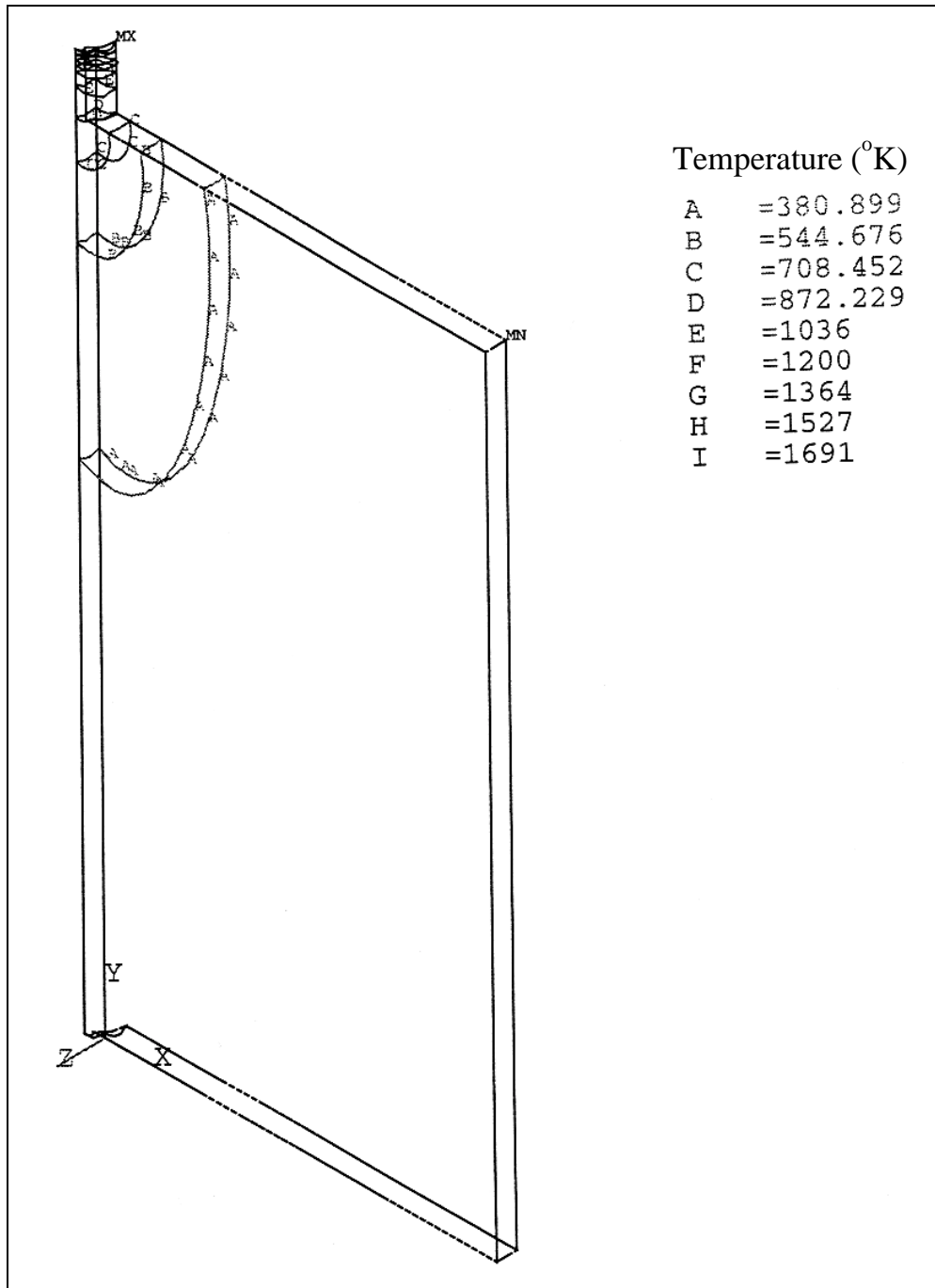
(b)Time = 3200 seconds

Figure 3.6 (continued): Temperature profiles for ANSYS fixed coordinate system thermal model calculations as a function of time after weld initiation



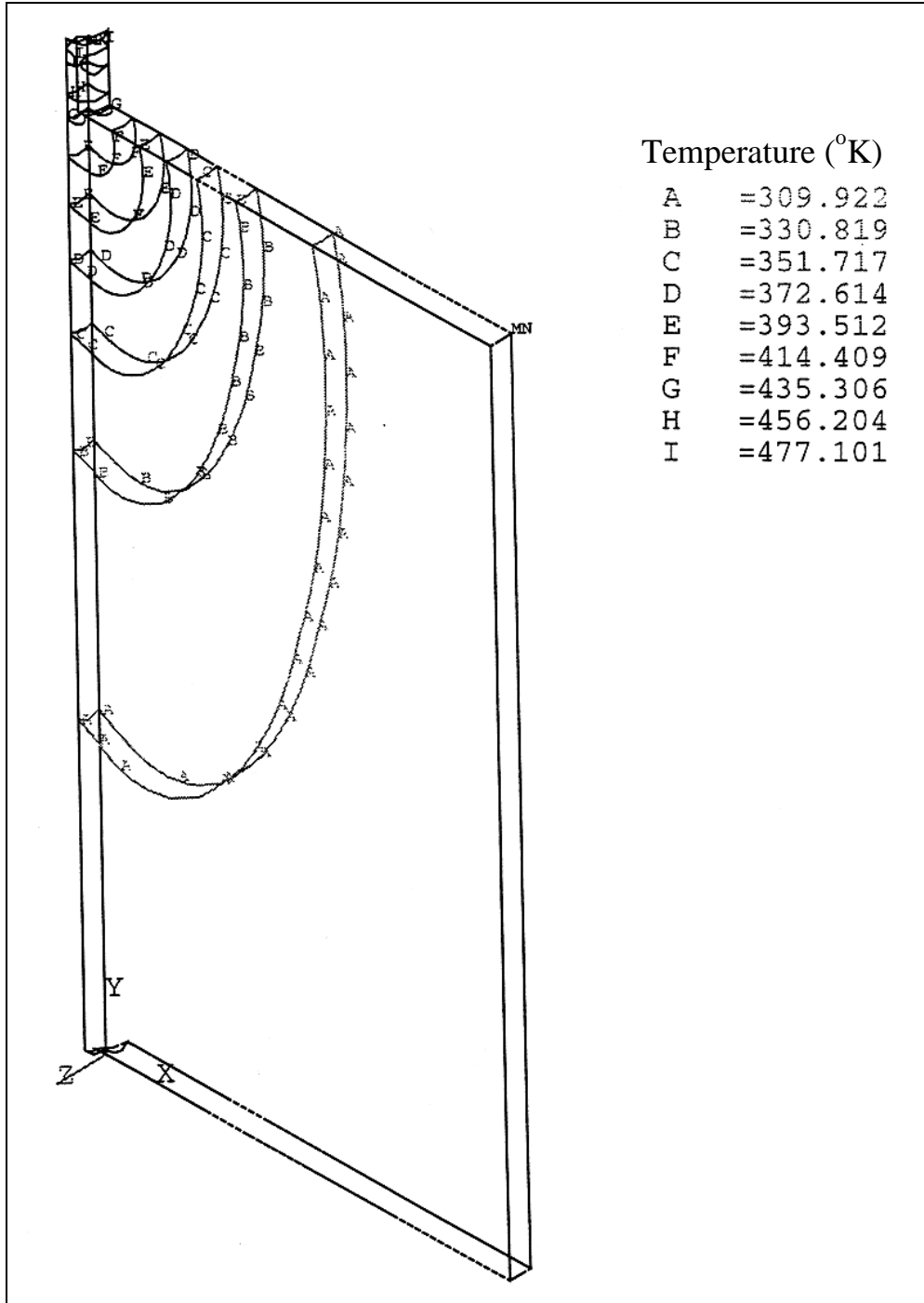
(c)Time = 4800 seconds

Figure 3.6 (continued): Temperature profiles for ANSYS fixed coordinate system thermal model calculations as a function of time after weld initiation



(d)Time = 5600 seconds

Figure 3.6 (continued): Temperature profiles for ANSYS fixed coordinate system thermal model calculations as a function of time after weld initiation



(e)Time = 6300 seconds

Figure 3.6 (continued): Temperature profiles for ANSYS fixed coordinate system thermal model calculations as a function of time after weld initiation

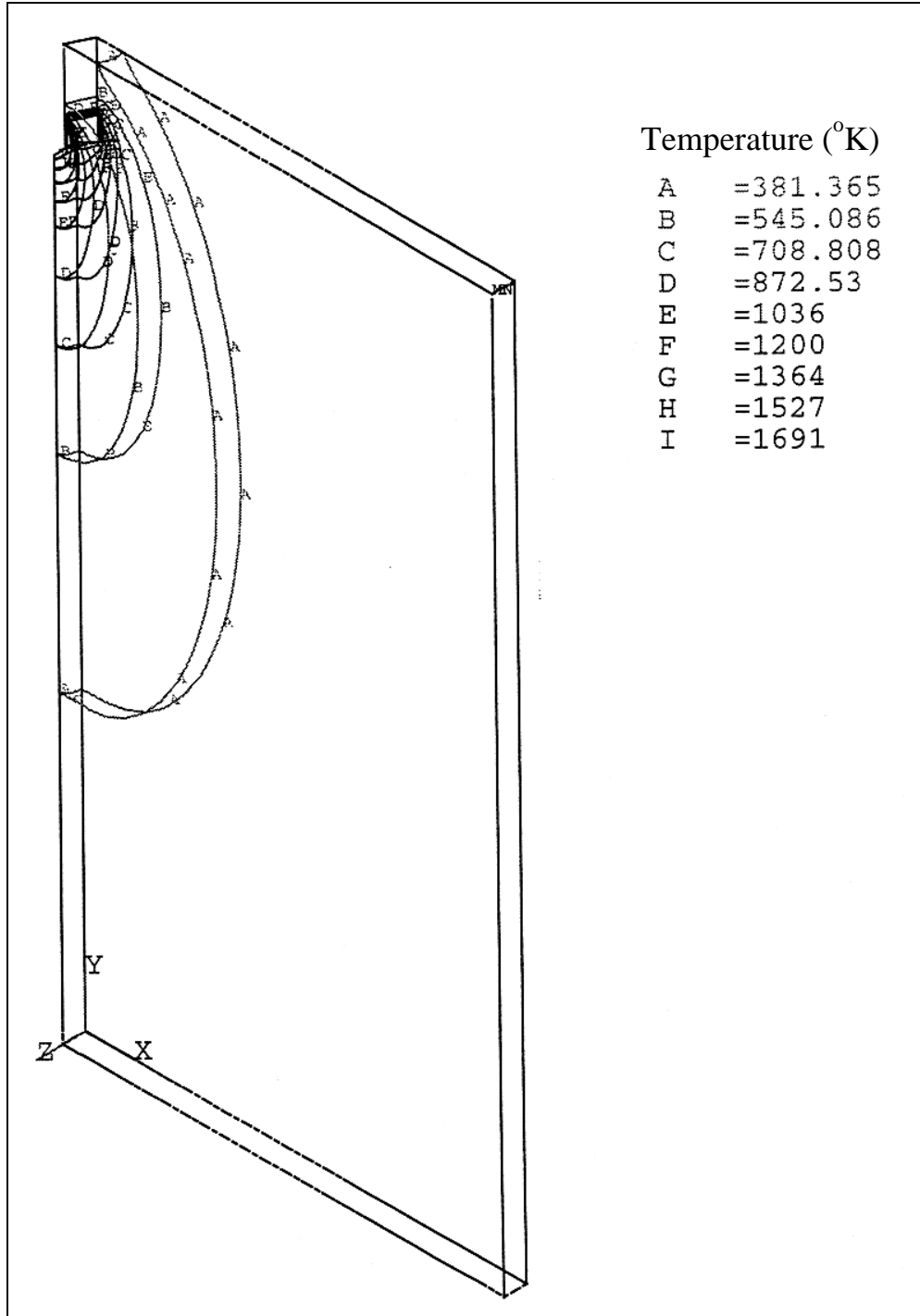
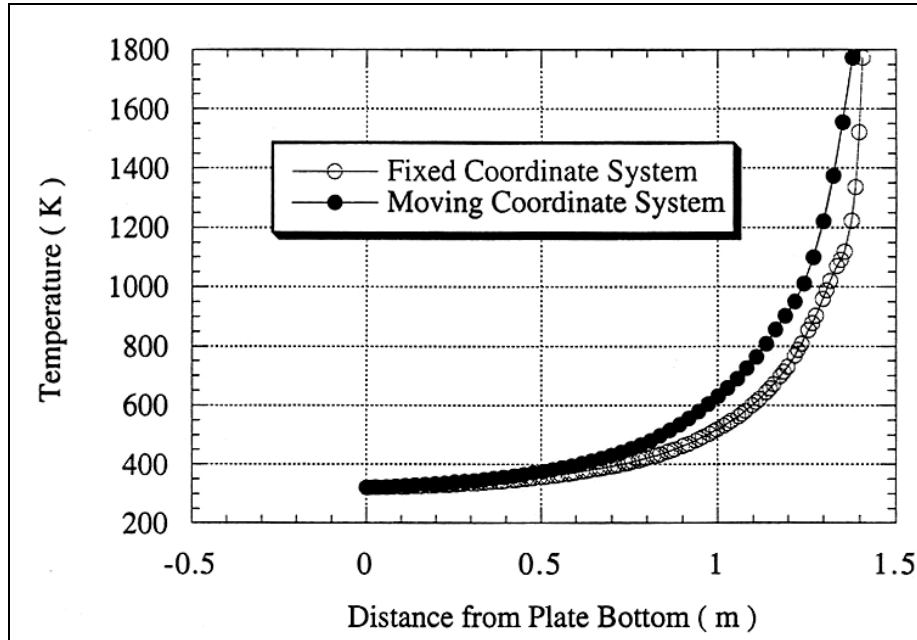


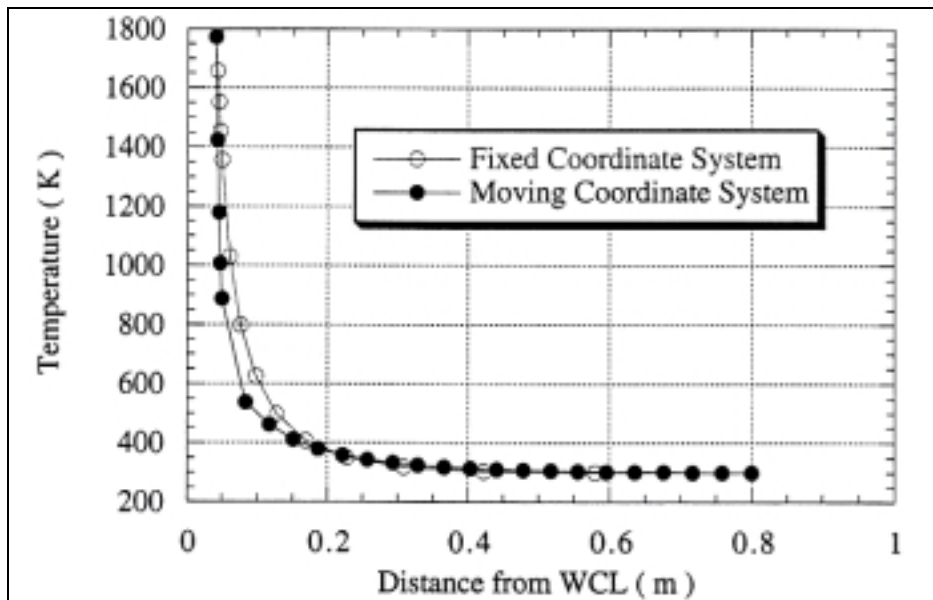
Figure 3.7: Temperature profile for ANSYS moving coordinate system thermal model calculation

In order to compare the results of the two calculational systems in detail, the temperature results for the nodes along the WCL and perpendicular to the welding direction for the two calculation systems are plotted in Figure 3.8. Figure 3.8a compares the temperature results of nodes along the WCL for the fixed coordinate system and the moving coordinate system. Figure 3.8b

compares the temperature results of nodes perpendicular to the welding direction on the middle plane as a function of distance from WCL for the fixed coordinate system and the moving coordinate system. It can be seen that the results are consistent. The slight difference between them may be caused by a combination of the different mesh sizes used for the two models and the increased accuracy of the moving coordinate system over fixed coordinate system.^[64,65]



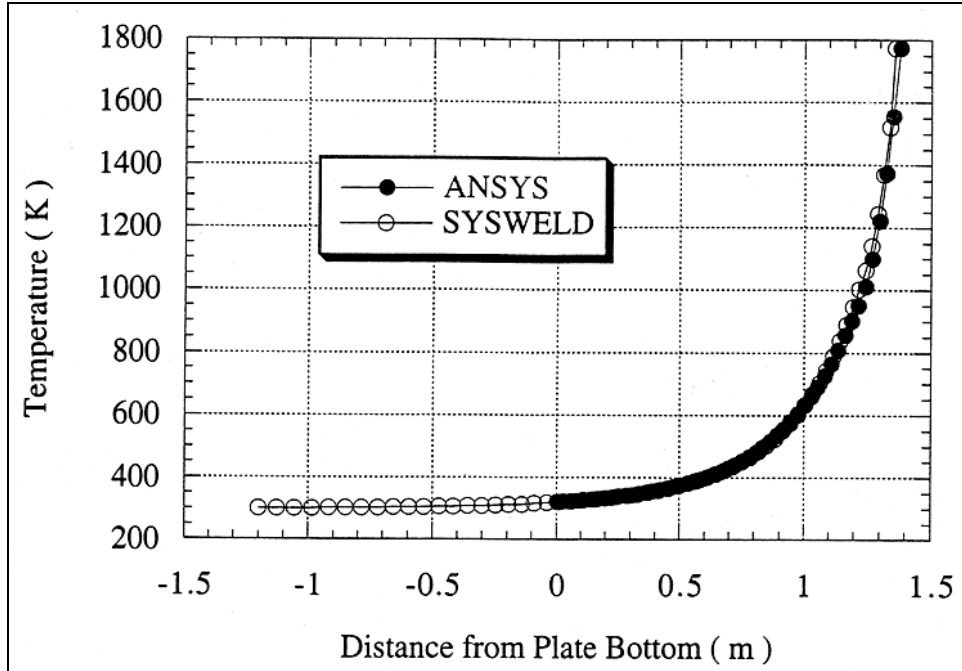
(a) Temperature as a function of distance from plate bottom along WCL on mid-plane



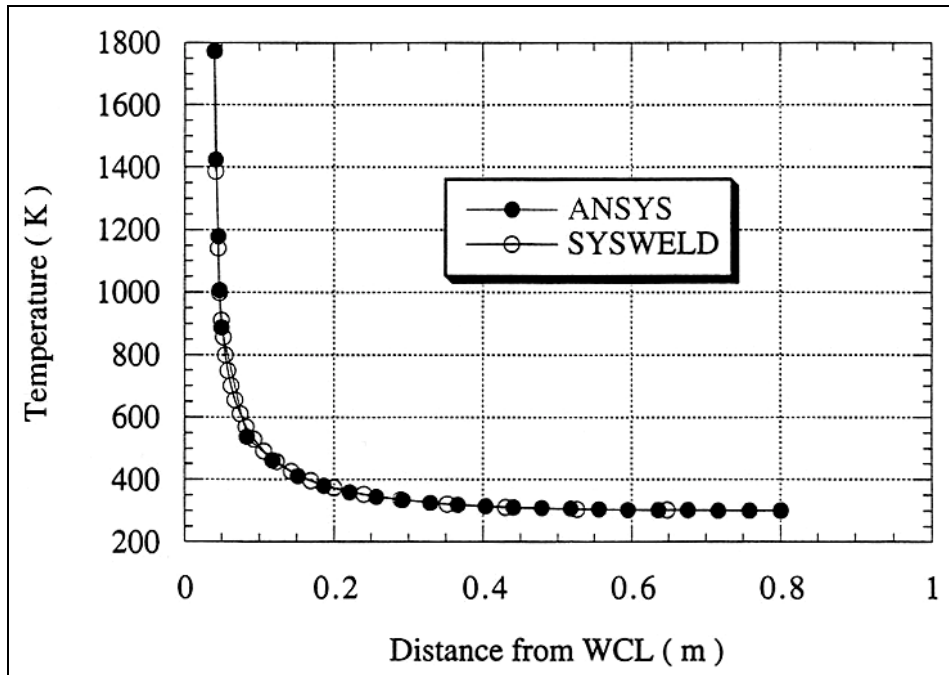
(b) Temperature as a function of distance from WCL on mid-plane

Figure 3.8: Comparison of thermal history predictions between ANSYS 3Dmoving and fixed coordinate system models

Temperature comparisons between the ANSYS and SYSWELD thermal moving coordinate models are given in Figure 3.9. Figure 3.9a illustrates the temperature as a function of distance from the plate bottom (synonymous with time after welding for the moving coordinate system) along the WCL on the middle plane for ANSYS and SYSWELD. It should be noted that the model bottom is at -1.2 m along the y coordinate direction for the SYSWELD moving coordinate model resulting in an effective plate length of twice the actual plate length. The ANSYS fixed coordinate system models the actual plate length. The extra plate length was added to all SYSWELD models used for residual stress calculations because the additional plate length in the moving coordinate system increased the cool-down time, which was needed to assure the weld reached ambient temperature prior to assessment of the post-weld residual stress. The plot of temperature as a function of distance from WCL perpendicular to the welding direction on the middle plane for the ANSYS and SYSWELD programs, Figure 3.9b, showed that the two programs provided similar results. However, SYSWELD required seventy-five percent less computation time than ANSYS.



(a) Temperature as a function of distance from plate bottom along WCL on mid-plane



(b) Temperature as a function of distance from WCL on mid-plane

Figure 3.9: Comparison of thermal history predictions between ANSYS and SYSWELD 3D moving coordinate system models

The close agreement of thermal history results between the moving and fixed coordinate systems provided justification to the authors for using a moving coordinate system to model ESW. The agreement between the ANSYS and SYSWELD thermal results provided justification to the authors for using the SYSWELD code; consequently, all subsequently reported modeling results were obtained using the SYSWELD commercial finite element code.

3.5 RESIDUAL STRESS RESULTS FOR 3D MODELS WITH MOVING COORDINATE SYSTEMS

Several different ES weldments were modeled using SYSWELD. The A36 plates used to fabricate the girder were 1.5 m wide (the welding direction) and 6 m long. However, the model used an effective plate length to minimize calculation time. The plate length needed to be modeled was assessed using a residual stress history perturbation assessment technique.^[63] An effective plate length conduction heat transfer value was assigned to the plate length termination boundary, and plate length was decreased from 6 m until this reduction in length affected the resultant residual stress. A plate length of 0.8 m was modeled in this study. It was assumed that 1.5 m long water-cooled copper shoes were used during welding and that these shoes stayed on for the complete weld cycle as well as during cool-down.

All of the study models nominally represented the West Linn Bridge ES weldment plate thicknesses and expected welding parameters. The plate thickness of 8 cm (3.15 in.) used in the model was slightly less than the thickness of 9 cm (3.5 in.) exhibited by the cores. The other modeled weldments were perturbations on this base model and covered expected welding parameter changes in plate thickness and welding speed. The plate thickness changes covered the range of thicknesses found on the West Linn Bridge, namely 2.5 in. to 3.5 in. The base 8 cm thick model was modeled using the nominal geometry of the West Linn Bridge-specific weld fusion zone determined experimentally (see Chapter 2) and a reasonable, best-guess welding speed; the results of this model are presented below in detail. Next, the results from a series of weld predictions using different weldment parameters are presented. Table 3.1 presents the weldment parameters used with the various models.

Table 3.1: Parameters for three dimension numerical analysis of ESW process

	Plate Thickness (cm)	Plate Height (m)	Plate Length (m)	Welding Speed (cm/s)
SYSWELD model 1	9	2.76	6.12	0.03
SYSWELD model 2	8	2.76	6.12	0.03
SYSWELD model 3	8	2.76	6.12	0.02
SYSWELD model 4	8	2.76	6.12	0.04
SYSWELD Model 5	10	2.76	6.12	0.03
SYSWELD Model 6	6	2.76	6.12	0.03

Thermal history predictions were run for all models using the thermal model criteria previously discussed in this chapter. Only symmetry boundary conditions were used during the residual stress analysis. The residual stress was modeled under self-restrain only. No external restraints

were applied in the analysis. To prevent rigid body motion during the finite element analysis, only two nodes on the domain edge were fully restrained. This suggests that the welded plate is not restrained but is pivoted around these restrained nodes and the restraint free condition is realized.

Planes $A_{1n}B_{1n}B_{11}A_{11}$ and $A_{1m}B_{1m}B_{11}A_{11}$ were constrained along the x coordinate direction; plane $B_{2n}D_{21}C_{21}B_{21}$ was constrained along the y coordinate direction. (see Figures 3.4b and c for direction and plane position).

The simplifying assumptions that were used in the mechanical model development were:

1. The non-linear thermoelastic-viscoplastic model was reduced to a linear thermoelastic model. A linear elastic-plastic stress-strain relation was assumed. The elastic and plastic regions were defined by elastic moduli and plastic moduli, with the transition occurring at the yield stress.
2. Potential defect or crack formation was ignored.
3. Creep and hardening were ignored. Simplified yield laws were used. Von-Mises yield criterion and associated flow rule with kinematic hardening were assumed to consider the Bauschinger effect. As in most welding problems, creep effects were neglected on the basis that time spent at high temperature is short for a weld.
4. The phase transformation expansion effect was considered to be similar during heating and cooling because of lack of available thermal expansion coefficient values. Plastic strain due to the change in volume during allotropic phase transformation is neglected in this study. A more representative treatment would involve incorporating the transformation plasticity effect for weld metal as well as different HAZ regions.
5. The same material properties were used for base metal, weld metal and HAZ. This would be expected to change the magnitude of the resulting residual stresses, but not the overall residual stress distribution characteristics.

The copper shoe's effective heat transfer coefficient was set at 130 J/(msK) while the plate surface effective heat transfer coefficient was set at 84 J/(msK). The material yield strength, thermal conductivity, enthalpy, Poisson's ratio, elastic and plastic modulus, and coefficient of thermal expansion were allowed to vary as functions of temperature.^[63] The temperature dependent material thermal properties used for this modeling study are shown in Figures 3.10 through 3.13.

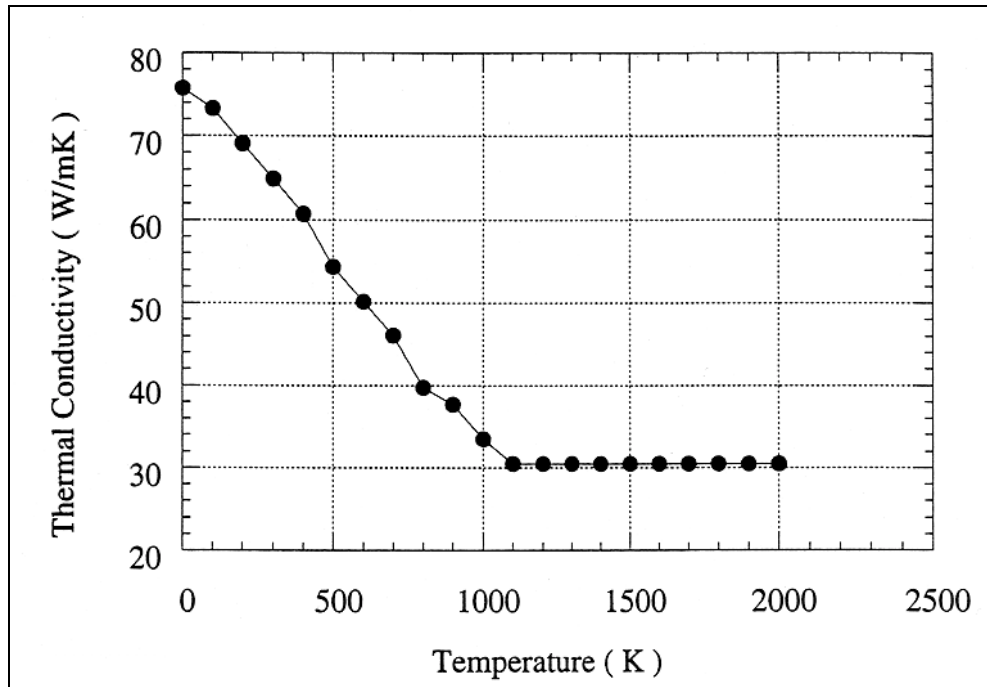


Figure 3.10: Temperature dependent thermal conductivity

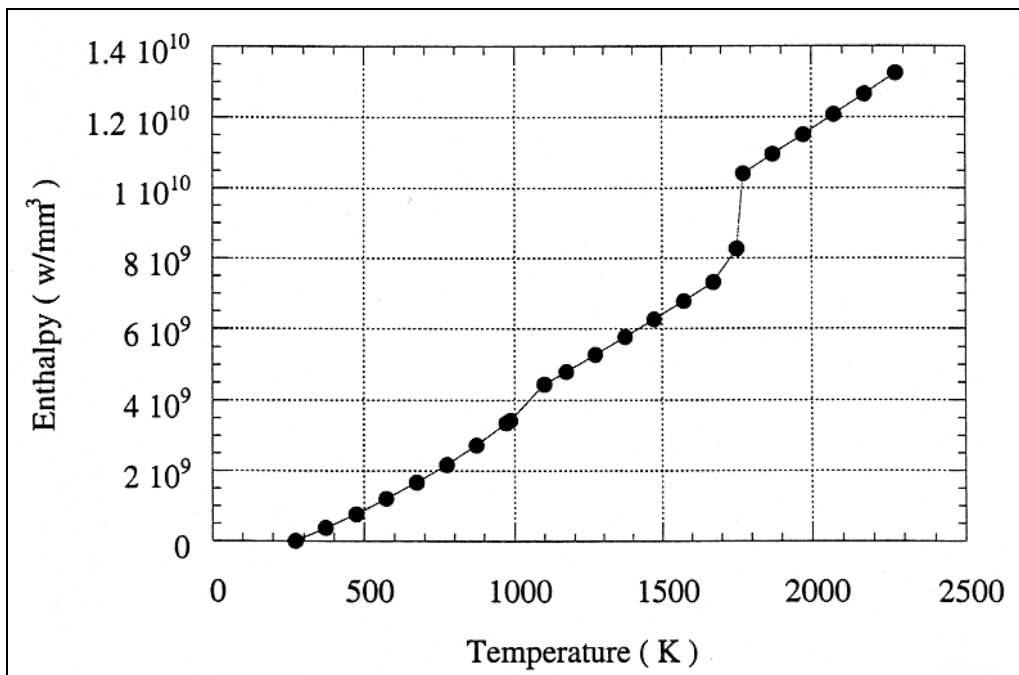
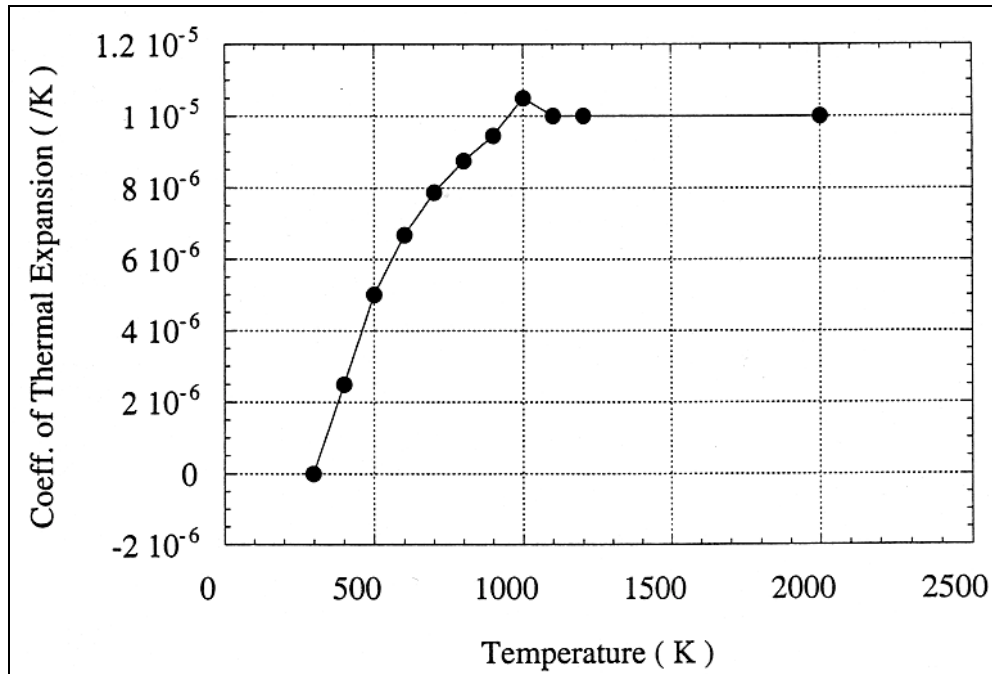
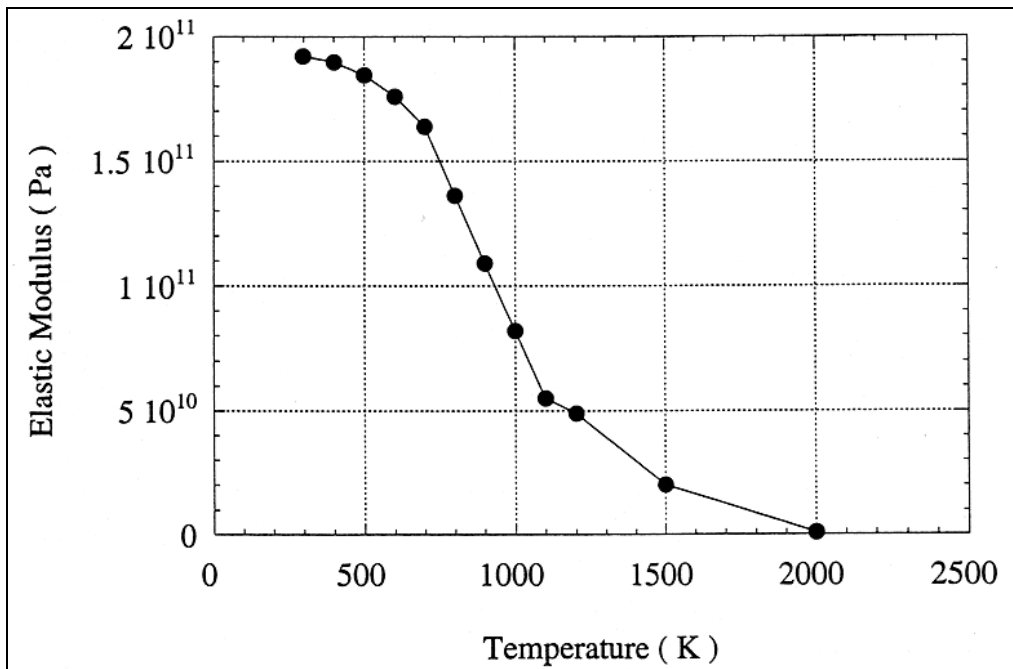


Figure 3.11: Temperature dependent enthalpy

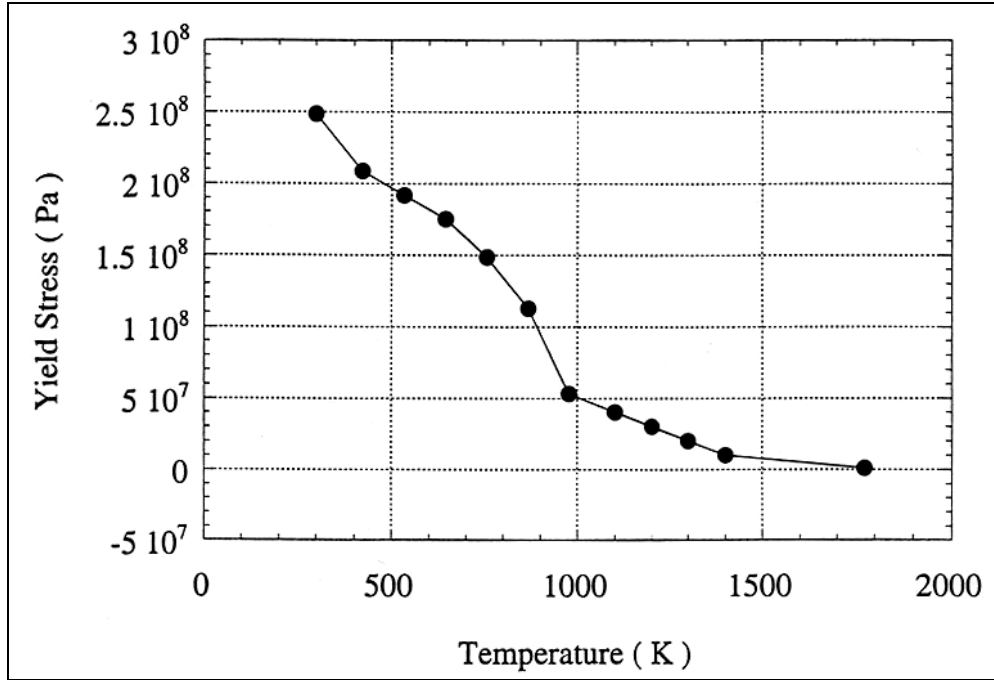


(a) Coefficient of thermal expansion

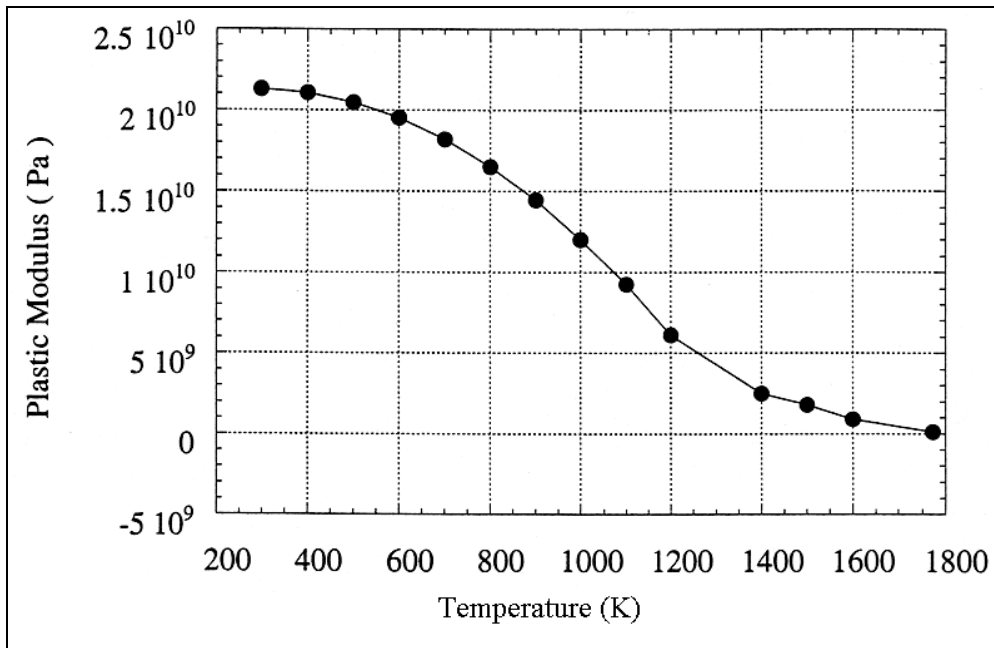


(b) Elastic modulus

Figure 3.12: Temperature dependent mechanical properties



(c) Yield stress



(d) Plastic modulus

Figure 3.12 (continued): Temperature dependent mechanical properties

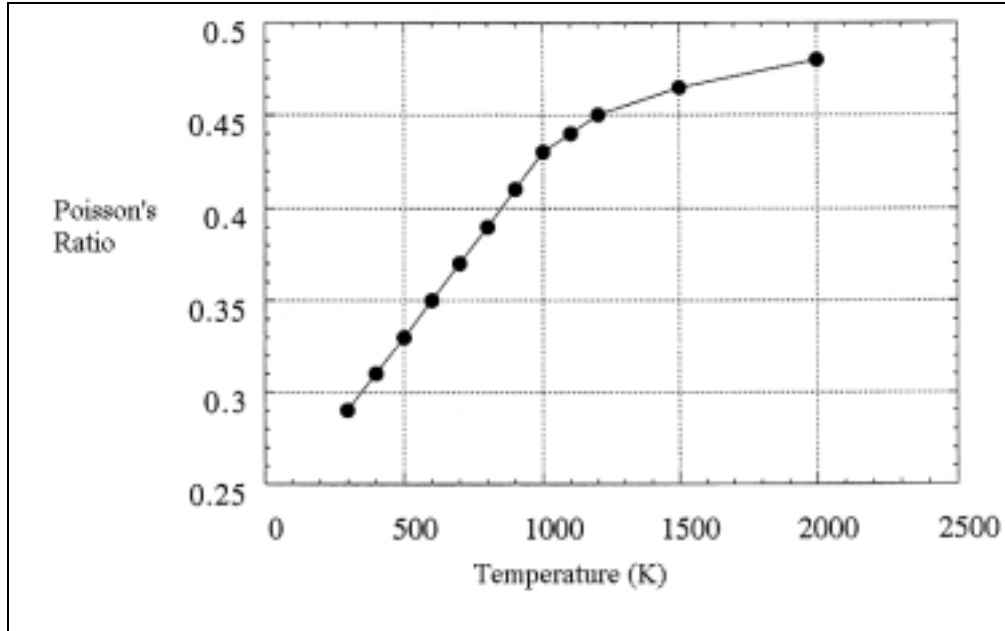
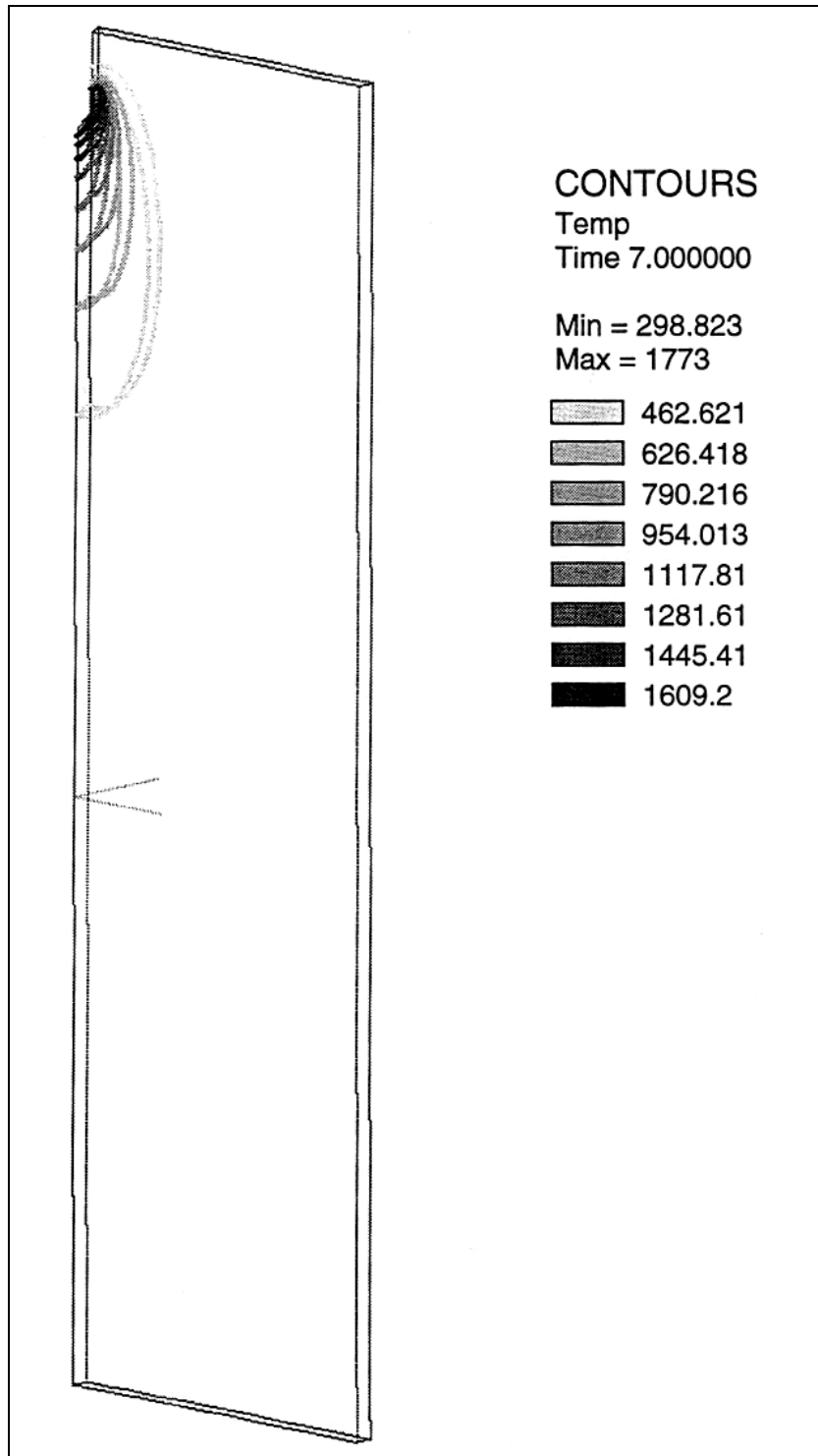


Figure 3.13: Temperature dependent Poisson's ratio

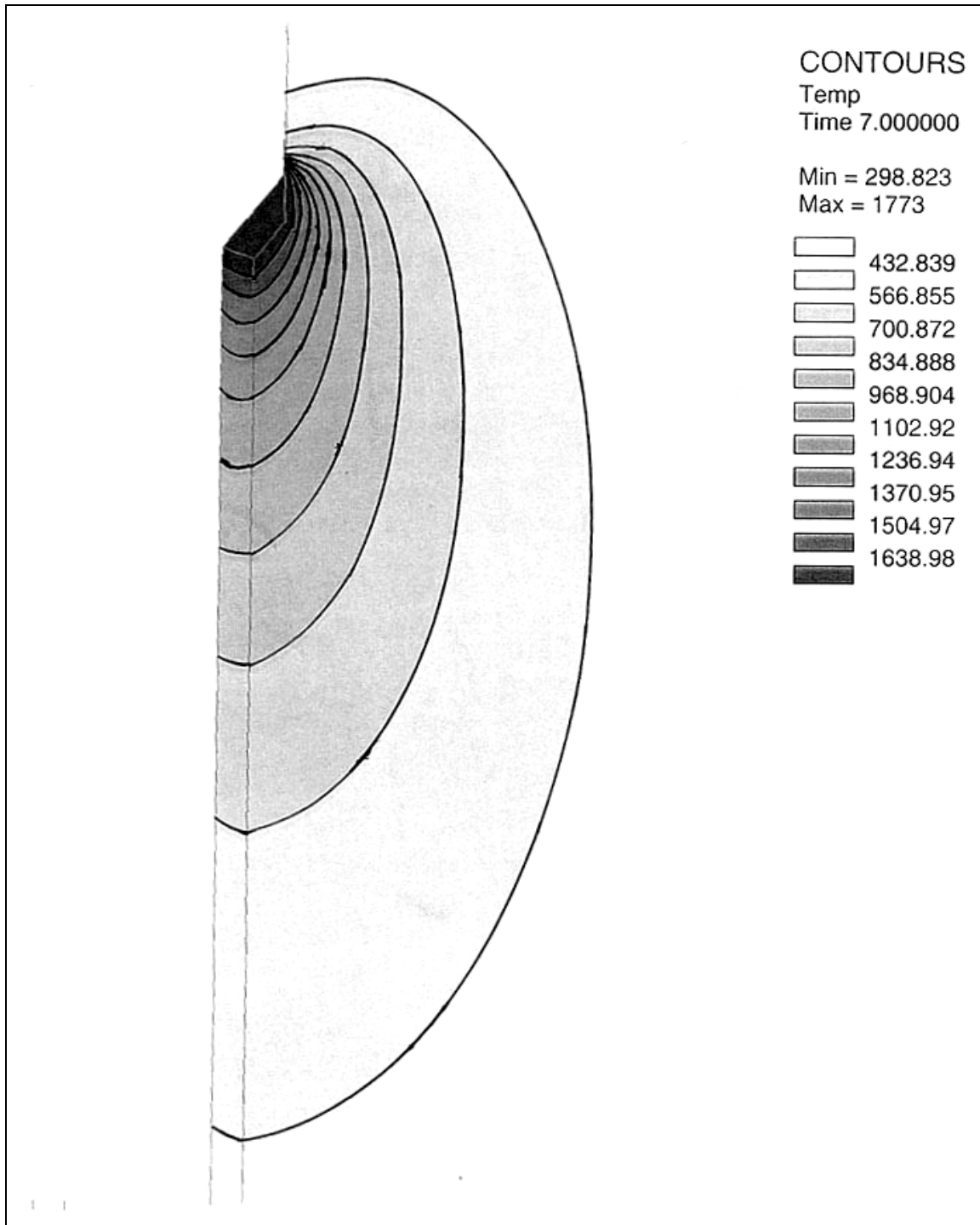
3.6 MODELING RESULTS

The 3D thermal history model results for the 3.15 in. (8 cm) thick plate in and near the HAZ/fusion region are shown in Figure 3.14. They illustrate the steep thermal gradients present in all directions from the fusion zone boundary, as well as the pre-heating that occurs in front of the fusion zone/slag bath in ESW. This is because of the massive through-thickness molten zone present in ESW in comparison to arc-welding processes. The temperature profile in Figure 3.14a reveals that the bottom part of the welded plate is at room temperature when the heat source moves near the top of the welded plate. Thus, the plate length is long enough in the models for mechanical analysis. Note that the vertical axis is actually a time axis for this fixed coordinate problem, with time after welding increasing with distance from the fusion zone.



(a) Over-all thermal contours

Figure 3.14: Temperature profiles for SYSWELD 3D moving coordinate system thermal model calculation



(b) Fusion zone thermal contours

Figure 3.14 (continued): Temperature profiles for SYSWELD 3D moving coordinate system thermal model calculation

The Von Mises stress distribution profile with the heat source close to the top of the plate is shown in Figure 3.15. It indicates that the weld-induced stress field is contained within the modeled segment of the plates.

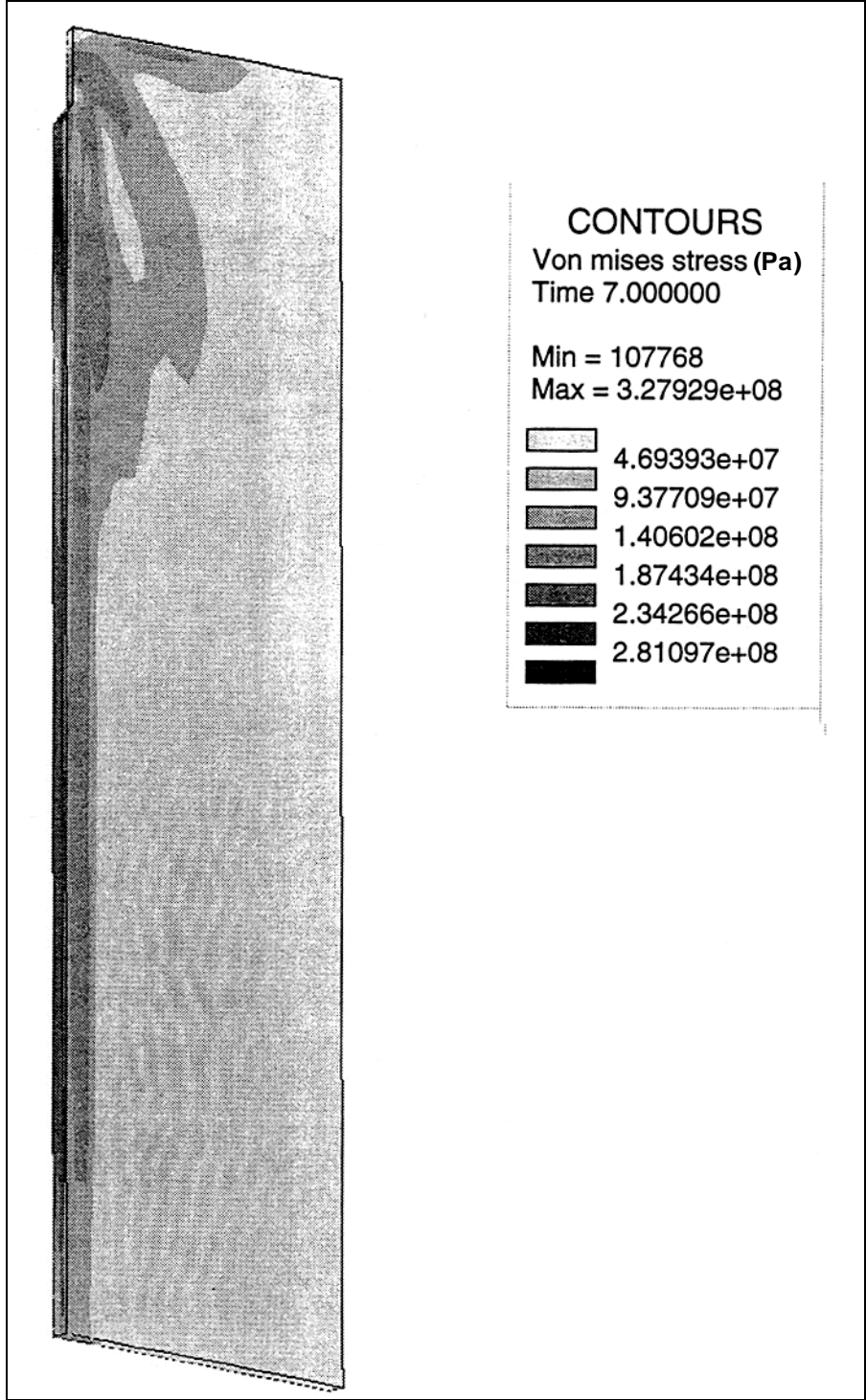


Figure 3.15: Von Mises stress profile for SYSWELD 3D moving coordinate system thermal mechanical model calculation

The residual stress values that were analyzed are the residual stress results at the bottom part of the welded plate determined by the mechanical analysis based on the thermal analysis results. The Von Mises distribution profile in Figure 3.15 reveals that the highest stress is concentrated around the heat source during ESW process. The residual stress in the fusion zone is very complicated. The x, y and z coordinate directions correspond to directions perpendicular to the welding direction, parallel to the welding direction and transverse to the plate thickness direction, respectively. The most important stresses, from a structural integrity standpoint, are those perpendicular and parallel to the welding direction.

The residual stress results from the 8 cm thick 3D moving coordinate model for the stress components perpendicular and parallel to the welding direction are shown in Figures 3.16 through 3.17.^[72] Note that the WCL is at X = 0, while the fusion line is at X = 4 cm. Figure 3.16 presents the residual stress perpendicular to the welding direction as a function of distance from WCL for mid-plane and surface stresses. The graph shows considerable stress variation in the HAZ and weld fusion zone region accompanied with strong stress gradients. Stress farther from the HAZ region continues to exhibit strong gradient changes until finally leveling out approximately 0.8 m from the WCL. Note that both mid-plane and surface stress are compressive, with the surface stresses near the WCL being more compressive than the mid-plane stresses.

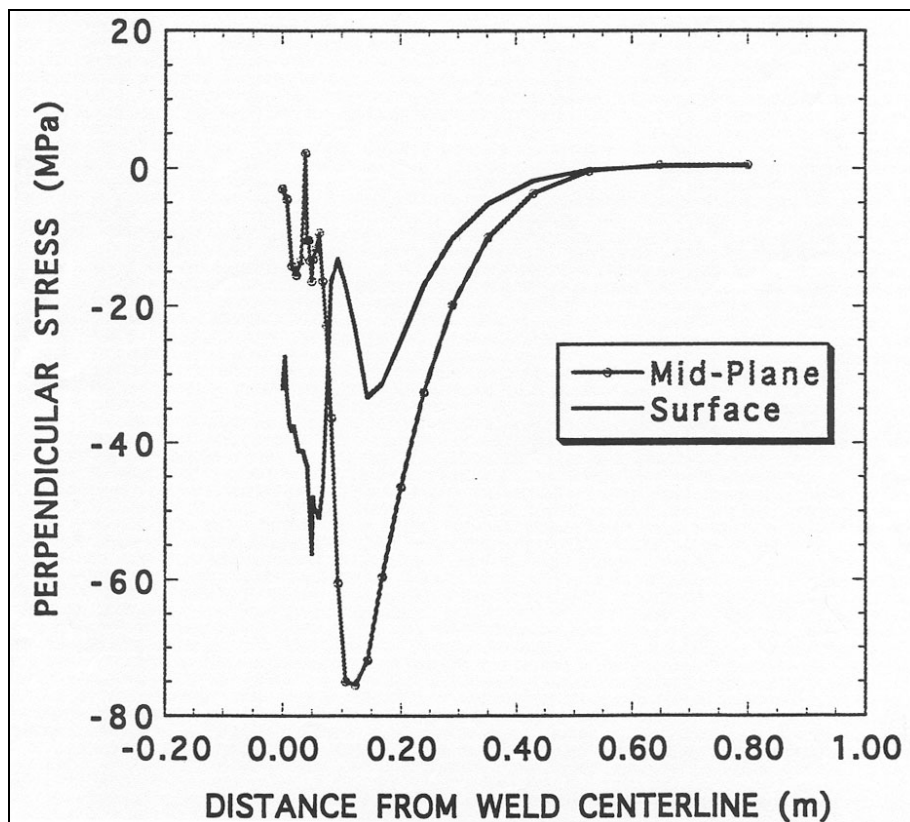
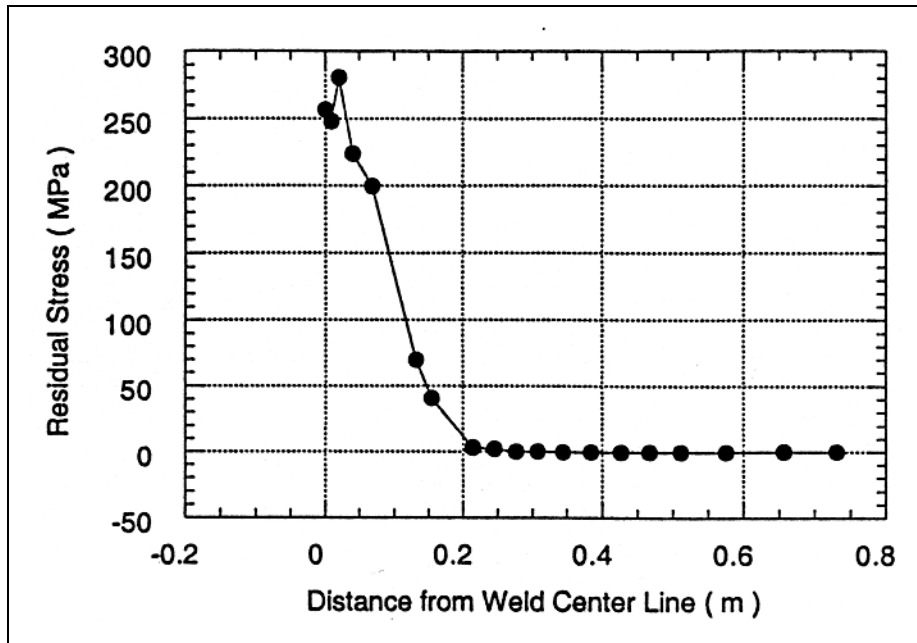
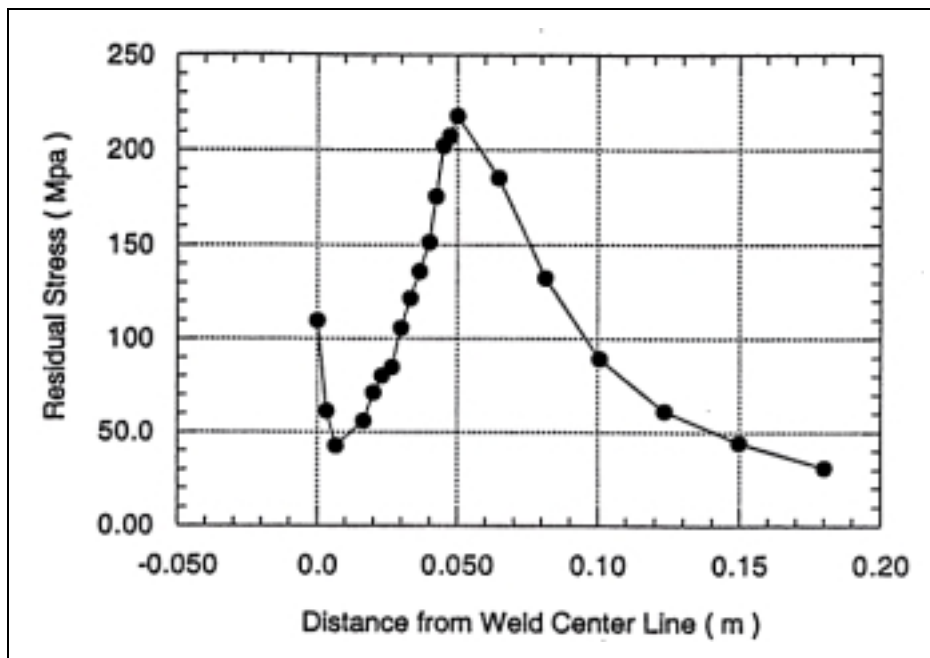


Figure 3.16: Mid-plane and surface residual stress perpendicular to WCL for SYSWELD 3D model



(a) Mid-plane



(b) Cross-section

Figure 3.17: ANSYS 2D fixed coordinate system model residual stress results

The mid-plane residual stress perpendicular to the WCL begins at the WCL with a compressive stress near 0 MPa, drops to -15 MPa, then increases to 5 MPa around the boundary of the fusion zone and the HAZ and then drops to -75 MPa at the distance from the WCL around 0.1 m. After that the stress goes back to zero with increasing distance from WCL. The surface stress results reveal that the WCL perpendicular stress at the plate surface is also compressive. The stress begins near -25 Mpa, decreases to its lowest compressive stress of -55 MPa, and then it increases to zero with increasing distance from the WCL, with the stress going up and down between the lowest compressive stress and zero stress.

The mid-plane residual stress distributions perpendicular to the WCL predicted using two different 2D models are shown in Figure 3.17^[72]. One 2D model was a mid-plane model while the second 2D model was a cross-sectional model, as illustrated in Figure 3.18. Both models predict only tensile stresses as a function of distance from WCL, in dramatic contrast to the compressive stress predictions from the 3D model, Figure 3.16. Also, the mid-plane model predicts tensile stress levels approaching 1.75 times the materials yield stress at the WCL. The cross-sectional model predicts tensile stresses with a magnitude of half the yield stress at the WCL, which is considerably less than the prediction of the mid-plane model, but still dramatically different from the 3D model prediction results. The 2D model results are in direct contradiction with the 3D results and are also in conflict with each other. Thus, the results from this study indicate that the use of simplified 2D models should be avoided in analyzing ESW.

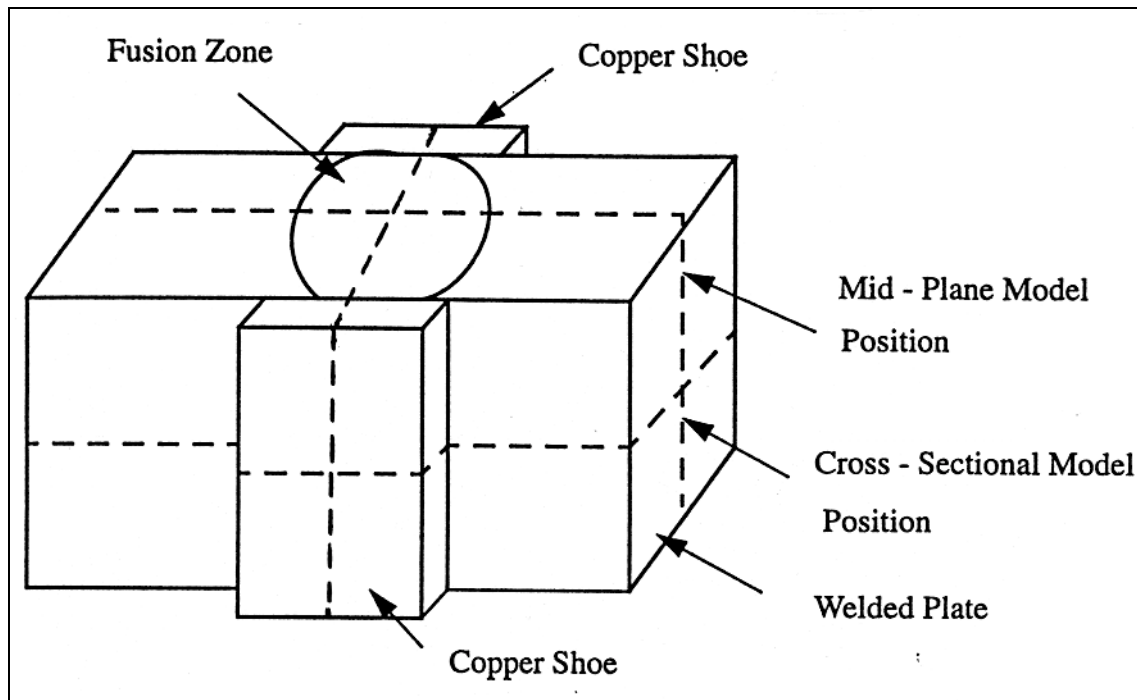


Figure 3.18: ANSYS 2D fixed coordinate system model set-up

The 3D residual stress distributions parallel to the direction of welding as a function of distance from WCL for mid-plane and surface stresses are shown in Figure 3.19. These stress plots also exhibit considerable stress variation in the HAZ and weld fusion zone region as well as strong stress gradients, until the stress levels out at essentially 0.8 m from WCL. Here, however, the parallel stresses exhibit tensile stress in the HAZ and fusion zone region. The stresses then become compressive with increasing distance from the WCL and then increase again to zero stress with increasing distance from WCL. The maximum tensile stress in the fusion zone is approximately a quarter of the yield strength, with the mid-plane value being greater than the surface value.

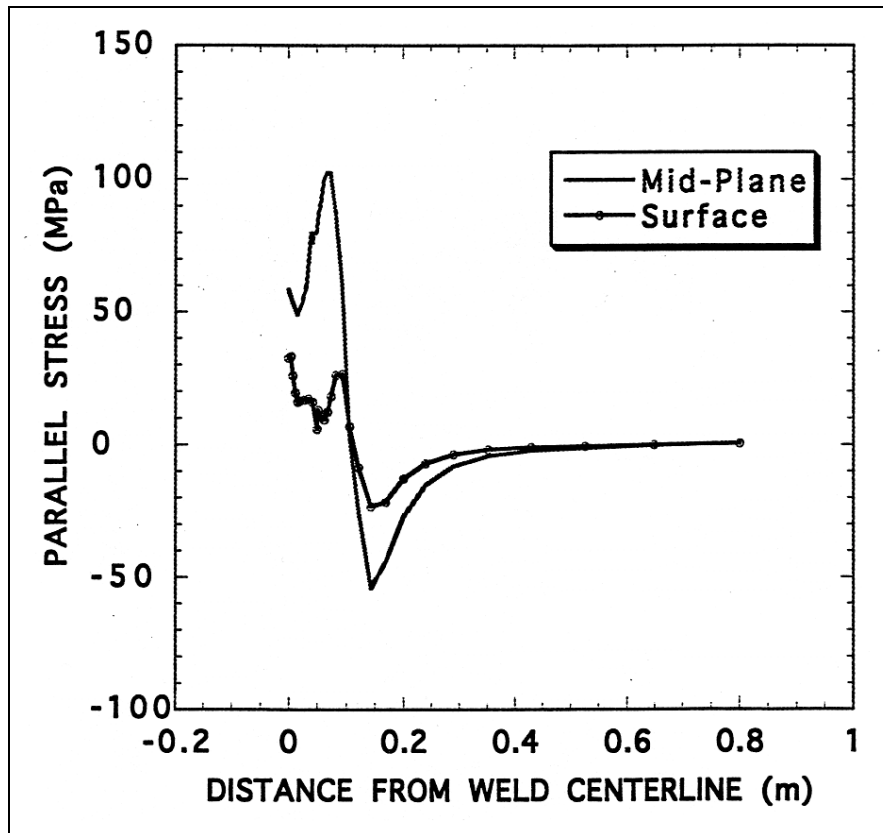


Figure 3.19: SYSWELD 3D model predicted residual stress parallel to weld

The mid-plane parallel stress results reveal that the parallel stress begins with a tensile stress that is slightly less than a quarter of the yield stress, drops to a low tensile stress around 50 MPa, increases to the highest tensile stress of 110 MPa (approximately half the yield stress) in the region of the HAZ, drops from the highest tensile stress to a low compressive stress of -55 MPa, and then approaches zero with increasing distance from WCL. The surface parallel stress begins at the WCL with a low tensile stress of around 35 MPa, decreases close to zero stress, increases to 30 MPa, decreases again to a low compressive stress of -25 MPa and then increases to zero with increasing distance from the WCL.

The perpendicular and parallel residual stresses at the WCL as a function of plate thickness are shown in Figure 3.20. Both stress sets are found to first decrease in magnitude with increasing distance from the mid-plane and then increase as the plate surface is approached. The stress magnitudes at the plate surface are still less than that found at the mid-plane, WCL position. Note that the WCL residual stress perpendicular to the welding direction remains compressive from mid-plane to plate surface while the parallel stress remains tensile.

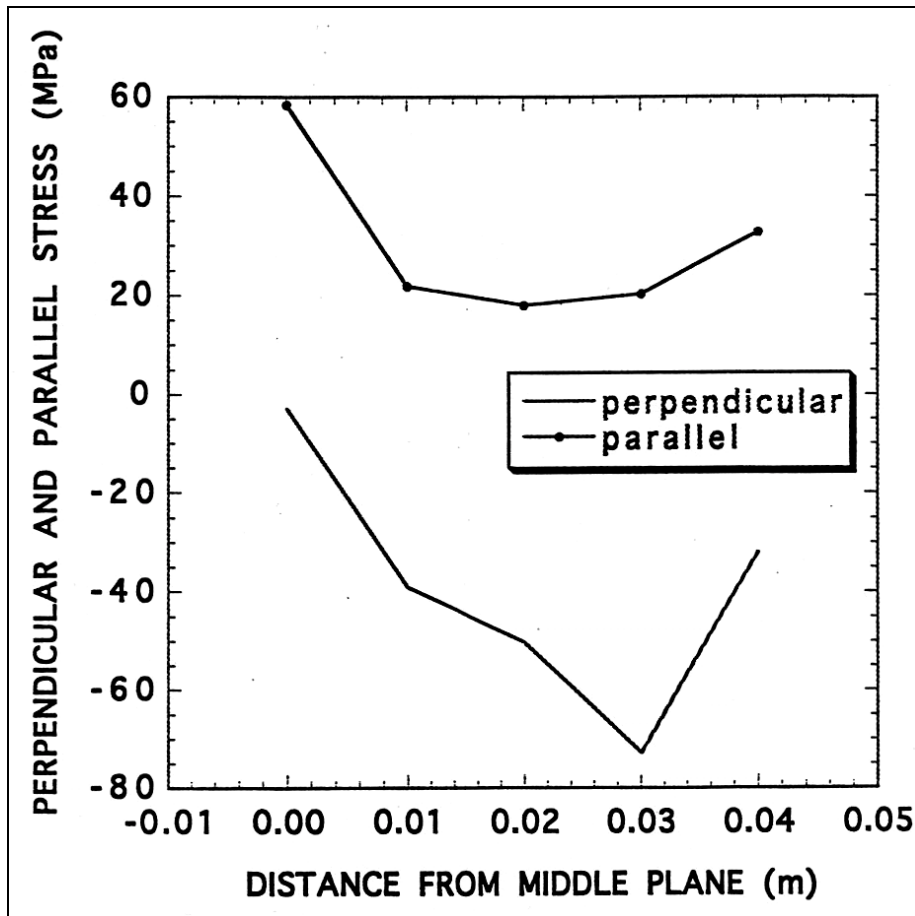


Figure 3.20: SYSWELD 3D model predicted through-thickness residual stress at WCL for 8 cm thick weld

The model results presented above are an in-depth look at a specific model close to what is expected on the West Linn Bridge in the areas where the cores were removed. The model assessments given below present predictions of the effect of parameter changes on expected residual stresses.

The following figures illustrate the effect of welding parameter changes on the surface residual stress perpendicular to the welding direction. This stress component was chosen because it is the most important one from a crack propagation aspect. Welding speed was allowed to vary

between 0.02cm/s and 0.04cm/s, see Figure 3.21. This range was felt to be reasonable for standard ESW practice for the thickness of steel plate on the West Linn Bridge^[1]. The modeling results predict that the HAZ/fusion zone region exhibits increasing stress level with decreasing speed. This trend then reverses with increasing distance from WCL and reverses again until the stress reaches zero.

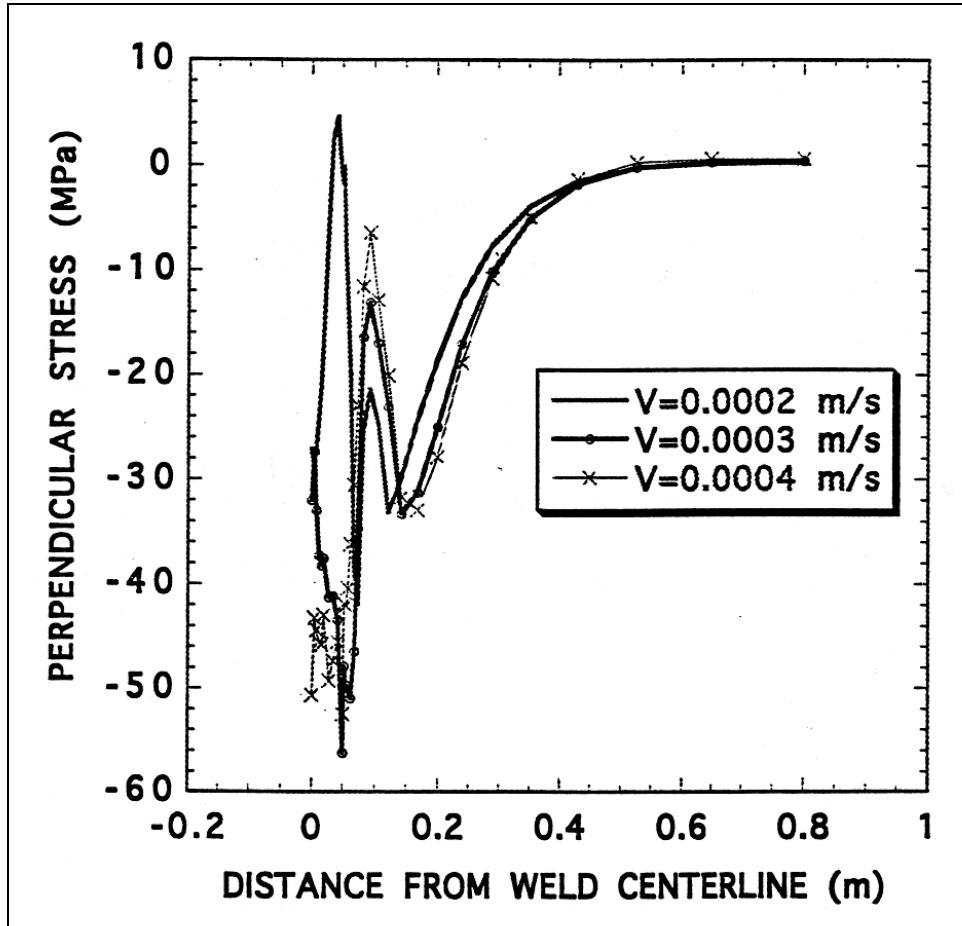


Figure 3.21: SYSWELD 3D model predicted welding speed effect on surface residual stress perpendicular to welding direction

An assessment of the effect of changing welding speed on the maximum level of residual surface stress perpendicular to the welding direction near the HAZ/fusion zone is shown in Figure 3.22. The residual stress values plotted in this figure come from the maximum stress found in the first stress oscillation near the WCL in Figure 3.21. It can be seen that the maximum residual stress value increases with decreasing welding speed and goes from compressive to tensile near 0.02cm/s. Thus, one should set a lower welding speed limit to keep surface residual stresses compressive.

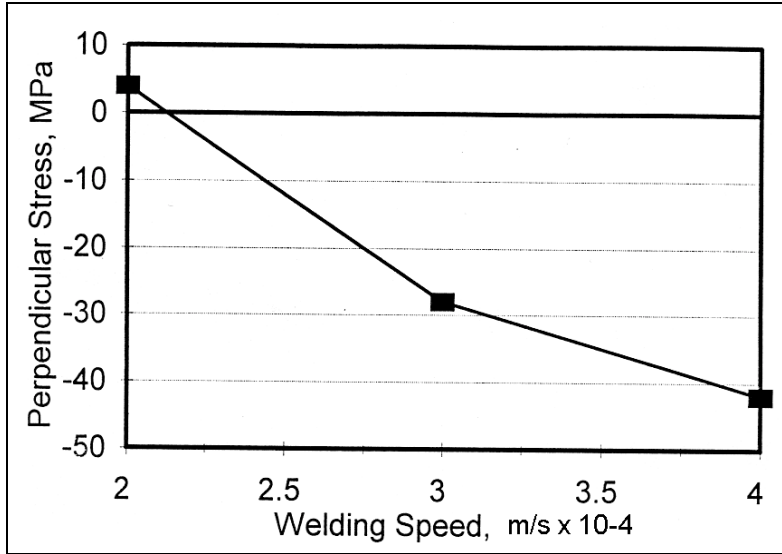


Figure 3.22: SYSWELD 3D model predicted welding speed effect on maximum residual stress perpendicular to welding direction in the HAZ/fusion zone

The effect of welding speed on heat input for this modeling analysis is shown in Figure 3.23. Note that heat input increases with increasing welding speed. This is because the model assumes that the fusion zone size remains constant for all welding conditions, as this was the only empirical information about welding parameters that was available. Higher heat input, in general, is expected to decrease residual stress, as it results in spreading the resultant weld-induced strain over a wider region and decreases resultant cooling rates. Model results agree with this expected trend. Note that heat input would be expected to decrease with increasing welding speed if current and voltage were held constant.

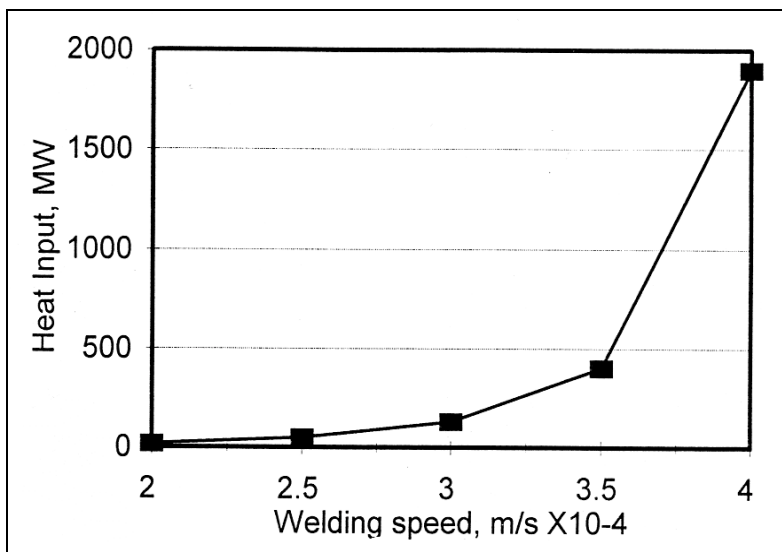


Figure 3.23: SYSWELD 3D model predicted welding speed effect on heat input

The effect of plate thickness change on surface residual stress perpendicular to the welding direction as a function of distance from the WCL is shown in Figure 3.24. The near HAZ/fusion zone residual stress was found to increase with decreasing plate thickness. Change in plate thickness was found to have little effect on residual stress with increasing distance from the WCL.

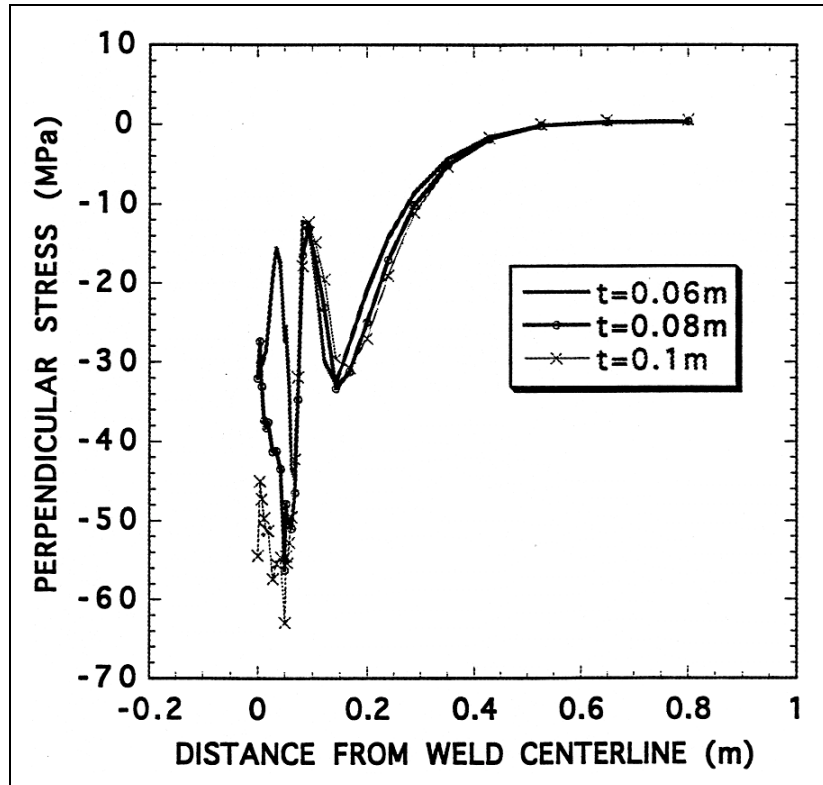


Figure 3.24: SYSWELD 3D model predicted plate thickness effect on surface residual stress perpendicular to welding direction

The effect of plate thickness on the maximum magnitude of the perpendicular residual stress near the HAZ/fusion zone is illustrated in Figure 3.25. It is predicted that maximum residual stress values increase with decreasing plate thickness but remain compressive for all thicknesses assessed. Extrapolation of the assessed results indicate that one could weld plates down to 4 cm in thickness using a welding speed of 0.03 cm/s and a mid-plane fusion zone width of 8 cm before the surface residual stress perpendicular to the welding direction would be expected to become tensile.

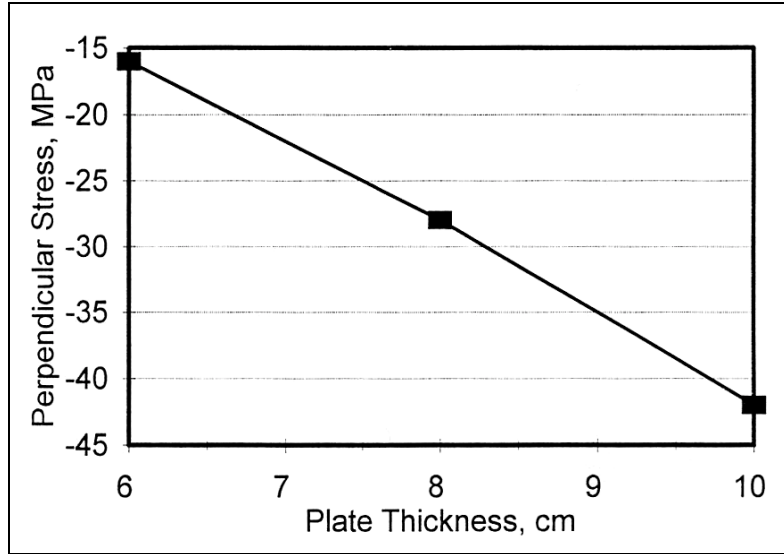


Figure 3.25: SYSWELD 3D model predicted plate thickness effect on maximum residual stress perpendicular to welding direction in the HAZ/fusion zone

3.7 CONCLUSIONS

A comparison between 2D and 3D modeling results indicate that 3D modeling must be used for ESW.

Use of the 3D moving coordinate (Eulerian) system for weld analysis allowed use of multiple 3D analyses, thus permitting weld parameter perturbation effects on resultant residual stress fields. The large range of parametric variations performed would not have been possible with conventional fixed coordinate (Lagrangian) analysis.

Residual stresses for ESW of thick plates exhibiting an 8 cm fusion zone in the HAZ/fusion zone are much less than the yield strength of the steel, and, in fact, are compressive perpendicular to the welding direction. The stress field distribution for ESW was found to be complex and extend a distance of up to ten times the fusion zone width.

4.0 EXPERIMENTAL RESIDUAL STRESS ASSESSMENT

4.1 INTRODUCTION

The objective of the work reported in this Chapter was to develop an experimental data base that could be used to assist in quantifying the residual stress/strain field in ES butt welded steel plates. Two types of residual stress measurements were made. One set involved physical removal of bridge material through the use of a coring machine. The other involved blind hole drilling on the plate surface on or near selected weldments.

4.2 RESIDUAL STRESS DETERMINATION FROM CORING

The core specimens used to obtain residual stress data were 3.5 in. (8.9 cm) diameter through-thickness cylinders removed from the West Linn Bridge. Measurements were made to determine the extent of strain relief due to initial core removal from the bridge. A second set of strain relief measurements were made as the cores were sectioned for subsequent machining into fracture toughness specimens. The measurement results and interpretation of these results are summarized in this chapter.

Relief strain of the cored material is what is measured experimentally. These core-related strain measurements can then be used to calculate "nominal" core-related relief stresses. Residual stress present in the structure prior to core removal is equal in magnitude and opposite in sign to relief stress. However, assessment of the actual (through-thickness) residual stress distribution can not, in general, be made simply by taking the measured relief stresses and changing their sign. The measured relief stresses yield general information on the change in dimensions and stress state of the individual cut sections of the structural component under investigation, but do not necessarily provide a composite picture of the actual residual stress state of the original uncut structure. The relief stress measurements can be used as an indication of the residual stress state in the original structure, but the actual residual stress state analysis is complex and can not be determined by simple analysis of core-related relief stresses.

A major problem with using the core-related strain relief measurements for subsequent residual stress analysis is that the strain relief sample geometry was decided upon based on the need for fracture toughness specimens; it was not an optimum geometry for strain relief measurements. Strain relief specimen geometry is preferably a narrow slice of material parallel to the desired strain/stress direction to be measured. This allows one to consider the strain/stress perpendicular to the analyzed direction to be essentially zero, thus greatly simplifying results interpretation. A cylindrical specimen geometry, which was used in this study, requires measuring and assessing strains parallel and perpendicular to the desired analysis direction, thus greatly complicating data

interpretation. Complete interpretation of the complex stress/strain changes measured in this study would require complex FEA and is beyond the scope of this project.

The measured relief strain/stress results from this study will simply be assessed as being indicators of surface related strain/stress. This approach is, in actuality, correct as the experimentally measured strains are surface strains. The initial coring operation would be expected to generate the major amount of surface relief, with the subsequent sectioning of the core yielding a second-order effect on relieved strain/stress.

One would actually like to determine the relieved surface strain/stress by tree-panning a thin, strain-gaged, surface layer of material directly from the bridge. However, one can postulate that the value of the relief strains/stresses of a tree-panned slice will be similar to the cumulative cored and sliced relief values, because the multiple cutting operations will essentially free the last slice of all connections to the rest of the bridge material.

A first approximation of the stress state of the surface material associated with the bridge will be given below. The initial coring results are assessed first, and then the cumulative coring plus slice results are discussed. The data and trends are compared to the ESW FEA model results.

4.3 CORE REMOVAL AND SUBSEQUENT SECTIONING

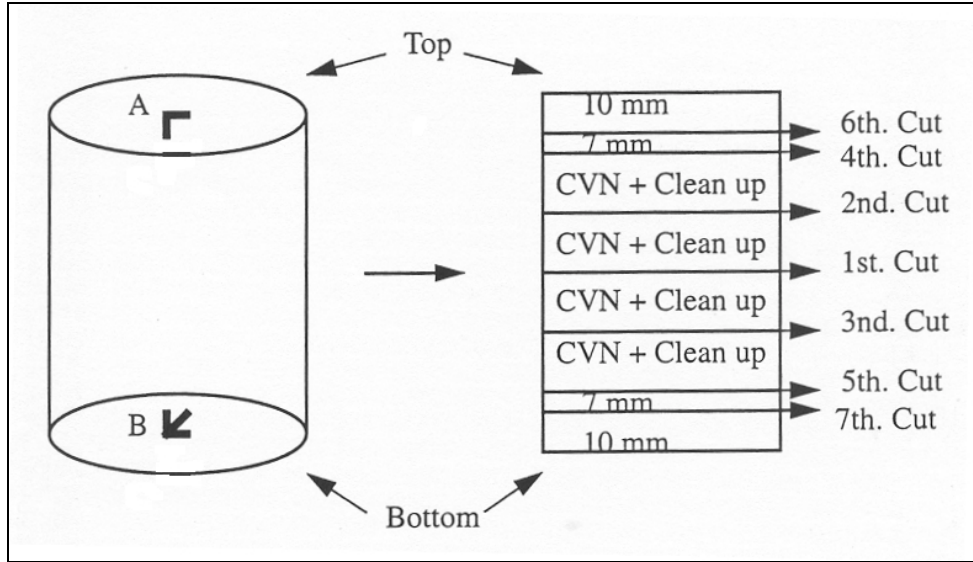
Fourteen cores were removed from one of the four box girders by ODOT personnel, Table 4.1. The cores were removed from ES weldments in compression loading on the bottom flange of the box girder.^[73] Of the fourteen cores that were recovered from the bridge, two were base-metal specimens, five were WCL specimens, and the remaining seven were HAZ specimens. The WCL specimens were centered between the fusion zone edges, as determined by grinding and then etching with nital. The center point of the HAZ specimens was placed 0.5 in. (1.27 cm) out from the top surface fusion zone edge per suggestions from Devletian at OGI. This was a best guess technique used to center the mid-thickness of the core specimen on the fusion zone boundary for subsequent fusion zone/coarse-grained-region HAZ toughness specimen placement.

Table 4.1: Core identification number and description.

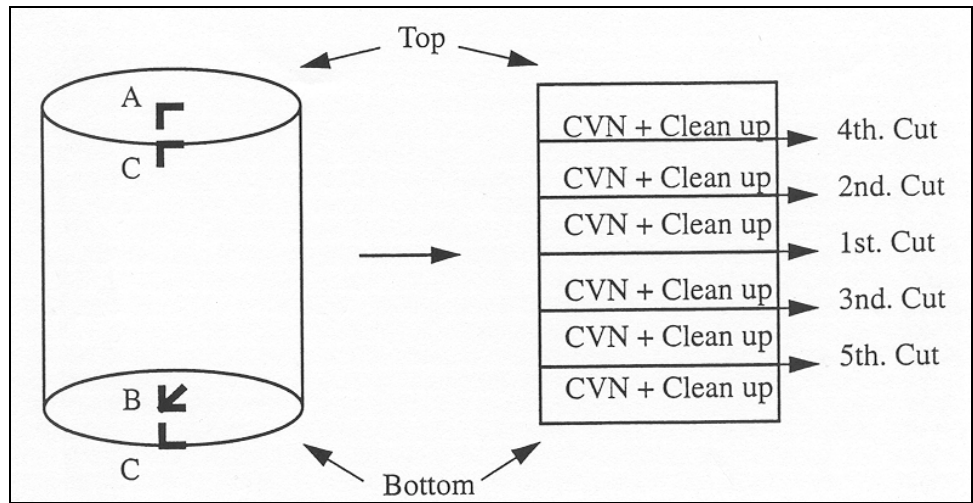
Number	Core ID	Core Type	Strain Gaged		Test Type
			Coring	Sectioning	
1	B1+4	Base Metal	Yes	Yes	FT
2	B3B1	Centerline	Yes	Yes	FT
3	B3B2	HAZ	Yes	Yes	FT
4	B7B1	HAZ	Yes	Yes	FT
5	B7B2	HAZ	Yes	Yes	FT
6	C3B1	HAZ	No	Yes	FT
7	C3B2	Centerline	No	Yes	FT
8	C7B1	HAZ	Yes	Yes	FT
9	C7B2	Centerline	Yes	Yes	FT
10	D3B1+8	Base Metal	Yes	Yes	CVN
11	D3B1	Centerline	Yes	Yes	FT
12	D3B2	HAZ	Yes	Yes	CVN
13	D7B1	HAZ	Yes	Yes	FT
14	D7B2	Centerline	No	No	CVN

Electrical resistance strain gages were attached to eleven of the fourteen cores prior to removal from the bridge. The majority of the cores had two-gage 90° weld-on rosettes; selected cores had two single weld-on gages attached at 90° to each other. The gages were oriented parallel and perpendicular to the welding direction. The gages were zeroed using a Somat 2100 field computer. A hydraulically powered drilling machine specially fabricated for ODOT cut out 3.5 in. (8.9 cm) diameter cores in about 90 seconds. Lubricant was used to cool the cores during cutting.^[73] The cores were caught as they fell towards the Willamette river after being cut out of the bridge plate. A follow-up set of strain measurements was made to determine the strain/stress relief due to the coring operation.

At OGI, three-gage, 45° rosettes were attached to what would have been the bottom of the cores and zeroed using a Vishay Model 2100 strain gage conditioner and amplifier system. The cores were subsequently sectioned at OGI using an automatic-feed band saw with a slow cutting speed of 50 feet/minute, 30 pounds load and continuous coolant to minimize heating. After each slice, the strain gages were interrogated to determine the change in strain. The thickness for each slice and the cut sequence are shown in Figure 4.1 for each core. The slice thicknesses were determined by the type of toughness test desired out of the given slab of material. The Charpy V notch (CVN) test required a 10 mm (0.394 in.) thick test specimen and the fracture toughness test required an 2.54 cm (1 in.) thick test specimen. The fracture toughness test conducted on each of the cores is presented in Table 4.1.

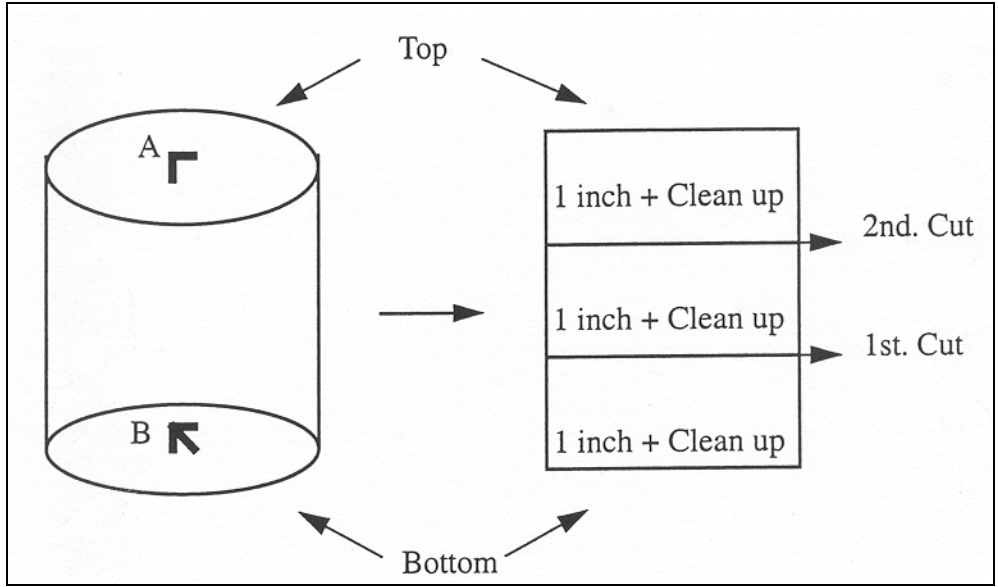


(a) D3B2

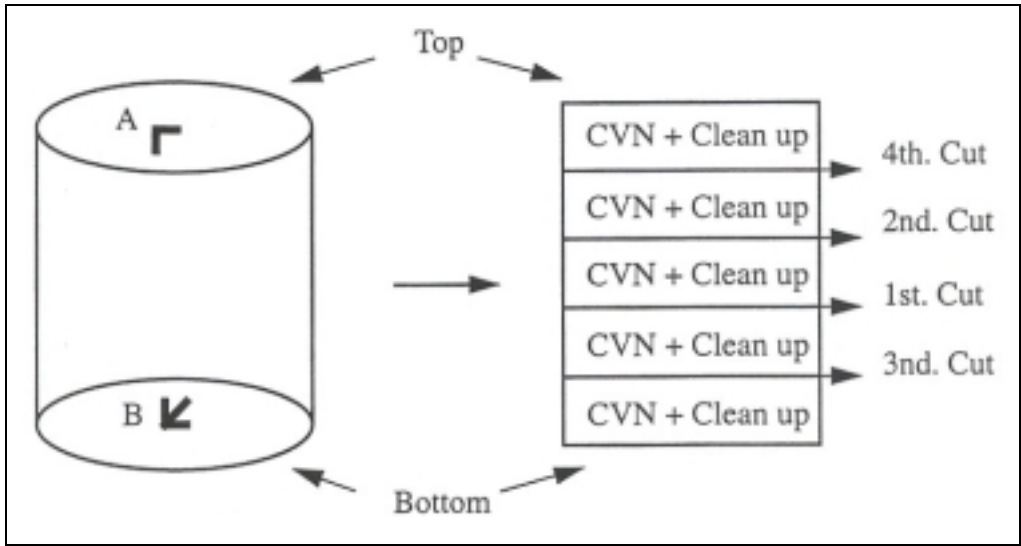


(b) D3B1+8

Figure 4.1: Strain gage positions, cutting sequence, and slice thickness for West Linn Bridge cores. Gage labels A – F refer to the gage type given in Table 4.1.

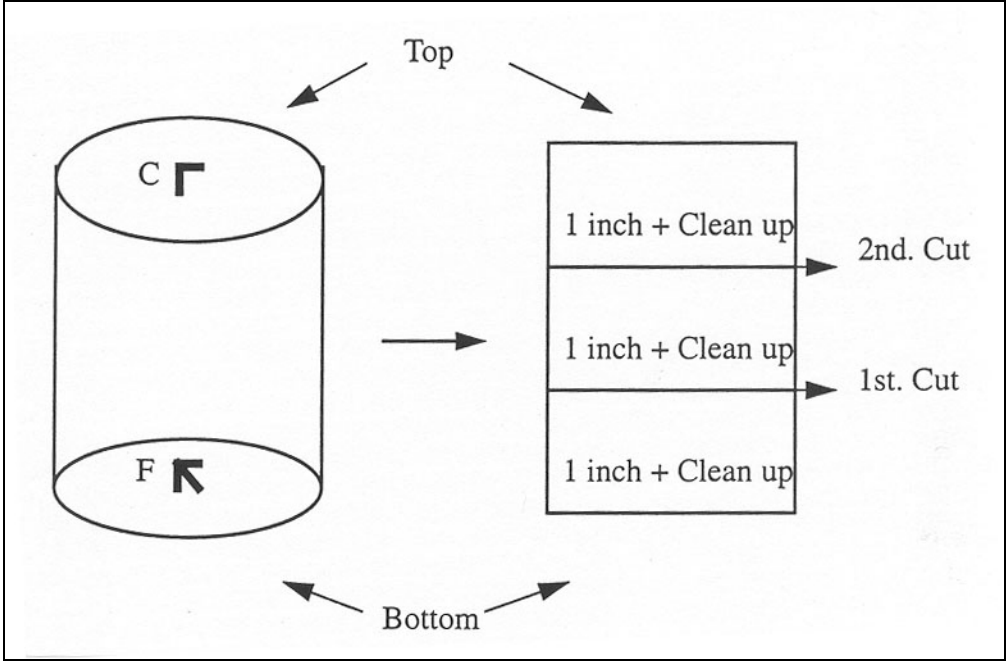


(c) B3B1, D3B1

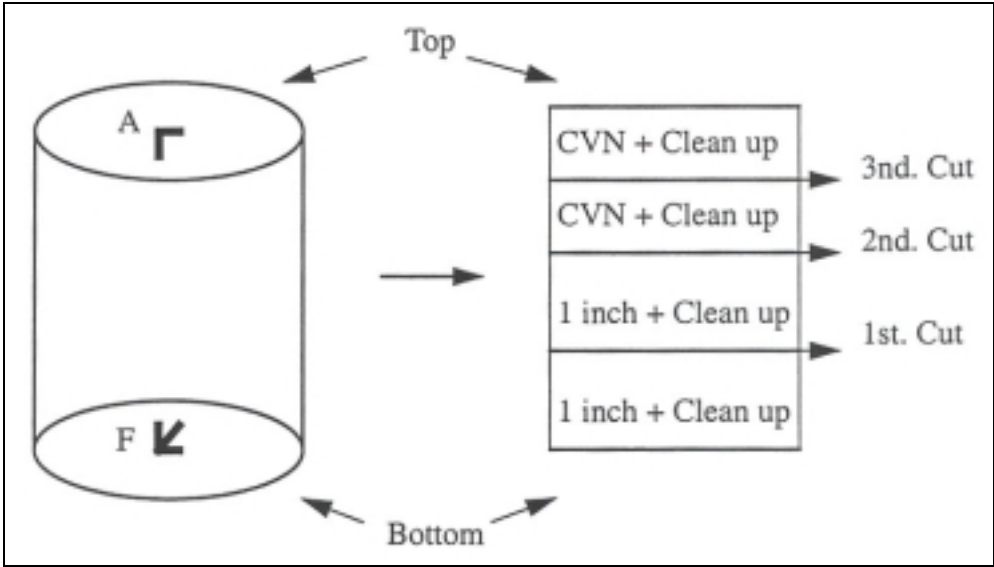


(d) C7B2

Figure 4.1 (continued): Strain gage positions, cutting sequence, and slice thickness for West Linn Bridge cores. Gage labels A – F refer to the gage type given in Table 4.1.

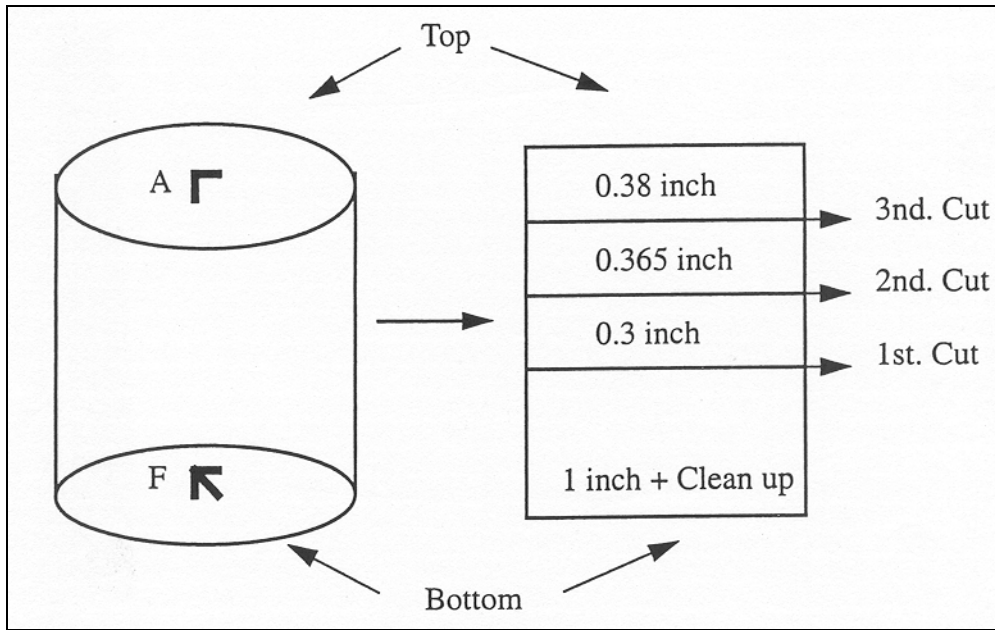


(e) C3B2

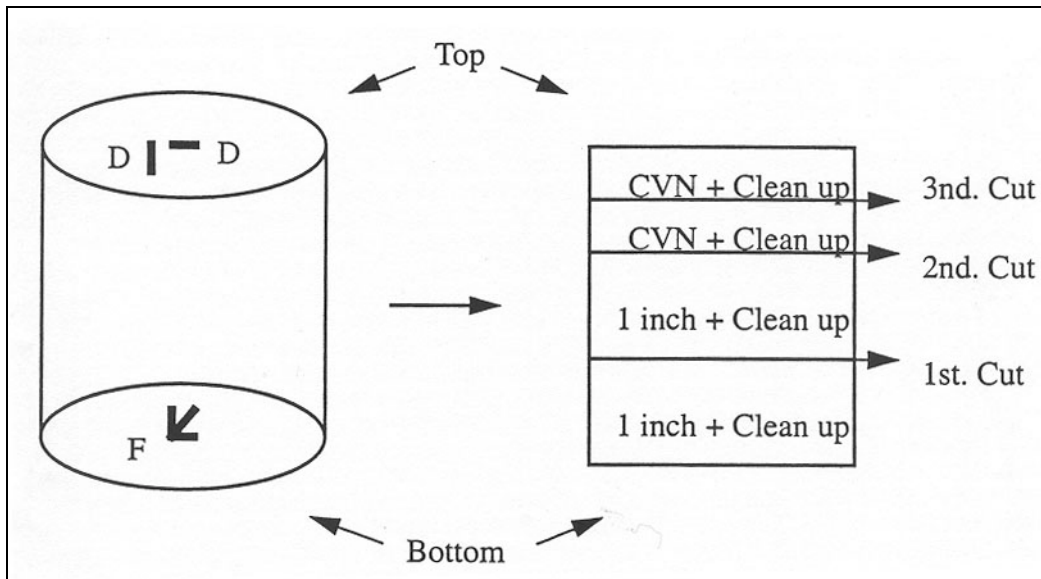


(f) D7B1, B7B2, B7B1

Figure 4.1 (continued): Strain gage positions, cutting sequence, and slice thickness for West Linn Bridge cores. Gage labels A – F refer to the gage type given in Table 4.1.

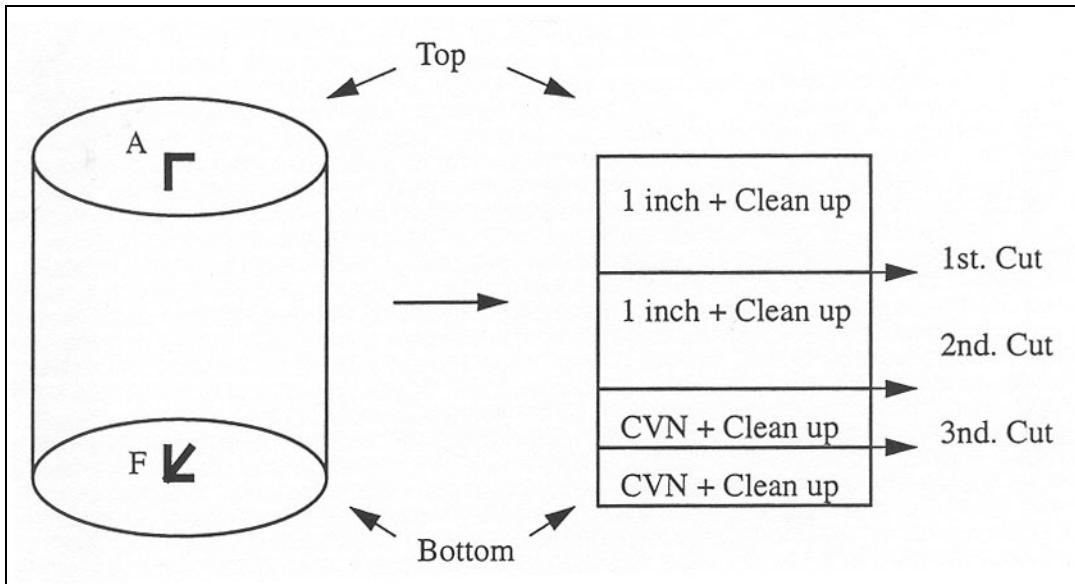


(g) B1+4

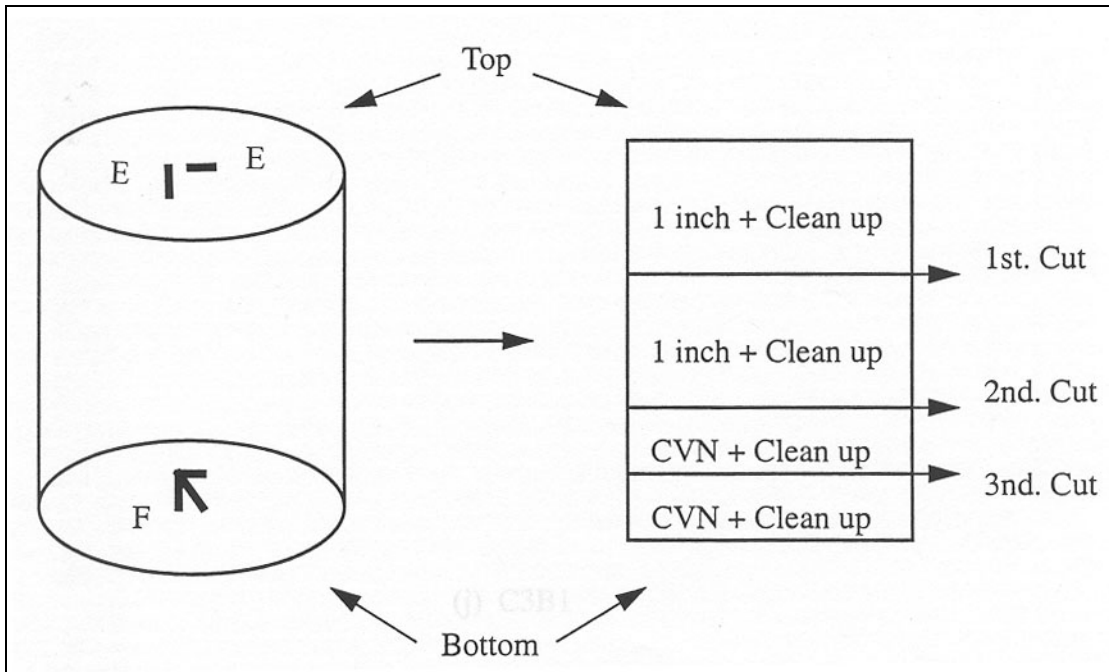


(h) C7B1

Figure 4.1 (continued): Strain gage positions, cutting sequence, and slice thickness for West Linn Bridge cores. Gage labels A – F refer to the gage type given in Table 4.1.



(i) B3B2



(j) C3B1

Figure 4.1 (continued): Strain gage positions, cutting sequence, and slice thickness for West Linn Bridge cores. Gage labels A – F refer to the gage type given in Table 4.1.

Three strains at a point should be measured to completely define either the stress or the strain field. The elastic constants such as elastic modulus E and Poisson's ratio ν of the specimen

material need to be known for conversion of the strains into stresses. With three strains at a particular point, principal strains and principal angle can be calculated. The principal angle is defined as the angle between the x axis (defined in relation to a designated gage on the rosette) and one of the principal strain directions. One can reduce the number of gage elements required from three to two if the principle stress directions are known. For the 90° rosettes applied before coring, it was assumed that the principal stress directions were perpendicular and parallel to the welding direction.

The six types of strain gages that were used for strain relief measurement are described in Table 4.2, and the specific gage type used with a given core is noted in Figure 4.1 The detailed procedures used at OGI for strain relief slice-related measurements are given in Zhang’s Ph.D. Thesis.^[63]

Table 4.2: Description of strain gage type used for coring and slicing strain change measurements.

Gage	Type	Resistance at 24°C, Ohms	Transverse Sensitivity at 24°C	Gage Factor
A: two-gage rosette	LWK-06-W250D-350	350.0±0.4%	-4.0±0.2%	2.04±1.0%
B: three-gage rosette	CEA-06-250UR-350	350.0±0.4%	g1,3 = 0.4±0.2% g2 = 0.2±0.2%	g1,3 = 2.095±0.5% g2 = 2.105±0.5%
C: two-gage rosette	CEA-06-125UR-350	350.0±0.4%	g1 = 0.7±0.2% g2 = 0.5±0.2%	g1 = 2.105±0.5% g2 = 2.120±0.5%
D: one-gage rosette	LWK-06-W250B-350	350.0±0.4%	-4.7±0.2%	2.02±1.0%
E: one-gage rosette	WK-06-125AD-350	350.0±0.4%	-2.1±0.2%	2.02±1.0%
F: three-gage rosette	EA-06-062RB-120	120.0±0.4%	g1,3 = 1.3±0.2% g2 = 0.8±0.2%	g1,3 = 2.040±0.5% g2 = 2.045±0.5%

The strain relief measurements from the coring operation are presented in Table 4.3. Each core is identified by core number and core type, i.e., base metal, WCL or HAZ. The actual measured strain values as well as the corrected calculated strain values and associated stress relief are given in the table. The corrected calculated strain incorporates the transverse strain sensitivity factor of the gages to account for strains that are perpendicular to the strain sensing direction. The techniques used to assess effective relief stresses associated with the measured relief strains are given in Zhang’s Ph.D. thesis^[63].

Table 4.3: Bridge coring strain gage and stress relief information.

Core ID	Strain Gage Direction Relative to Box Girder Length or ESW Direction		Measured Strain (ue)	Calculated Strain (ue)	Stress Relief Associated with Core, ksi
	Girder	ES Weld			
B1+4	Longitudinal	(Perpendicular)	160	179.5	10.3
	Lateral	(Parallel)	429.9	442	16.3
B3B1	Longitudinal	Perpendicular	799.8	762.4	13.6
	Lateral	Parallel	-1180	-1163	-30.8
B3B2	Longitudinal	Perpendicular	959.8	924.5	19.0
	Lateral	Parallel	-1180	1156.5	-29.0
B7B1	Longitudinal	Perpendicular	879.8	864.1	22.1
	Lateral	Parallel	-669.8	-642.9	-12.6
B7B2	Longitudinal	Perpendicular	709.8	683.4	14.0
	Lateral	Parallel	-879.9	-862.6	-21.7
C7B1	Longitudinal	Perpendicular	1139.7	978.7	27.0
	Lateral	Parallel	-619.8	-532.2	-7.90
C7B2	Longitudinal	Perpendicular	789.9	678.3	12.3
	Lateral	Parallel	-1180	-1013.3	-26.7
D3B1+8	Longitudinal	(Perpendicular)	759.6	769.1	25.6
	Lateral	(Parallel)	-10	20.6	8.3
D3B1	Longitudinal	Perpendicular	509.7	473	5.1
	Lateral	Parallel	-1069.6	-1062.9	-30.4
D3B2	Longitudinal	Perpendicular	919.5	894.2	20.6
	Lateral	Parallel	-919.6	-894.3	-20.6
D7B1	Longitudinal	Perpendicular	919.5	902.7	23.0
	Lateral	Parallel	-709.7	-681.7	-13.5

Note: C3B1, C3B2 and D7B2 Core Specimens were not strain gaged prior to coring.

The strain relief measurements for both the coring and slicing operation are given in Appendix A, Tables A-1 through A-13. The tables include the calculated strains, associated relief stresses, and the depth of each slice. For the 45° rosettes, the direction of the principal axis is defined as an angle relative to one of the gages.

4.3.1 Relief Strains from Coring

Core-related relief strain results from Appendix A, Tables A-1 through A-13 are plotted in Appendix B, Figures B-1 through B-13. These graphs plot relieved strain as a function of slice distance from the 45° rosette surface. The strain relief value plotted at full thickness is the value obtained from the original coring operation. Note that the coring-related values are only correct for the top surface 90° gage results; plots for the bottom surface 45° gage results use the top surface coring value, as no bottom surfaces were instrumented prior to the coring operation. The results assume that the residual stress/strain is symmetrical in relation to the ES weld mid-plane, a reasonable assumption for an idealized ES weld. This assumption is not necessarily a reasonable one for the resultant superimposed composite residual stress field associated with the base ES welds plus the cosmetic repairs welds, which are present on all but one surface of the cored West Linn Bridge weldments. Thus the data analysis technique used below to assess the slicing data from core surfaces not having coring-related strain relief measurements is inherently suspect. Nevertheless, the authors used this methodology in an attempt to assess general trends using all data generated in the core-slicing study. For cores that had no strain gage rosette attached prior to core removal (C3B1, C3B2), average core drilling strain relief values from similar type specimens were used as an estimate of the coring-relieved strains to allow evaluation of the slicing results.

One expects the major surface strain/stress relief contribution when the core is initially cut out of the bridge, as this directly relieves strains present in the plane of the surface. The major effect of subsequent core slicing would be expected to be the release of strains/stresses in the through-thickness direction with a related Poisson's relief effect in the surface plane.

The general pattern of experimentally determined strain relief seen in the majority of the results appears to be as follows:

- the major strain relief takes place during the coring operation,
- a secondary change of opposite sign to that exhibited during coring takes place when the cut farthest away from the strain-gaged surface is cut,
- subsequent slicing events closer to the strain-gaged surface result in decreasing change in relief strain.

All slicing-induced changes tend to yield strain relief of the opposite sign from that observed in the original coring operation. There are, however, a substantial number of cores that do not exhibit this behavior for any one or for all of their measurements. The discrepancy between relief data for the two base metal cores is a good example of specimen results divergence. The authors expected the base metal data to be the best-behaved set of data, as exemplified by the B1+4 base metal data. Yet the D3B1+8 base metal slicing-related results are entirely different in form than the B1+4 results, Figures 4.2 and 4.3. It is not known if these latter results are real or

data collection errors. The authors' prejudice is that the coring results are reasonable, but the slicing results are not. More coring tests would need to be made to assess this question for base metal as well as for WCL and HAZ specimens.

4.3.2 Residual Stresses from Coring

The core-related stress values from Appendix A, Tables A-1 through A-13 are plotted as bridge-related residual stresses in Appendix C, Figures C-1 through C-13. The negative of the Table A-1 through A-13 estimates of surface relief values are used below as estimates for bridge-related surface residual stresses. The authors expected the coring plus slicing values to asymptotically approach the actual surface residual stress as material was removed from the core. The data extrapolations used to extract surface residual stress estimates are shown on the plots.

The first set of results that will be assessed as bridge residual stress are the coring results from the 90° rosettes, Figures 4.2 through 4.6. The base metal coring residual stress results are shown in Figure 4.2 as a function of gage direction and plate thickness.

The coring results indicate that the residual hot-rolling-induced surface stresses in both directions are compressive. The expected dead loads on the thinner (2.5 in. (6.4 cm) thick) B1+4 core material are predicted to be nominally zero, while the dead loads on the thicker (3.5 in. (8.9 cm) thick) D3B1+8 core material are predicted to be –10 ksi longitudinal to the beam (perpendicular to the ES weld) direction and nominally zero in the cross-beam (parallel to the ESW) direction.^[73] The results of subtracting –10 ksi load from the longitudinal direction for the thick plate brings the thick plate longitudinal residual stress value up to approximately the thin plate value. The results indicate that both plates exhibit a nominal –15 ksi surface residual stress in the direction parallel to the ES weld and a nominal –10 ksi surface stress in the direction perpendicular to the ES weld.

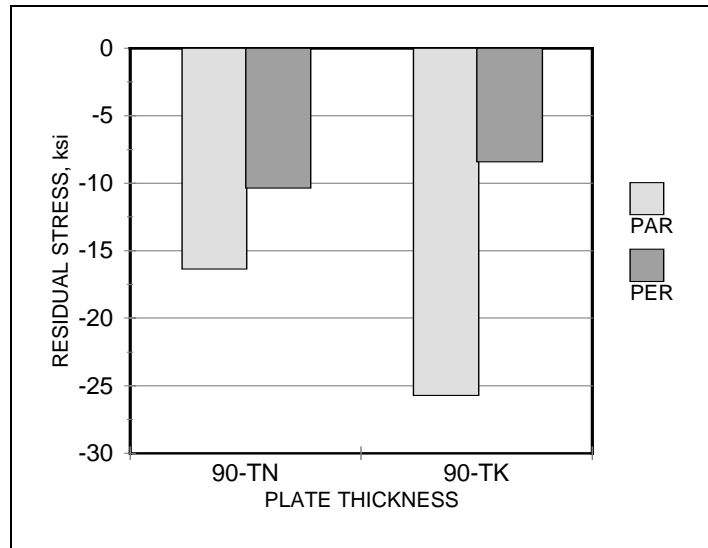


Figure 4.2: Calculated residual stress for the base metal cores. TN = 2.5 in. thick plate; TK = 3.5 in. thick plate; PAR = parallel; PER = perpendicular; 90 = 90° two-gage rosette.

The WCL coring results are shown in Figure 4.3 as a function of gage direction, i.e., parallel and perpendicular to the ESW direction. The results indicate that the weld area exhibits 25 to 30 ksi residual stress parallel to the welding direction and -5 to -10 ksi perpendicular to the welding direction. In Figure 4.4 the WCL coring results are presented again, with the -10 ksi bridge-structure-induced load in the direction perpendicular to the welding direction subtracted. This increases the weld-induced residual stresses in this direction to -5 to 5 ksi. Note that no correction due to plate fabrication induced residual stresses are required, as almost the complete volume of the WCL cores are weld metal. In addition, the majority of the small portion of original plate material which remains was subjected to relatively high temperatures during ESW, and it is expected that this would result in stress relieving of any fabrication-induced residual stresses.

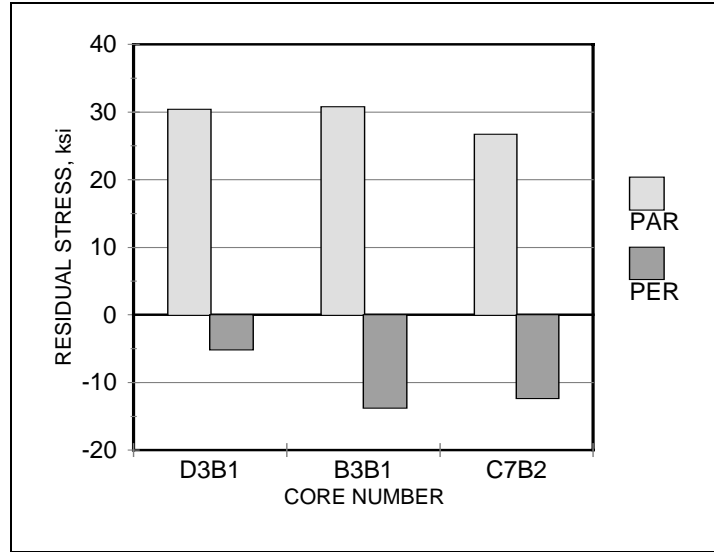


Figure 4.3: Calculated residual stress for the weld centerline cores. PAR = parallel; PER = perpendicular; 90 = 90° two-gage rosette.

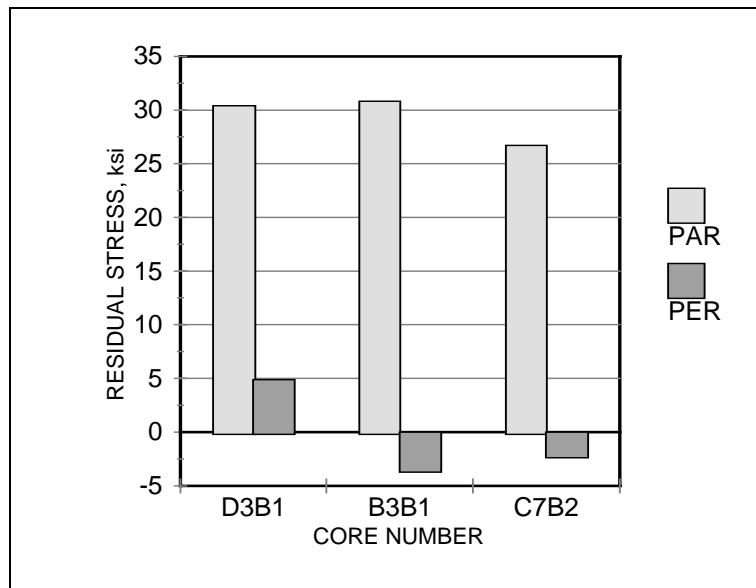


Figure 4.4: Calculated residual stress for the weld centerline cores minus the stress due to dead load (total stress - [-10 ksi] perpendicular to the welding direction). PAR = parallel; PER = perpendicular; 90 = 90° two-gage rosette.

The HAZ coring results are shown in Figure 4.5 as a function of gage direction, i.e., parallel and perpendicular to the ESW direction. The results indicate that the HAZ core area exhibits 10 to 30 ksi residual stress parallel to the welding direction and -15 to -25 ksi perpendicular to the welding direction. Both the parallel and perpendicular HAZ residual stress results exhibit a greater range of stress values than the WCL core results, Figure 4.3. The HAZ parallel direction results exhibit much lower residual stress values than the WCL results and the perpendicular HAZ results exhibit higher to much higher compressive residual stresses than the WCL results. The subtraction of the -10 ksi dead load perpendicular to the welding direction, Figure 4.6, results in a range of compressive residual stress in that direction of -5 to -15 ksi.

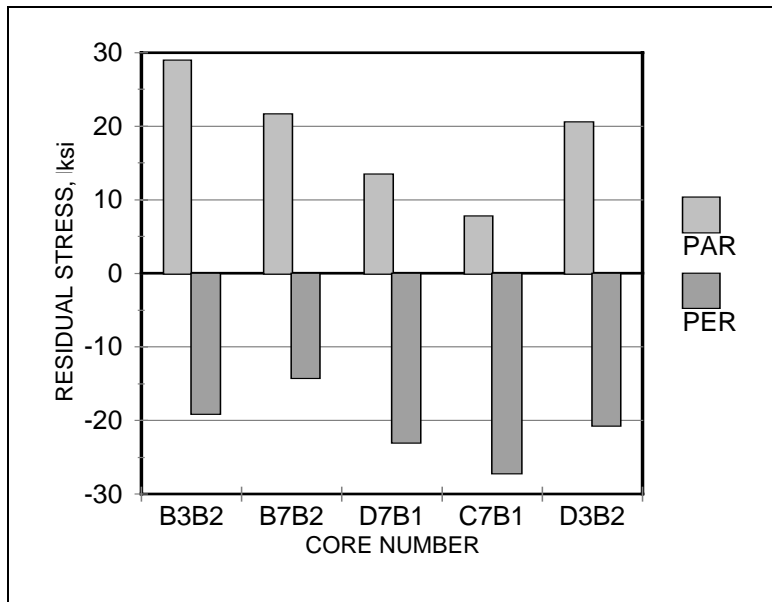


Figure 4.5: Calculated residual stress for the heat affected zone cores.
 PAR = parallel; PER = perpendicular; 90 = 90° two-gage rosette.

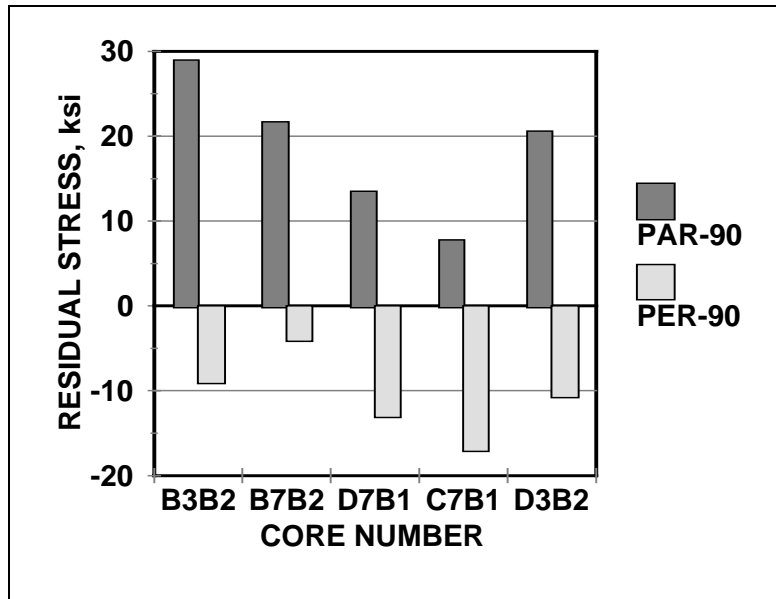


Figure 4.6: Calculated residual stress for the heat affected zone cores minus the stress due to dead load (total residual stress – [-10ksi] perpendicular to the welding direction). PAR = parallel; PER = perpendicular; 90 = 90° two-gage rosette.

It may be appropriate to make a correction in residual stress values for the HAZ core due to the rolling-induced residual stress results. However, a decision on how much to correct is difficult, and the authors feel that this would require a FEA analysis, which is beyond the scope of this project. The problem arises because nominally at least half of the HAZ core material is either weld metal or HAZ material that has seen over 1200° C. The former material would not have rolling-induced residual stress to start with, and the latter material would be expected to anneal out any rolling-induced residual stresses. Thus one is left with subtracting a maximum of 5 to 7 1/2 ksi compressive stress from the measured stresses, assuming that the specific area where the strain gages were placed had (any) rolling-induced residual stresses.

Also, as the experimental results show greater variation than these values, it is felt that attempting to adjust for rolling-induced residual stress would be an academic exercise. However, any remaining effect of rolling-induced stresses would be to increase the measured weld-induced residual stresses in a tensile direction.

4.3.3 Residual Stresses from Coring and Sectioning

The base metal coring plus sectioning results are presented in Figure 4.7. Note that these values are more speculative than the coring results. This is because the values presented in these graphs, and all subsequent graphs in this section, are the negative of the extrapolated intercept value at zero plate thickness from the relevant stress relief graphs previously presented in this chapter. This stress estimation procedure assumes that the cumulative stress (measured strain) from coring and slicing is equal to the expected stress measurement that would result if the near-surface material were tree-panned from the beam. Use of this stress estimation technique

assumes that all strain readings were correct, as any incorrect reading will compromise the complete analysis since the results are additive.

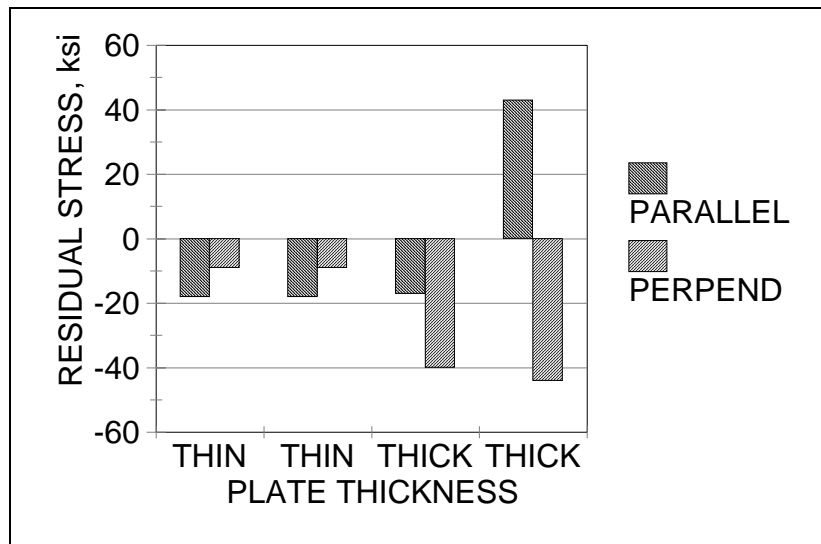


Figure 4.7: Calculated residual stress for the base metal cores. THIN = 2.5 in. thick plate; THICK = 3.5 in. thick plate.

The 2.5 in. thick base metal residual stress values labeled “thin” in Figure 4.7 appear to be reasonable, while those for the 3.5 in. thick base metal do not. The thinner base metal residual stress values are very close to the originally measured coring values, as would be expected. The thicker base metal yields residual stress values very different from the coring results and very different between gage types, with the first set of readings being from the pre-coring gages and the second set of readings being from the post-coring gage set. No obvious explanation for the discrepancy in these results is known to the authors. It does point out, however, that residual stress readings are somewhat of an art, and major variations can be found in even the most controlled situations.

The coring plus slicing estimates of bridge-related residual stress values for the WCL and HAZ specimens are even more speculative in interpretation than the base metal coring plus sectioning results. This is due to two major factors. The first is that there were no coring strain relief measurements taken on the “bottom” side of the cores. Assessment of the bottom side coring plus sectioning results relies on the assumption that the ESW residual stress field is symmetrical with respect to the weld mid-plane. This symmetry assumption problem is also true for the base metal specimens discussed above. This is not an unreasonable assumption to make for an idealistic weld modeling situation. It is more difficult to justify in a “real world” situation where grossly off-centered weldments are possible. However, the West Linn Bridge-specific fusion line assessments given in Chapter 2 indicate that the assessed welds are reasonably symmetrical, even with the noted fabrication perturbations. The much more serious problem for this specific set of welds is the presence of cosmetic fusion line repair welds on essentially every weld surface.

One to four manual metal arc welds (MMAW) were present on each fusion line except one assessed in this study; one weld surface exhibited MMAW completely across the fusion zone surface. The authors assume that the placement of supplemental MMAWs at the fusion lines of the ES welds was standard practice for this fabricator. This indicates that their shoe was incorrect for their welding conditions. Rather than increase the relief in their shoes to fix their fusion line under-cut problem, they chose to apply post-weld MMAWs to the ES welds. Another complicating factor in assessment of this post-weld repair procedure is that microstructure studies by Devletian found that some of the MMAW welds had received a correct preheating treatment while others had not. Thus, the potential differences in MMAW associated material strength due to differences in heat treatment, plus the large discrepancy between the number of MMAW weld beads laid down on the four fusion lines associated with each core make the assumption of mid-plane, or for that matter, fusion zone side-to-side symmetry suspect. Nevertheless, all data is used below in an attempt to assess ESW weld-induced residual stress trends.

The WCL coring plus sectioning residual stress estimates are shown in Figures 4.8 to 4.10. The resultant residual stress values as a function of core number are presented in Figure 4.10. One can see that average residual stress values, both parallel and perpendicular to the welding direction, have increased over the values found for the coring results alone. The stresses perpendicular to the welding direction range from slightly compressive to half of the yield strength. The stresses parallel to the welding direction are around yield strength levels. Assessment of stresses by gage type indicates that the 45° gages, which were assigned the as-cored strain relief values from the 90° top side gages, may exhibit higher stresses than the 90° gages, if the fourth 90° gage results are disregarded, Figure 4.9. For the orientation perpendicular to the welding direction, subtracting the -10 ksi dead load stress, results in the stresses in the perpendicular direction, all being in tension, except for the B3B1 core, Figure 4.10. Thus, both stress components are now in the tension regime.

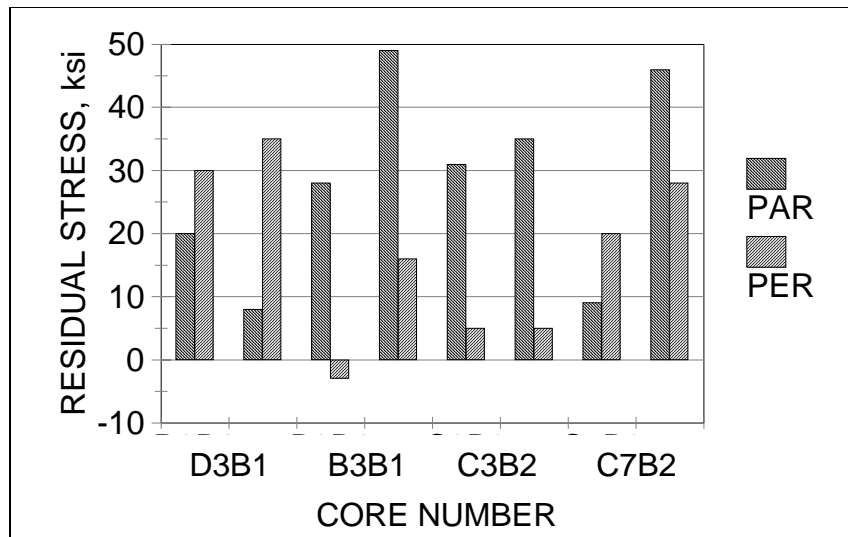


Figure 4.8: Calculated residual stress for the weld centerline cores. The two sets of values for each core are due to the two strain gage rosettes on each core. PAR = parallel; PER = perpendicular.

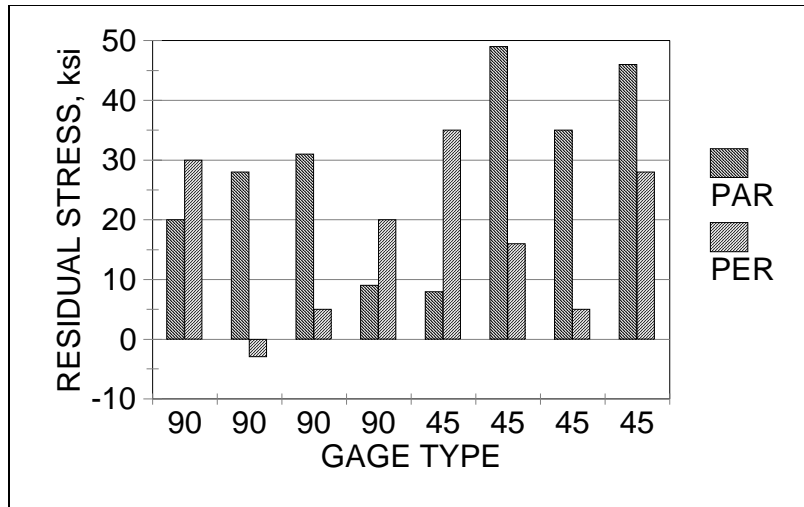


Figure 4.9: Calculated residual stress for the weld centerline cores segregated by strain gage type. PAR = parallel; PER = perpendicular; 90 = 90° two-gage rosette; 45 = 45° three gage rosette.

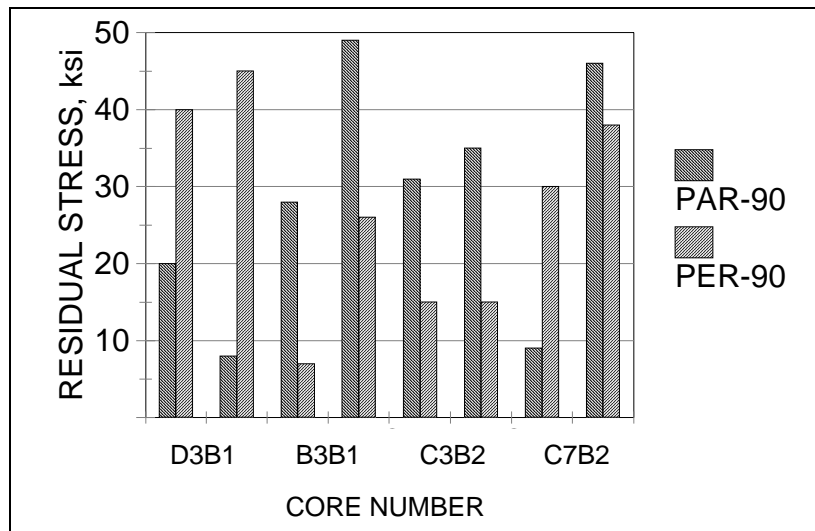


Figure 4.10: Calculated residual stress for the weld centerline cores minus the stress due to dead load (total residual stress - [-10 ksi]). The two sets of values for each core are due to the two strain gage rosettes on each core. PAR = parallel; PER = perpendicular.

The HAZ coring plus sectioning results as a function of core number are given in Figure 4.11. The majority of these results exhibit compressive stresses perpendicular to the welding direction and tension stresses parallel to the welding direction. The compressive stresses range from 1/3 to 1 times the yield strength with a nominal average of 1/2 the yield strength. Figure 4.12 illustrates that all but one of the tension values for the stress perpendicular to the welding direction, as well as the yield-plus stresses parallel to the welding direction, are associated with

the 45° rosette, which is the one that was attached after the coring operation. Over half of the HAZ results exhibit near-zero or compressive residual stress after the subtraction of the -10 ksi dead load, Figure 4.13. In addition, the majority of the tensile values for the residual stresses parallel to the welding direction are around 2/3 the yield strength. Based on these results, lower residual tensile stresses existed in the HAZ than along the WCL.

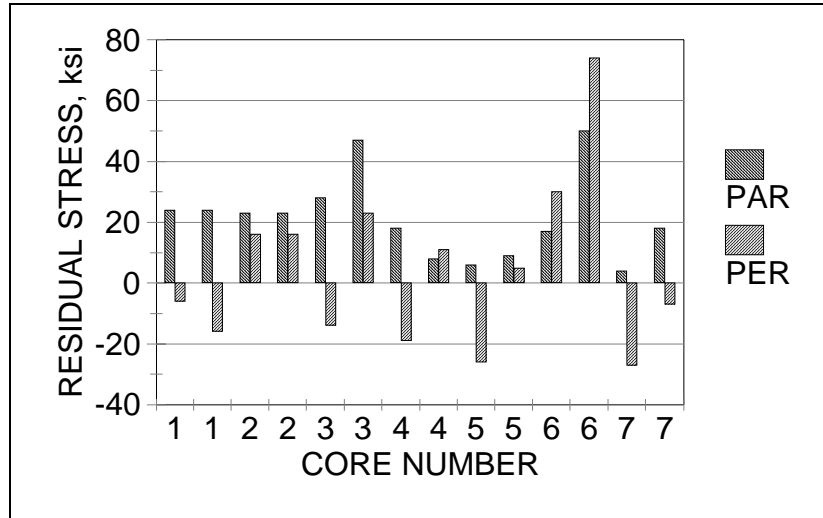


Figure 4.11: Calculated residual stress for the seven heat affected zone cores. The two sets of values for each core (1, 1; 2, 2; etc.) are due to the two strain gage rosettes on each core. PAR = parallel; PER = perpendicular.

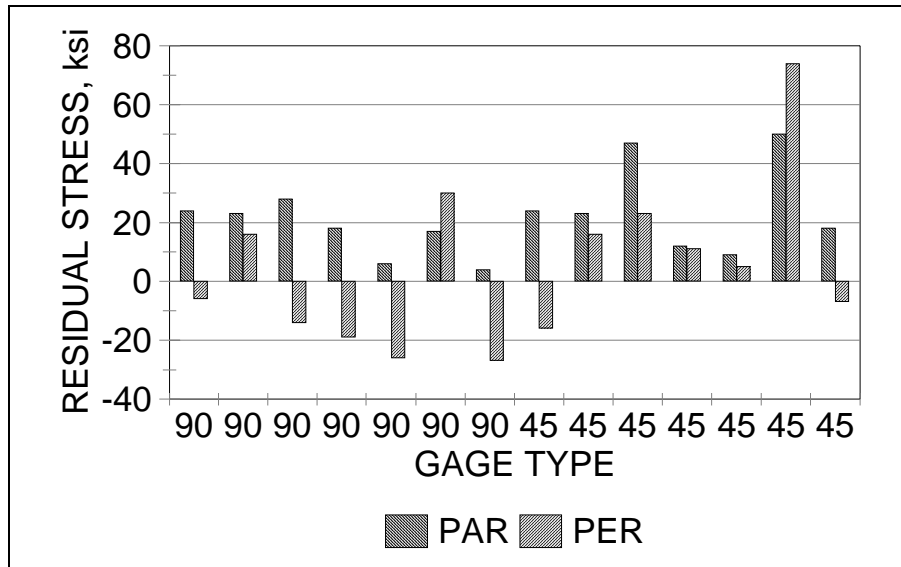


Figure 4.12: Calculated residual stress for the heat affected zone cores segregated by strain gage type. PAR = parallel; PER = perpendicular; 90 = 90° two-gage strain rosette; 45 = 45° three-gage strain rosette.

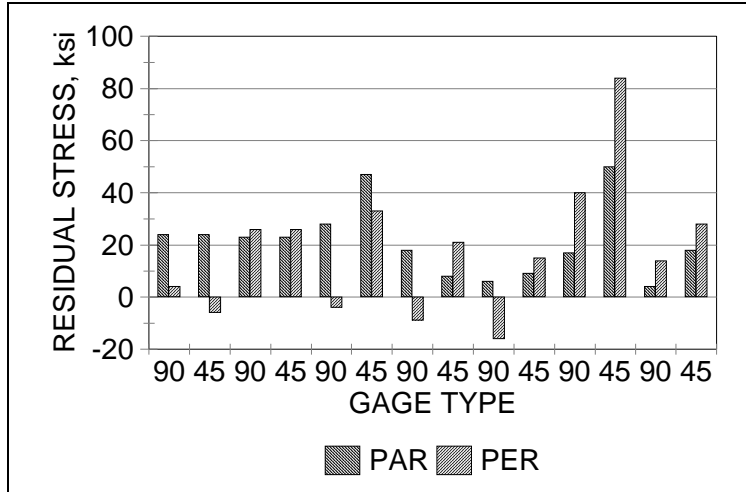


Figure 4.13: Calculated residual stress for the heat affected zone cores minus the stress due to dead load (total residual stress - [-10 ksi]).
 PAR = parallel; PER = perpendicular.

4.4 COMPARISON OF EXPERIMENTAL AND PREDICTED RESIDUAL STRESS

The surface residual stress results generated with the 3D model, Figure 4.14 and 4.15, are compared to the experimental results in Table 4.4. In the comparison, the model and experimental values are adjusted for the 10 ksi dead load. The 3D model results at 10 cm from the WCL (approximately 0.5 in. (1.3 cm) from the fusion line) were chosen for comparison with the experimentally determined HAZ coring and coring + slicing results.

Table 4.4: Comparison of 3D model surface predictions and experimental coring and sectioning ESW residual stress results.

ITEM	WCL RESIDUAL STRESS, %Yield stress		WCL + 10cm RESIDUAL STRESS, % Yield Stress	
	Maximum	Minimum	Maximum	Minimum
3D MODEL				
Parallel	13%	NA	7%	NA
Perpendicular	-13%	NA	-6%	NA
CORING RESULTS				
Parallel	84%	69%	78%	22%
Perpendicular	14%	-14%	-8%	-47%
CORING PLUS SLICING				
Parallel	139%	8%	119%	14%
Perpendicular	122%	19%	89%	-50%

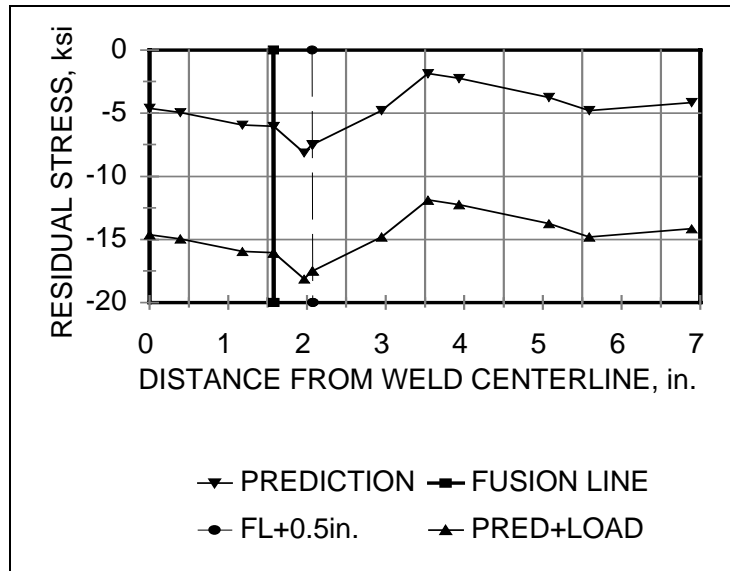


Figure 4.14: Predicted surface residual stress changes perpendicular to the welding direction as a function of distance from the weld centerline.

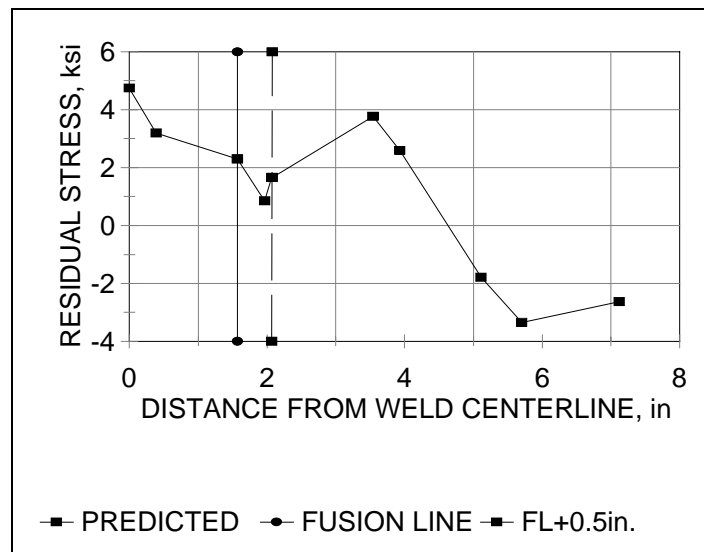


Figure 4.15: Predicted surface residual stress changes parallel to the welding direction as a function of distance from the weld centerline.

The large range in experimentally measured values makes comparisons difficult and speculative. However, a comparison of data change trends from WCL to WCL+10 cm (10 cm out from the WCL) indicates that both the predicted stresses and the measured stress value ranges parallel to the welding direction decrease with increasing distance from the WCL. The predicted stresses perpendicular to the welding direction increase with increasing distance from the WCL, while the

experimentally measured value ranges in this direction tend to decrease with increasing distance from the WCL. Both the 3D model results and the experimental results exhibit higher tension stresses in the direction parallel to the welding direction than perpendicular to the welding direction. In most cases, the experimental range of stresses are more tensile than the predicted stresses.

A major question raised by these results is whether the experimental results and, in particular, the large range of results, are reasonable. It is not possible to answer this question without further research. The problem that arises is that the presence of the fusion line/zone repair welds makes it impossible to conduct a one-to-one residual stress comparison to the ESW 3D model. The presence of these surface repair welds has the potential effect of changing the near-surface, weld-induced residual stress field from one controlled by an ES weld to one controlled by a multi-pass weld. The ESW modeling results presented herein indicate that low compressive residual stresses should be present on the plate surface perpendicular to the welding direction. Classical multi-pass measurement and modeling results indicate that one should expect yield-strength tension residual stresses on the plate surface. The programmatic test results can be interpreted either way. This may actually be correct, as the repair welds varied from one to multiple passes to complete coverage of the fusion zone. Pre-heating was also observed to be variable.

One might also expect the residual stress results in the direction parallel to the weld to be more affected by the repair welds than those perpendicular to the welding direction. This is because the MMAW beads are continuous along the length of the weld, whereas they are generally discontinuous in the direction perpendicular to the welding direction, i.e. they lie along the fusion line. The residual stress field associated with the small MMAW bead should drop off sharply with distance from the weld bead edge. This would also mean that one might expect the effect of the repair welds to be greater as one approached the surface, i.e., for cut slices closer to the surface. Thus the initial coring-related stress relief strains/stresses, and, in particular, those perpendicular to the welding direction, may be most indicative of the base ESW residual stress field than the other results. Indeed, the initial coring residual stress measurements in the direction perpendicular to the welding direction correlate best with the modeling results. However, an experimental and/or modeling assessment of the relevance of these bridge-specific results would require the assessment of a base ES weldment with multiple repair welds and preheat conditions superimposed on the base ESW residual stress field.

4.5 RESIDUAL STRESS DETERMINATION FROM HOLE DRILLING

4.5.1 Introduction

Residual stresses may be either beneficial or detrimental, depending upon magnitude, sign, and distribution of the stress with respect to the load-induced stresses^[74] Tensile residual stresses are usually detrimental and may even be the predominant factor contributing to fatigue and other structural failure mechanisms. In order to measure residual stress using strain gages, the locked-in stress must be relieved so that the sensor can register the change in strain caused by the removal of the stress. Stress relief can be done by cutting and sectioning the part, as discussed above, or by locally removing material, such as in the hole drilling technique, as discussed

below. The strain sensor responds to the deformation produced by the relaxation/re-distribution of the stress with material removal. The initial residual stress relieved by the material removal operation can then be inferred from the measured strains assuming elastic stress relaxation takes place.^[74]

An attempt was made to experimentally determine surface residual stresses on two ES weldments on the West Linn Bridge as a function of distance from the WCL. It was expected that this data would be useful in its own right and could also be used as a FEA validation data base. It was decided to use the hole-drilling strain-gage method, as presented in the ASTM E 837-95 Standard Test Method of Determining Residual Stresses by the Hole-Drilling Strain-Gage Method^[38].

The hole-drilling strain gage method of stress relaxation is the most widely used modern technique for measuring residual stress. The test method is for determining the near-surface residual stresses of isotropic, linearly-elastic materials in which the residual stress does not vary significantly with depth and does not exceed one-half the yield strength. The analysis methodology in E 837-95 also assumes that the stresses in the plane of the surface near the drilled hole are essentially constant.

There is no closed-form analytical solution for the hole drilling problem, so it is analyzed using a combination of empirical and FEA techniques.^[74] Strain data analysis yields an indication of the uniformity of the through-thickness stress gradient and whether or not one can use the ASTM E837-95 methodology for assessment of the experimental data.

Complete surface strain relaxation does not take place instantaneously once the surface is pierced by the drill. Complete surface strain relaxation requires a finite hole depth, nominally equal to, or slightly deeper than, the drill diameter. The ASTM E837-95 specification recommends that strain change be measured as a function of depth so that the result can be compared with the condition of uniform stress distribution. In Figure 4.16, strain normalized to strain measured at a hole depth equal to hole diameter is plotted as a function of hole depth normalized as a function of hole diameter. The strain envelope encompasses the expected strain relief values as a function of depth in a uniform stress distribution for three experimentally measured strain functions: $e_3 + e_1$, $e_3 - e_1$, and $e_3 + e_1 - 2e_2$ where e_1 , e_2 , and e_3 are values from a standard three-gage strain rosette. These functions are plotted in the following analysis as $e_1 + e_3$, $e_3 - e_1$, and $e_1 + e_3 - 2e_2$, respectively.^[74] Significant deviation from the strain envelope indicates that a non-uniform through-thickness stress distribution is present and/or error in strain measurement has been made. In either case, the measured data are not acceptable for residual stress calculations using the ASTM E837-95 test method.

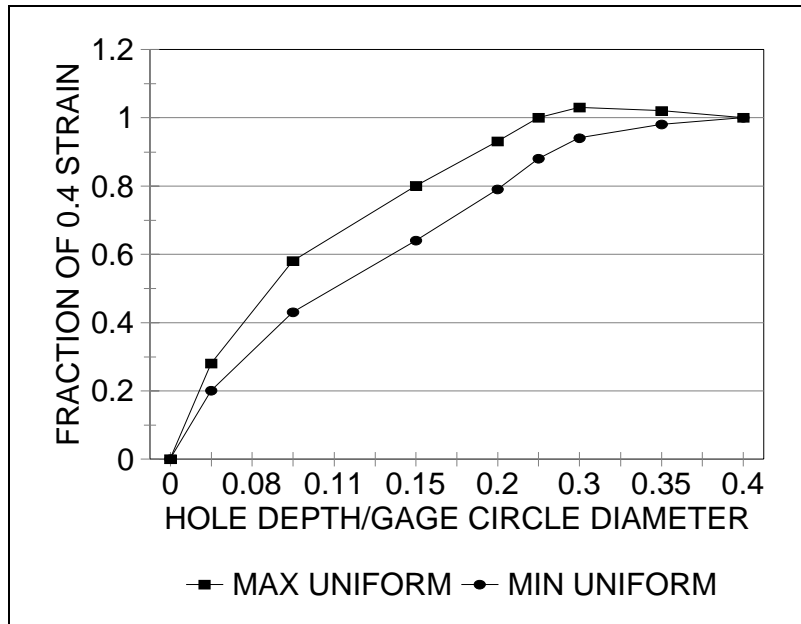


Figure 4.16: Envelope of expected strain changes for a uniform through-thickness stress state as determined by the blind-hole-drilling method as a function of normalized hole depth.

The Micro-Measurements technique suggests that an equivalent uniform stress assessment can be made if the assessment of measured data with the expected uniform strain results of Figure 4.16 indicate the presence of a through-thickness stress gradient. A nominal residual stress value is calculated for each data point in this analysis versus a residual stress for only the final data point in the uniform stress analysis. The incrementally plotted equivalent uniform stress data will be a straight line if the through-thickness stress is uniform; it will vary from a straight line if there is a stress gradient present. In the presence of a stress gradient, only the first equivalent uniform stress value is used as an estimate of the surface stress, and this measurement will more closely approximate the actual value with smaller increment thickness. Note that all equivalent stress values assume a uniform stress gradient from the surface to the bottom of the relevant hole depth. Thus all equivalent stress readings, including the first, are incorrect. However, the equivalent stress results do tend to indicate the direction of the change in stress with increasing distance from the surface.

4.5.2 Experimental Results

Two sets of residual stress hole-drilling traverses as a function of distance from the WCL were made. All hole drilling results for both sets that did not exhibit obvious experimentally-oriented problems were assessed in a variety of ways. The first analysis technique was to assess the final hole depth residual stress estimate. Almost all gages indicated compressive residual stress levels much greater than expected and/or reasonable for A36 steel. This led to an analysis of incremental residual stress reading as compared to expected reading changes for uniform through-thickness stress conditions. An example of this analysis is shown in Figure 4.17. These results indicated that all of the hole-drilling sets exhibited non-uniform through thickness

residual stresses or gage-related measurement problems. Thus the standard ASTM E-837-95 specification data analysis methodology was not applicable. Subsequent analysis using the Micro-Measurements technique produced unrealistic results, Figure 4.18, because the graph shows a residual stress greater than the compressive yield strength of the steel.

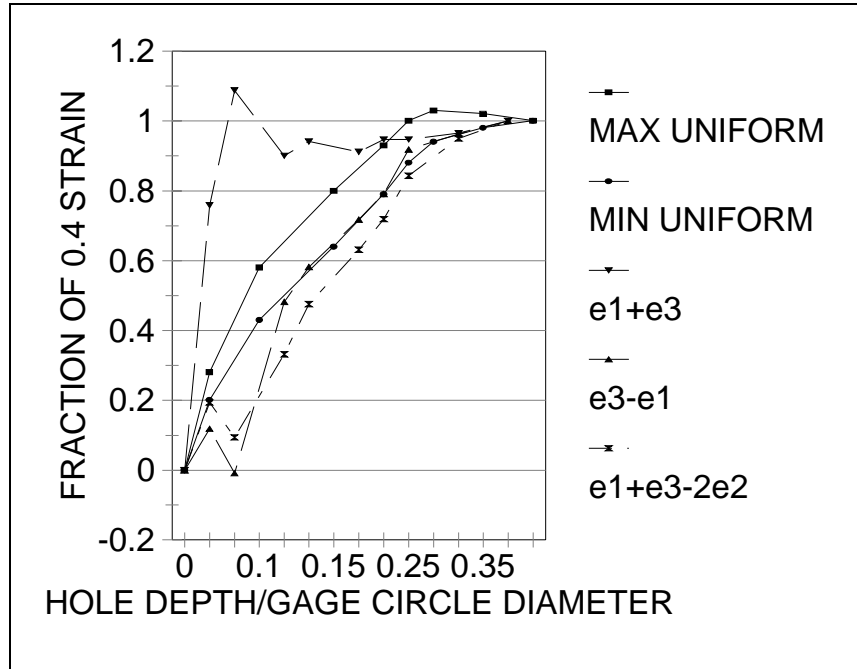


Figure 4.17: Measured strain for a hole drilled one inch from the weld centerline compared with the expected uniform through-thickness stress envelope as a function of normalized hole depth.

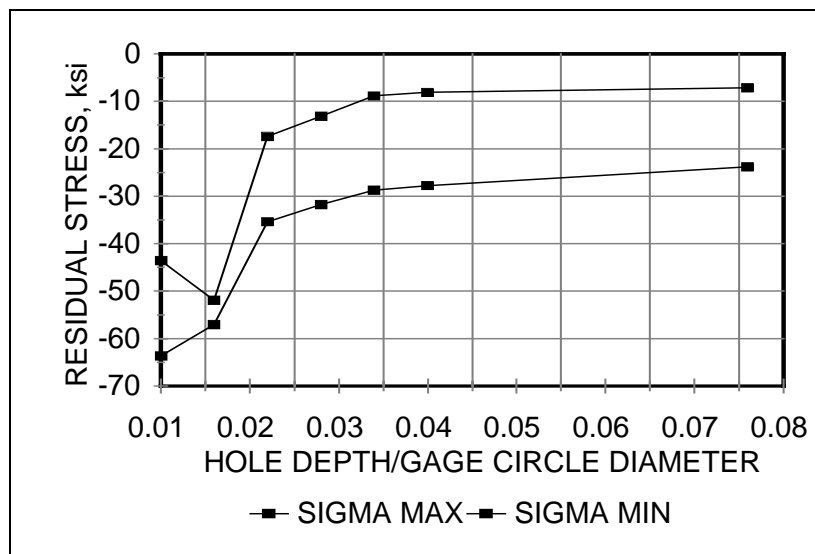


Figure 4.18: Calculated change in residual stress for a hole drilled one inch from the weld centerline as a function of normalized hole depth.

4.5.3 Discussion

The maximum and minimum principle stresses for both sets of measurements, defined as the stress in the initial increment from the equivalent uniform stress analysis, are shown in Figures 4.18 and 4.19. Neither the position-specific values for the two sets of readings nor their apparent data trends as a function of distance from WCL agree. The Set One readings vary from nominally -125 ksi to -30 ksi with a trend towards decreasing absolute stress value with increasing distance from the WCL, if the 3.5 in. reading is excluded. The Set Two readings vary from -120 ksi to +40 ksi, with no apparent trend.

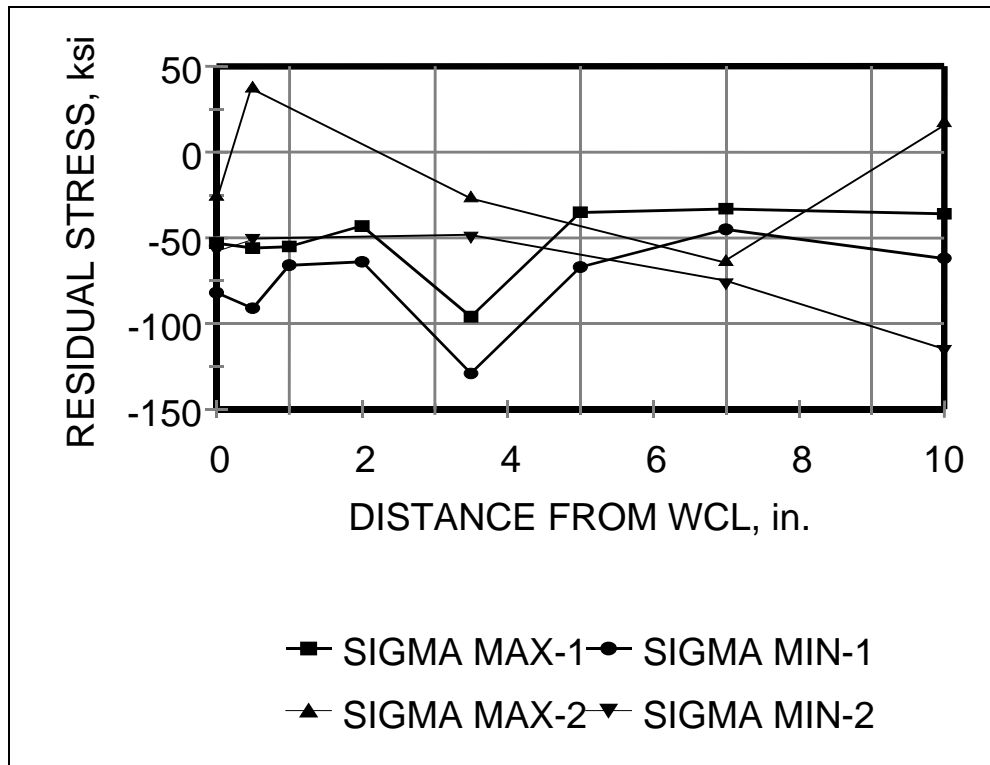


Figure 4.19: Estimated surface residual stress as a function of stress direction, hole drilling set, and distance from the weld centerline. SIGMA MAX-1 = nominal stress parallel to the welding direction for set one readings; SIGMA MAX-2 = nominal stress parallel to the welding direction for set two readings; SIGMA MIN-2 = nominal stress perpendicular to the welding direction for set two readings.

The results in Figure 4.19 show that many of the measured values are above the yield stress of A36 steel (approximately 36 ksi), which is the stress level where plastic deformation around the hole, induced by the presence of high stresses, begins to take place. Thus the magnitude of the measured stresses are suspect simply due to the indicated high stress values.^[74]

A laboratory assessment of the methodology of measurement used to achieve the bridge-specific strain relief values indicates that it was correct. Thus, it is not obvious to the authors why the complete set of hole drilling experimental results are questionable. The most logical reason

would appear to be the degradation of the strain-gage glue. This glue is not recommended for high humidity applications. It turned out that the atmosphere inside the box beams exhibited an unexpectedly high humidity. This, coupled with the fact that the gages were left in a glued-down condition for several days before drilling took place, could well have resulted in glue degradation and subsequent unreliable gage readings.

4.5.4 Conclusions

The above analysis of the residual stress hole-drilling measurements taken on the West Linn Bridge indicates that the results are not credible for the following reasons:

1. The absolute values for all readings are too high;
2. There is little or no agreement between the two sets of data; and
3. The data trends as a function of hole depth are not consistent between sets and contradict model predictions.

5.0 FUTURE WORK

The future work recommendations are presented in three sections. The first covers computer modeling studies. The second covers experimental residual stress measurements. The third covers fracture toughness studies.

5.1 COMPUTER MODELING STUDIES

There are two major complicating factors that stand in the way of confident use of the present FEM work for prediction of the weld-induced residual stress state. One is the lack experimental validation data, and the other is the lack of prediction of the repair weld effects. Development of an accurate computational assessment of expected residual stress state requires both further modeling and experimental studies. The required model-oriented experimental studies will be mentioned in this section but amplified in the section below.

The present major problem with the assessment of the prediction results is that the model only predicts what is to be expected under ideal ESW conditions. It does not take into account the effects of additional repair welds on the resultant residual stress field. Development of a validation base for the present model result would require preparation of laboratory ES welds which are well characterized, both from a welding technique and from a thermal-physical property standpoint. The welds should be as close to the known/predicted West Linn Bridge weldment plate size and weld parameters as possible, in order to make the validated computer model as close to the West Linn Bridge weldment conditions as possible. Detailed residual stress assessment would allow direct comparison with model results, with computational runs based on laboratory weld parameters, leading to model results validation and/or revision until experimental and computational results agree.

The next step would be to perturb both computational and experimental ES weldments with a known series of repair welds based on the experimental observations from this study. Use of this validation base to validate/modify the computational prediction model results would then allow multiple computational ESW plus weld repair scenarios to be assessed with assurance that they would be relevant to the West Linn Bridge ES weldments. It is important to note that the assessment of selected actual West Linn Bridge steel/weld metal constitutive properties would also be required.

5.2 EXPERIMENTAL RESIDUAL STRESS STUDIES

A detailed residual stress data base would need to be developed in order to assess residual stress fields in the West Linn Bridge ES weldments as well as develop a validation data base for the computational modeling mentioned above. This would entail laboratory weld assessment as well as bridge weldment assessment.

The first step would be to fabricate control ES weldments. These weldments would be subjected to residual stress measurements, which would be assessed against model predictions. Note that this assessment would entail two major modeling steps. The first would be computation of expected residual stress fields based on the geometry and mechanical properties of the control ES weldments. Once this was achieved, the geometry of the residual stress assessment specimen(s) could be accounted for in the ESW model. The model would incorporate the slicing operations that are used on the actual material to allow direct comparison with experimental residual strain/stress measurements. Full analysis of expected relief strain measurements would allow assessment of the realism of the computed residual stress distribution.

This same process would then need to be carried out again with the addition of repair welding on laboratory control welds and computational modeling. Validation/modification of the computational modeling would verify and improve the accuracy of the computational results, as well as the measurement/modeling techniques developed for residual stress assessment. This would allow one to develop a residual stress determination technique that could then be used for subsequent additional residual stress assessment specimen removal from the West Linn Bridge weldments and/or re-assessment of the measurement results taken in the present work.

Fabrication of control ES weldments would also allow assessment of the hole-drilling technique under laboratory conditions. Once a repeatable and reliable hole-drilling technique was developed, that agreed with measured and predicted stresses determined by the sectioning technique, multiple hole drilling traverses would be run on West Linn Bridge ES welds. These traverses would be the most economical and least intrusive method for assessing ESW residual stress variability due to changes in ESW and/or repair techniques and material variables.

5.3 FRACTURE TOUGHNESS STUDIES

The major problem with the West Linn Bridge ES weldment fracture toughness assessment was that the comparison of the base metal, fusion zone and HAZ data included uncontrolled variables. The core specimens were removed from widely differing weldment areas, both from a given section and box beam standpoint.

The major difference between a laboratory control weld and a bridge fabrication weld is the control on welding parameter and consumables. Both plates used in the fabrication of a laboratory weld would be from the same well characterized heat of material, unless one purposely wanted to incorporate different heat materials into the analysis. This is not so with a bridge weldment. A given amount of materials to be welded is ordered under a generic specification, and then the materials are used on an as-needed basis. No particular regard is given to heat consistency for a given set of welds and/or a given box beam. It is certainly assumed that multiple heats of material were used in the construction of the West Linn Bridge. This means that the two plates on a given ES weld may come from different heats, and that the weld consumables for different welds may also come from different heats. Consequently, there can be a wide variation in property response from weldment to weldment.

It is hypothesized that this type of problem was responsible for the major discrepancies between impact and fracture toughness properties found in a separate study of the West Linn Bridge weldments.^[75] At room temperature, one does not expect high Charpy V-Notch impact (CVN) properties and very low J-Integral fracture toughness (K/J) properties. The question is, are these results correct for a given weld, and/or are they correct for all welds? An in-depth fracture analysis study is needed to answer these questions. A combination of assessment of control welds and West Linn Bridge welds will be needed to answer these questions.

Control welds made specifically for fracture studies would need to be fabricated. These welds would need to be made from materials and with procedures that accurately represent those used on the West Linn Bridge. Then CVN, K/J and fatigue studies would need to be conducted. This would result in a baseline data set that could be used to assess the response of the variety of Bridge weldments tested. Comparison of the Bridge and baseline data would allow assessment of whether variation within the Bridge weldments have a significant effect on measured properties. An expected outcome of this study would be a methodology to predict toughness properties of the West Linn Bridge ES weldments based on measured chemistry.

Note that the above study only assesses base ESW properties. Another question is what effect on near-surface fusion line properties would one expect from the addition of the repair welds. Previous OGI work in this area for FHWA indicates that toughness properties are increased and fatigue life is not adversely affected, if the repair welds are done properly. It appears some of these repair welds were done using the correct pre-heat requirements while others may not have been. Further repair weld effect studies will need to be carried out to assess the expected change of both pre-heat condition and number of weld passes used for a given repair. Assessment of West Linn Bridge welds by etching and portable hardness measurement would be needed in order to bracket the expected repair scenarios used on the West Linn Bridge ES weldments.

The addition of the cosmetic repair welds is expected to adversely affect the near-surface residual stress distribution. Repair welds done correctly may well increase the near-surface toughness while repair welds improperly applied may decrease the near surface toughness. Prediction of both expected residual stress state and fracture toughness state for specific West Linn Bridge weldments would be the expected outcome of this proposed future work.

6.0 REFERENCES

1. B.E. Paton: Electroslag Welding, American Welding Society, New York, 1962.
2. A.L. Liby and D.L. Olson: Quarterly of the Colorado School of Mines, 1, 1974, p41.
3. J. D. Harrison: " Met. Constr. Br. " Weld. J., 1(8), 1969, p 366.
4. W.P. Beater, Jr., P.J. Konkol, B.M. Kapadia, A.K. Shoemaker, and J.K. Sovak: Acceptance Criteria for Electroslag Weldments in Bridges, Phase I. Final Report, U.S. Steel Corporation. Monroeville, PA, 4, 1977.
5. D. G. Atteridge, S. Venkataraman, and W.E. Wood: Improving the Reliability and Integrity of Consumable Guide Electroslag Weldments in Bridge Structures, Final Report, DOT-FHWA, December 1982.
6. D.G. Atteridge, S. Venkataraman, and W.E. Wood: Improving the Reliability and Integrity of Consumable Guide electroslag Weldments in Bridge Structures, Executive Summary Report, DOT-FHWA, December 1982.
7. D.G. Atteridge, W.E. Anderson et al, Department of Energy, Westinghouse Savannah River Company, Aiken, SC: Weld Residual Stress Measurement/ Mitigation, Annual Progress Report October 1, 1991 through September 30, 1992, Subcontract No. AA46386, report No. 17, July 1993.
8. D. G. Atteridge, J.H. Devletian, and W.E. Wood: Heat-Affected Zone Toughness of Electroslag Weldments, Office of Advanced Research, Federal Highway Administration, U.S. Department of Transportation, Grant No. DTFH61-86-X-00119, March 1994.
9. R. Turpin, D.G. Atteridge, J.H. Devletian, and W.E. Wood: Repair of Process-Related Defects in Electroslag Weldments, Office of Advanced Research, Federal Highway Administration, U.S. Department of Transportation, Grant No. DTFH61-86-X-00119, March 1994.
10. D.G. Atteridge, R.E. Page, V. Srivathsan and W. Wood: "Effect of Mechanical Vibration on Electroslag Weldment Fusion Zone Structure", the 61st Annual American Welding Society Meeting, Los Angles, CA, April 1980.
11. S. Venkataraman, W.E. Wood, D.G. Atteridge, and J.H. Devletian: "Influence of Alloy Additions on the Toughness of Electroslag Weld Metal", the ASM Metals Congress, Cincinnati, OH, September 21-23, 1981.
12. S. Venkataraman, W.E. Wood, D.G. Atteridge, and J.H. Devletian: "A New Method for Grain Refinement in Electroslag Welds", the ASM Conference, Trends in Welding Research in the United States, New Orleans, LA, November 16-18, 1981.
13. J.H. Devletian, P. Wang, W.E. Wood, and D.G. Atteridge: "Toughness and Structure Changes in ES Welds Induced by SA Overwelding", the Annual American Welding Society Meeting, Kansas City, MO, April 26-29, 1982.
14. S. Venkataraman, W.E. Wood, and D.G. Atteridge: "Influence of Process Variables on Microstructures and mechanical properties of Electroslag Welds", the 63rd Annual American Welding Society Meeting, Kansas City, MO, April 26-29, 1982.

15. S. Venkataraman, W.E. Wood, D.G. Atteridge, and J.H. Devletian: "Influence of Alloy Additions on the Toughness of Electrosag Weld Metal", the 63rd Annual American Welding Society Meeting, Kansas City, MO, April 26-29, 1982.
16. S. Venkataraman, J.H. Devletian, W.E. Wood, and D.G. Atteridge: "Grain Refinement Dependence on Solidification and Solid State Reaction in Electrosag Welds", the TMS/AIME Fall Meeting, St. Louis, MO, October 25-26, 1982.
17. W.E. Wood, D.G. Atteridge, and W.E. Anderson: "Acoustic Emission Characterization of Defects in Electrosag Weldments", the International Conference on Trends in Welding Research, Gatlinburg, TN, May 1986.
18. D.G. Atteridge and W.E. Anderson: "Cyclic Work Hardening Induced in the Heat-Affected Zone During Multi-Pass Welding", the Third International Conference on Welding and Performance of Pipelines, London, England, November 1986.
19. Khalid Khan, John Albers, David Atteridge, Lemmy Meekisho, and Daniel Danks: "An Experimental Study of Residual Stresses in Mechanical Components", the 1992 SEM Congress, Las Vegas, Nevada, June 8-11, 1992.
20. D.G. Atteridge, J. Devletian, R. Turpin, and W.E. Wood: "Electrosag Welding of Thick Section Steel Plates", Materials Week, Chicago, IL, October 1994.
21. S. Venkataraman, W.E. Wood, J.H. Devletian, and D.G. Atteridge: "Grain Refinement in Electrosag Welds", Recent Trends in Welding Research in the United States, ASM, 1982.
22. S. Venkataraman, J.H. Devletian, W.E. Wood, and D.G. Atteridge: "Grain Refinement Dependence on Solidification and Solid State Reactions in electrosag welds", Grain Refinement in Castings and Welds, TMS-AIME, 1983.
23. M.R. Scholl, W.E. Wood, and D.G. Atteridge: "Acoustic Emission Characterization of Defects in Electrosag Weldments ", 29th International Instrumentation Symposium Proceedings, Las Vegas, Nevada, May 1982.
24. M. Li, D.G. Atteridge, L.L. Meekisho and V.A. Dikshit: "Finite Element Analysis of Multipass Electrosag Cladding Welds ", the 74th Annual AWS Convention, Houston, TX, April 27-30, 1993.
25. M. Li, D.G. Atteridge, V.A. Dikshit and L.L. Meekisho: "Finite Element Analysis of Electrosag Cladding", International Conference on Modeling and Control of Joining Processes, Orlando, FL, December 8-10, 1993.
26. M. Li, D.G. Atteridge, and L.L. Meekisho: "Mathematical Modeling of Microstructure Evolution in Heat Effected Zone of Electrosag Cladding", International Conference on Trends in Welding Research, Gatlinburg, TN, June 1995.
27. S. Venkataraman: Effects of Process Variables and Microstructures on Properties of Electrosag Weldments, Ph.D. Thesis, O.G.I., 1981.
28. A.W. Pense, J.D. Wood, J.W. Fisher: "Recent Experiences with Electrosag Welded Bridges", Welding Journal, 12, p 33-42.
29. K. Masubuchi: Analysis of Welded Structure, New York, NY, Pergamon Press, 1981.
30. H. Wohlfahrt: "Residual Stresses due to Welding, Their Origin, Calculation and Evaluation", Residual Stresses, edited by E. Macherlauch, V. Alle Rechte Vorbehalten Hauk., Germany, DGM Informationsgesellschaft mbH, 1986, p 81-112.
31. Metals Handbook, volume 6: Welding, Brazing, and Soldering, Ed. 10, Materials Park, Ohio: ASM International, 1992.

32. C.O. Ruud: Review and Evaluation of Nondestructive Methods for Residual Stress Measurement, Sep. 1981.
33. Koichi Masubuchi: "Models of Stresses and Deformation due to Welding-A Review", Modeling of Casting and Welding Processes, the Metallurgical Society of AIME, Aug. 3-8, 1980, p 223.
34. L. Tall: "Residual Stresses in Welded Plates-A Theoretical Study", Welding Journal Research Supplement, 43 (1), 1964, p 105-235.
35. K. Masubuchi, B. Simmons, and R.E. Monre: Analysis of Thermal Stresses and Metal Movement During Welding, RSIC-820, Redstone Scientific Information Center, Redstone Arsenal, Alabama, July, 1968.
36. M. Hetenyi: Handbook of Experimental Stress Analysis, New York, NY, John Wiley & Sons, 1950.
37. J. Mathar: "Determination of Initial Stresses by Measuring the Deformations Around Drilled Holes", Trans. ASME, 56 (4), 1934, p 249-254.
38. Standard Test Method for Determining Residual Stresses by the Hole-Drilling Strain-Gauge Method, ASTM Standard E 837-95.
39. N.J. Rendler and I. Vigness: "Hole-Drilling Strain-Gauge Method of Measuring Residual Stress", Experimental Mechanics, 6(12), 1966, p 577-586.
40. H. Wolf and D.L. Sauer: "New Experimental Techniques to Determine Residual Stresses in Large Turbine-Generator Compounds", American Power Conf., Chicago, May 1, 1974.
41. A. J. Bush and F. J. Kromer: "Residual Stresses in a shaft after Weld Repair and Subsequent Stress Relief", 1979 SESA Spring Meeting, Soc. for Exp. Stress Anal., 21 Bridge Square, Westport, CT, paper No. A-16.
42. D. Rosenthal: "Mathematical Theory of Heat Distribution During Welding and Cutting", Welding Journal, 20 (5), 1941, p 220s-234s.
43. D. Rosenthal: "The Theory of Moving Sources of Heat and Its Application to Metal Treatment", Trans. ASME, 68 (11), 1946, p 849-865.
44. D. Radaj: Heat Effects of Welding - Temperature Field Residual Stress Distribution, Springer - Verlag, 1992.
45. E.F. Nippes, L.L. Merrill and W.F. Savage: Welding Journal Research Supplement, 28, 1949, p 556s - 564s.
46. E.F. Nippes, H. Wawrousek and W.L. Fleischmann: Welding Journal Research Supplement, 34, 1955, p 169s - 196s.
47. Jr. C.M. Adams: Welding Journal Research Supplement, 37, 1958, P 210s - 215s
48. D.E. Rodgers and P.R. Fletcher: "The Determination of Internal Stresses from the Temperature History of a Butt Welded Pipe", Welding Journal Research Supplement, 1938, p 4s - 7s.
49. S. Vaidyanathan, A.F. Todaro and I. Finne: "Residual Stresses Due to Circumferential Welds", ASME Journal of Engineering Materials and Technology, Oct. 1973, p. 233 - 237
50. Z. Paley, L. Lynch and C. Adams: "Heat Flow in Welding Heavy Steel Plate", Welding Journal Research Supplement, Feb. 1964, p 71s - 79s.
51. C. M. Adams: "Cooling Rates and Peak Temperatures in Fusion Welding", Welding Journal Research Supplement, May 1958, p210s - 215s.

52. Y. Veda and T. Amici: "Analysis of Thermal Elastic-Plastic Stress and Strain During Welding by Finite Element Method", *Trans. Japan Welding Society*, 2 (2), 1971, p 90 - 100.
53. E. Wilson and R. Nickell: "Application of the Finite element Analysis to Heat Conduction Problems", *Nuclear Engineering and Design*, No. 4, 1966, p 276 - 286.
54. J. Goldak, M.J. Bibby, D. Downey and M. Gu: "Heat and Fluid Flow in Welds", *Advanced Joining Technologies*, edited by T.H. North, London, UK: Chapman and Hall, 1990, p 69 - 82 .
55. W. K. C. Johnes and P.J. Alberry: "A Model for Stress Accumulation in Steels during Welding", *Residual Stresses in Welds by Welded Construction and Their Effects*, edited by R.W. Nichols, London, UK, Nov. 1978, p 15 - 17.
56. G. W. Greenwood and R. H. Johnson: "The Deformation of Metals under Small Stresses during Phase Transformations", *Proceedings Royal Society*, A283 (1394), Jan. 1965, p 403 - 422.
57. S. H. Cho and J.E. Sunderland: "Phase Change Problems with Phase Change Thermal Conductivity", *Trans. ASME*, 96 (5), p 214 - 217.
58. A.H. Dilawari, J. Szekely, and T.W. Eagar: "Electromagnetically and Thermally Driven Flow Phenomena in Electroslag Welding", *Metall. Trans. B*, 9 B, 1978, p 371-381.
59. A.H. Dilawari, T.W. Eagar and J. Szekely: "An Analysis of Heat and Fluid Flow Phenomena in Electroslag Welding", *Welding Journal*, Jan. 1978, p s - 30s.
60. T. Debroy, J. Szekely, and T.W. Eagar, "Heat Generation Patterns and Temperature Profiles in Electroslag Welding," *Metallurgical Transactions*, 11B (12), 1980, p 593-605.
61. T. Debroy, J. Szekely, and T.W. Eagar, "Temperature Profiles, the Size of the Heat-Affected Zone and Dilution in Electroslag Welding," *Materials Science and Engineering*, 56, 1982, p 181-193.
62. ANSYS 5.0 Engineering Analysis System, Swanson Analysis System, Inc., 1992.
63. L. Zhang, "Experimental and Finite Element Analysis of Residual Stress in electroslag Butt Welds", Ph.D. Thesis, Oregon Graduate Institute, Portland, Oregon, June 1999.
64. X. Chen, M. Becker and L. Meekisho, "Welding Analysis in Moving Coordinates," *Math. Analysis of Weld Phenomena IV*, H. Cerjak (ed.), The Institute of Materials, London, UK 1997.
65. X. Chen, M. Becker and L. Meekisho, "Finite Element Analysis in Moving Coordinates," p. 91, *Proc. 2997 National Heat Transfer Conf.*, ASME Pub. HTD-348 (1997).
66. D. Radaj: *Heat Effects of Welding*, Springer-Verlag, Berlin, 1992.
67. J. Bergheau and J.B. Leblond: "Coupling between Heat Flow, Metallurgy and Stress-Strain Computations in Steel: The Approach Developed in the Computer Code SYSWELD for Welding and Quenching", *Modeling of Casting, Welding, and Advanced Solidification Processes V*, The Minerals Metals and Materials Society, Warrendale, Pa, 1991.
68. SYSWELD+ Reference Manual, private information.
69. J. A. Goldak and M. Gu: "Computational Weld Mechanics of the Steady State", *Mathematical Modeling of Weld Phenomena 2*, Institute of Materials, London, UK, 1995
70. M. Gu, J.A. Goldak and E. Hughes: "Steady State Thermal Analysis of Welds with Filler Addition", *Can. Metall.*, 32, 1993, p49-55.
71. M. Gu, J.A. Goldak: "Steady State Formulation for Stress and Distortion of Welds", *ASMEJ PED-64*, p843-854.

72. D.G. Atteridge, M. Becker, L. Meekisho, K. Nelson-Owusu, B. Tahmasebi, and L. Zhang, "3D Eulerian Modeling of Electroslag Welding," *Trends in Welding Research*, ASM International Conference, June 1999, p. 943-948.
73. Steven C. Lovejoy, "Bridge Engineering Section, Oregon Dept. of Transportation, Private Communication.
74. Measurement of Residual Stresses by the Hole Drilling Strain Gauge Method, Tech Note TN-503-3, Measurements Group, Inc., Raleigh, NC.
75. J.H. Devletian, "Toughness and Fatigue Threshold Determination of Electroslag Welds Extracted from the West Linn Bridge," Final Report submitted to the Oregon Dept. of Transportation by the Oregon Graduate Institute, 1999.

APPENDICES

APPENDIX A: CORE-RELATED RELIEF STRAIN RESULTS

Table A-1: Core-related calculated relief strains and stresses for weld centerline core B3B1.

Coring or slicing	Calculated Strain, ue	Relief Stress, ksi	Distance from bottom surface, in.	Degrees from Gage 1
Coring				
Par-90	-1163	-30.8		
Per-90	762.4	13.6		
Cut 1			1.2	
Par-90	24	1.8		
Per-90	-84	-4.3		
Par-45	-206	-12.3		-81
Per-45	-562	-20.6		
Cut 2			2.3	
Par-90	106	1.9		
Per-90	-162	4.3		

Gage 1 was perpendicular to the welding direction.

Table A-2: Core-related calculated relief strains and stresses for weld centerline core C7B2.

Coring or slicing	Calculated Strain, ue	Relief Stress, ksi	Distance from bottom surface, in.	Degrees from Gage 1
Coring				
Par-90	-1013.3	-26.7		
Per-90	678.3	12.3		
Cut 1			1.0	
Par-90	21	-0.2		
Per-90	-89	-2.7		
Par-45	4	-3.6		-87
Per-45	-374	-12.3		
Cut 2			2.2	
Par-90	74	-1.8		
Par-90	-432	-13.5		
Cut 3			0.2	
Par-45	-159	-13.0		83
Per-45	-777	-27.2		
Cut 4			2.8	
Par-90	816	20.7		
Per-90	-627	-12.6		

Gage 1 was perpendicular to the welding direction.

Table A-3: Core-related calculated relief strains and stresses for weld centerline core C3B2.

Coring or slicing	Calculated Strain, ue	Relief Stress, ksi	Distance from bottom surface, in.	Degrees from Gage 1
Coring				
Par-90	NA	(-30.6)		
Per-90	NA	(9.4)		
Cut 1			1.2	
Par-90	29	-0.4		
Per-90	-53	-1.5		
Par-45	-10	-2.9		55
Per-45	-258	-8.6		
Cut 2			2.3	
Par-90	49.4	-0.5		
Per-90	-215	-6.6		

Gage 1 was parallel to the welding direction. () = Assumed coring-induced relief stress.

Table A-4: Core-related calculated relief strains and stresses for weld centerline core D3B1.

Coring or slicing	Calculated Strain, ue	Relief Stress, ksi	Distance from bottom surface, in.	Degrees from Gage 1
Coring				
Par-90	-1062.9	-30.4		
Per-90	473	5.1		
Cut 1			1.2	
Par-90	23	-0.2		
Per-90	-97	-3.0		
Par-45	-12	-2.8		88
Per-45	-240	-8.0		
Cut 2			2.3	
Par-90	100	0.4		
Per-90	-373	-11.3		

Gage 1 was perpendicular to the welding direction.

Table A-5: Core-related calculated relief strains and stresses for heat affected zone core B3B2.

Coring or slicing	Calculated Strain, ue	Relief Stress, ksi	Distance from bottom surface, in.	Degrees from Gage 1
Coring				
Par-90	-1156.5	-29.0		
Per-90	924.5	19.0		
Cut 1			2.4	
Par-90	128	3.0		
Per-90	-123	-2.8		
Par-45	32	0.5		42
Per-45	-55	-1.5		
Cut 2			1.2	
Par-45	134	2.1		44
Par-45	-236	-6.5		
Cut 3			0.2	
Par-45	116	2.0		48
Per-45	-183	-4.9		

Gage 1 was 45 degrees to the welding direction.

Table A-6: Core-related calculated relief strains and stresses for heat affected zone core B7B1.

Coring or slicing	Calculated Strain, ue	Relief Stress, ksi	Distance from bottom surface, in.	Degrees from Gage 1
Coring				
Par-90	-642.9	-12.6		
Per-90	864.1	22.1		
Cut 1			1.2	
Par-90	38	-0.7		
Per-90	-59	-1.6		
Par-45	-27	-2.5		39
Per-45	-337	-10.8		
Cut 2			2.4	
Par-90	81	3.1		
Per-90	45	2.3		
Cut 3			2.9	
Par-90	115	4.3		
Per-90	48	2.7		

Gage 1 was 45 degrees to the welding direction.

Table A-7: Core-related calculated relief strains and stresses for heat affected zone core B7B2.

Coring or slicing	Calculated Strain, ue	Relief Stress, ksi	Distance from bottom surface, in.	Degrees from Gage 1
Coring				
Par-90	-862.6	-21.7		
Per-90	683.4	14.0		
Cut 1			1.2	
Par-90	43	0.4		
Per-90	-97	-2.8		
Par-45	118	3.2		39
Per-45	-70	-1.1		
Cut 2			2.4	
Par-90	108	-0.7		
Per-90	-293	-8.6		
Cut 3			2.9	
Par-90	76	-3.4		
Per-90	-601	-19.1		

Gage 1 was 45 degrees to the welding direction.

Table A-8: Core-related calculated relief strains and stresses for heat affected zone core C3B1.

Coring or slicing	Calculated Strain, ue	Relief Stress, ksi	Distance from bottom surface, in.	Degrees from Gage 1
Coring				
Par-90	NA	(-29)		
Per-90	NA	(-19)		
Cut 1			2.4	
Par-90	58	0.5		
Per-90	-144	-4.2		
Par-45	45	-1.7		44
Per-45	-64	-1.7		
Cut 2			1.2	
Par-45	-28	-52		44
Per-45	-428	-14.4		
Cut 3			0.2	
Par-45	-198	-13.7		41
Per-45	-727	-25.9		

Gage 1 was 45 degrees to the welding direction.

Table A-9: Core-related calculated relief strains and stresses for heat affected zone core C7B1.

Coring or slicing	Calculated Strain, ue	Relief Stress, ksi	Distance from bottom surface, in.	Degrees from Gage 1
Coring				
Par-90	-532.2	-7.9		
Per-90	978.7	27.0		
Cut 1			1.2	
Par-90	30	0.8		
Per-90	-20	-0.4		
Par-45	28	-0.8		39
Per-45	-169	-5.3		
Cut 2			2.4	
Par-90	62	2.1		
Per-90	9	0.9		
Cut 3			2.9	
Par-90	-41	-2.9		
Per-90	-158	-5.6		

Gage 1 was 45 degrees to the welding direction.

Table A-10: Core-related calculated relief strains and stresses for heat affected zone core D3B2.

Coring or slicing	Calculated Strain, ue	Relief Stress, ksi	Distance from bottom surface, in.	Degrees from Gage 1
Coring				
Par-90	-894.3	-20.6		
Per-90	-894.2	+20.6		
Cut 1			1.7	
Par-90	84	1.2		
Per-90	-154	-4.2		
Par-45	67	0.2		87
Per-45	-201	-5.9		
Cut 2			2.2	
Par-90	516	14.4		
Par-90	-263	-3.6		
Cut 3			1.3	
Par-45	39	-2.3		87
Per-45	-359	-11.5		
Cut 4			2.6	
Par-90	20	-3.4		
Per-90	-409	-13.3		
Cut 5			0.9	
Par-45	-16	-7.4		89
Per-45	-695	-23.1		
Cut 6			3.0	
Par-90	48	-3.5		
Per-90	-517	-16.6		
Cut 7			0.4	
Par-45	-58	-11.0		-88
Per-45	-920	-30.1		

Gage 1 was parallel to the welding direction.

Table A-11: Core-related calculated relief strains and stresses for heat affected zone core D7B1.

Coring or slicing	Calculated Strain, ue	Relief Stress, ksi	Distance from bottom surface, in.	Degrees from Gage 1
Coring				
Par-90	-681.7	-13.5		
Per-90	902.7	23.0		
Cut 1			1.2	
Par-90	-6	-0.4		
Per-90	-17	-0.6		
Par-45	94	2.7		71
Per-45	-39	-0.3		
Cut 2			2.4	
Par-90	-31	-1.3		
Per-90	-26	-1.2		
Cut 3			2.9	
Par-90	-130	-4.4		
Per-90	-11	-1.7		

Gage 1 was 45 degrees to the welding direction.

Table A-12: Core-related calculated relief strains and stresses for 2.5 in. thick base metal core B1+4.

Coring or slicing	Calculated Strain, ue	Relief Stress, ksi	Distance from bottom surface, in.	Degrees from Gage 1
Coring				
Par-90	442	16.3		
Per-90	179.5	10.3		
Cut 1			0.4	
Par-90	19	1.0		
Per-90	32	1.3		
Par-45	70	2.1		44
Per-45	-25	-0.1		
Cut 2			0.8	
Par-90	30	1.4		
Per-90	39	1.6		
Cut 3			1.0	
Par-90	-15	-0.4		
Per-90	6	0.1		

Gage 1 was 45 degrees to the welding direction.

Table A-13: Core-related calculated relief strains and stresses for 3.5 in. thick base metal core D3B1+8.

Coring or slicing	Calculated Strain, ue	Relief Stress, ksi	Distance from bottom surface, in.	Degrees from Gage 1
Coring				
Per-90	769.1	25.6		
Par-90	20.6	8.3		
Cut 1			1.8	
Per-90	3	0.9		
Par-90	79	2.6		
Per-45	97	1.8		-26
Par-45	-141	-3.7		
Cut 2			2.2	
Per-90	72	3.7		
Par-90	138	5.3		
Cut 3			1.3	
Per-45	154	2.2		-27
Par-45	-292	-8.1		
Cut 4			2.7	
Per-90	117	5.9		
Par-90	204	7.9		
Cut 5			0.9	
Per-45	246	4.3		-26
Par-45	-384	-10.2		
Cut 6			3.0	
Per-90	48	-3.5		
Par-90	-517	-16.6		
Cut 7			0.5	
Per-45	369	7.7		-25
Par-45	-455	-11.3		

Gage 1 was 45 degrees to the welding direction.

**APPENDIX B: GRAPHS OF CORE-RELATED RELIEF STRAIN
RESULTS**

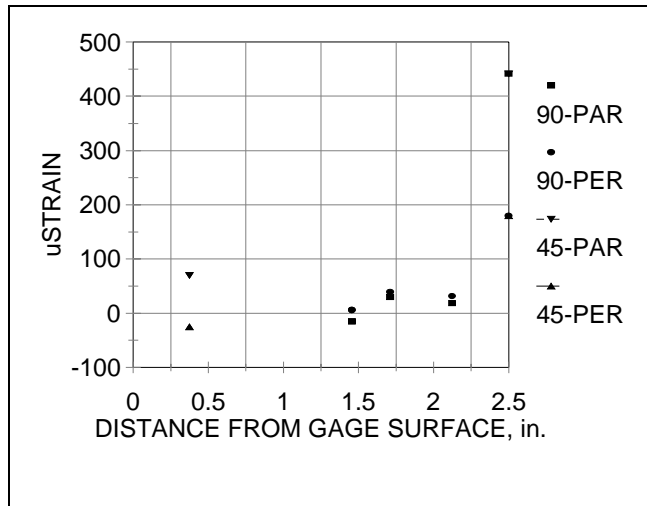


Figure B-1: Measured strain relieved during coring and sectioning for the 2.5 in. thick base metal core B1+4. PAR = parallel; PER = perpendicular; 90 = 90° two-gage strain rosette; 45 = 45° three-gage strain rosette

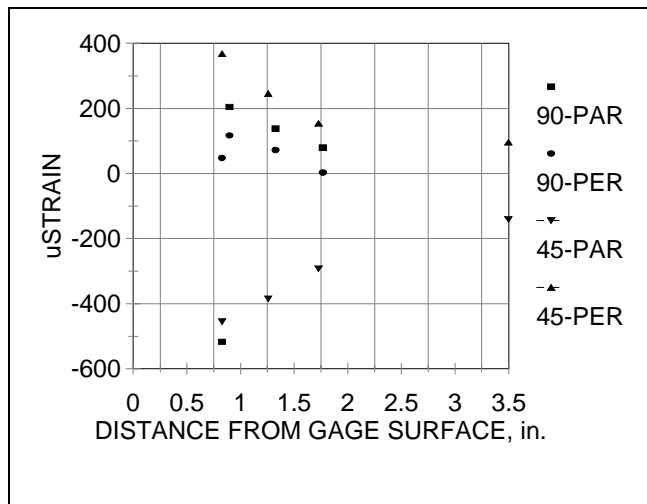


Figure B-2: Measured strain relieved during coring and sectioning for the 3.5 in. thick base metal core D3B1+8. PAR = parallel; PER = perpendicular; 90 = 90° two-gage strain rosette; 45 = 45° three-gage strain rosette

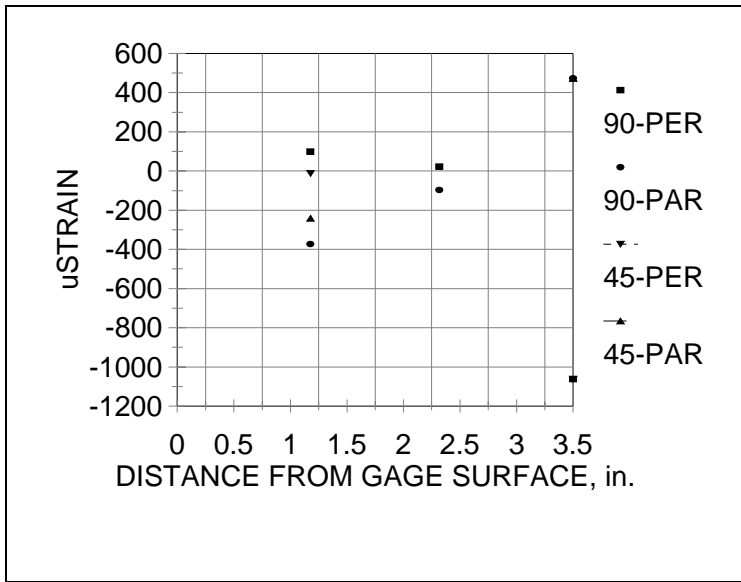


Figure B-3: Measured strain relieved during coring and sectioning for the weld centerline core D3B1. PAR = parallel; PER = perpendicular; 90 = 90° two-gage strain rosette; 45 = 45° three-gage strain rosette.

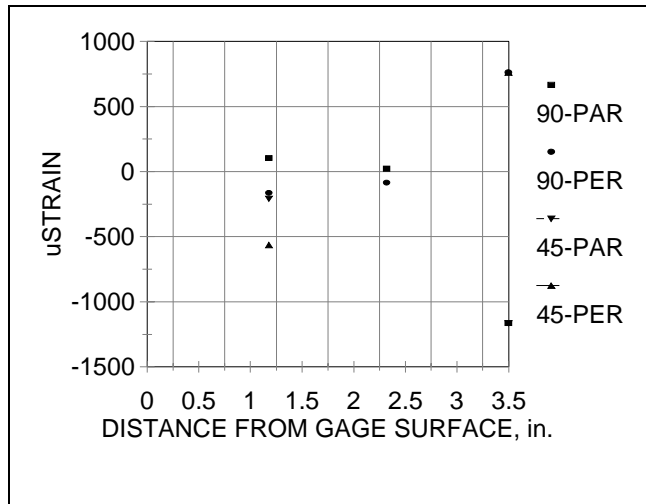


Figure B-4: Measured strain relieved during coring and sectioning for the weld centerline core B3B1. PAR = parallel; PER = perpendicular; 90 = 90° two-gage strain rosette; 45 = 45° three-gage strain rosette.

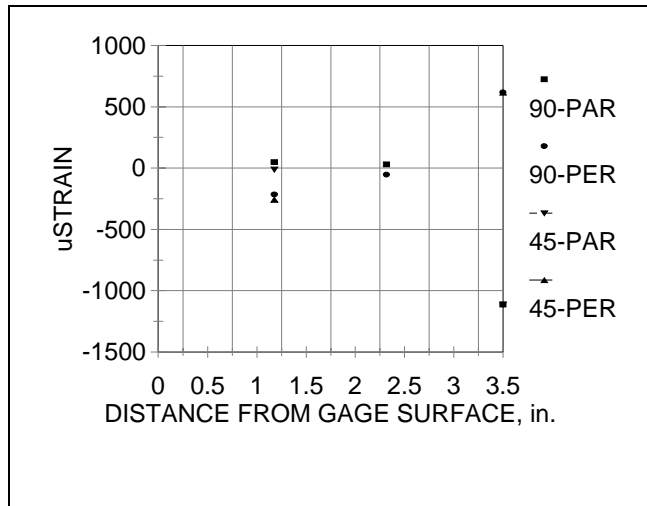


Figure B-5: Measured strain relieved during coring and sectioning for the weld centerline core C3B2. PAR = parallel; PER = perpendicular; 90 = 90° two-gage strain rosette; 45 = 45° three-gage strain rosette.

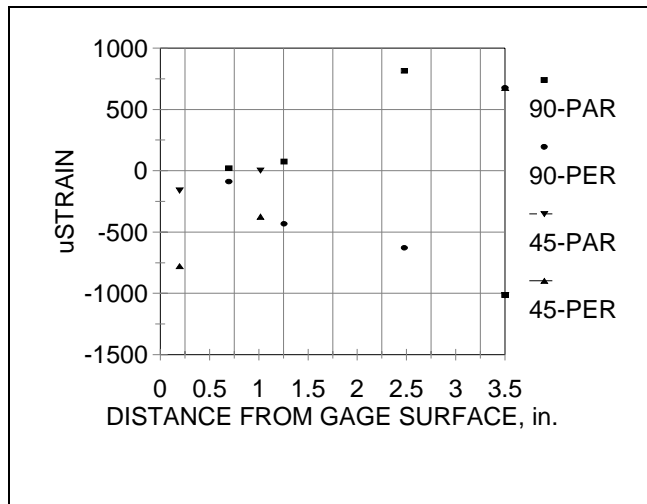


Figure B-6: Measured strain relieved during coring and sectioning for the weld centerline core C7B2. PAR = parallel; PER = perpendicular; 90 = 90° two-gage strain rosette; 45 = 45° three-gage strain rosette.

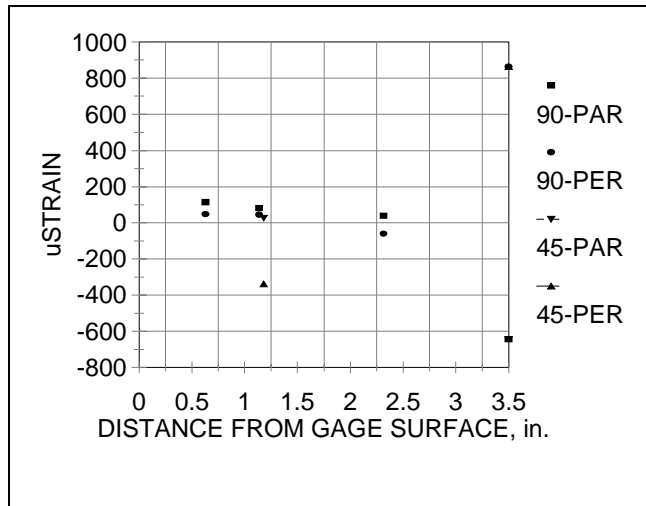


Figure B-7: Measured strain relieved during coring and sectioning for the heat affected zone core B7B1. PAR = parallel; PER = perpendicular; 90 = 90° two-gage strain rosette; 45 = 45° three-gage strain rosette.

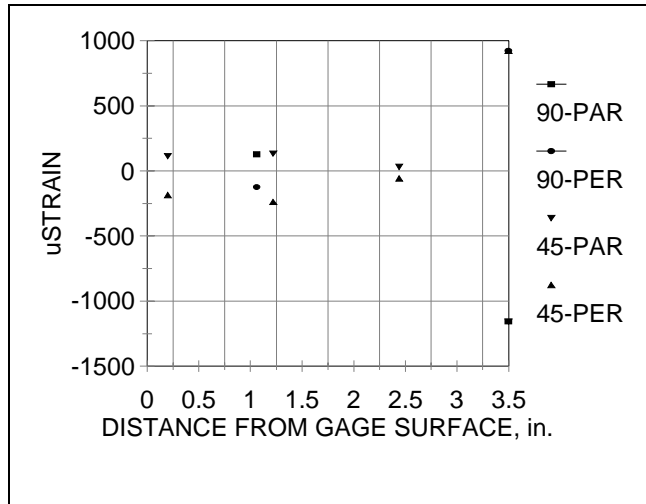


Figure B-8: Measured strain relieved during coring and sectioning for the heat affected zone core B3B2. PAR = parallel; PER = perpendicular; 90 = 90° two-gage strain rosette; 45 = 45° three-gage strain rosette.

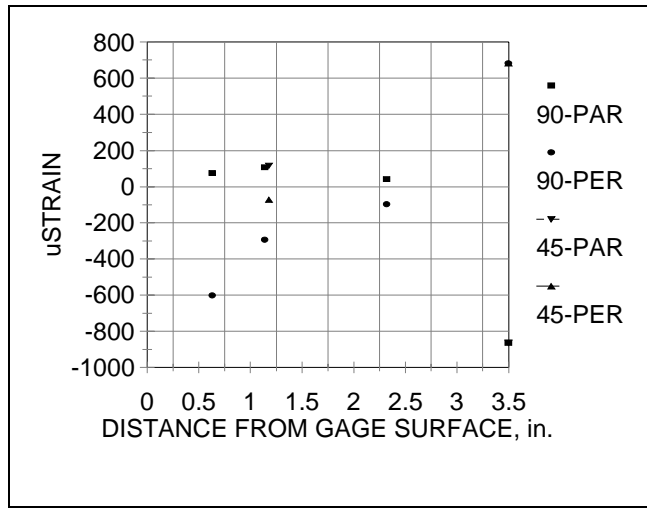


Figure B-9: Measured strain relieved during coring and sectioning for the heat affected zone core B7B2. PAR = parallel; PER = perpendicular; 90 = 90° two-gage strain rosette; 45 = 45° three-gage strain rosette.

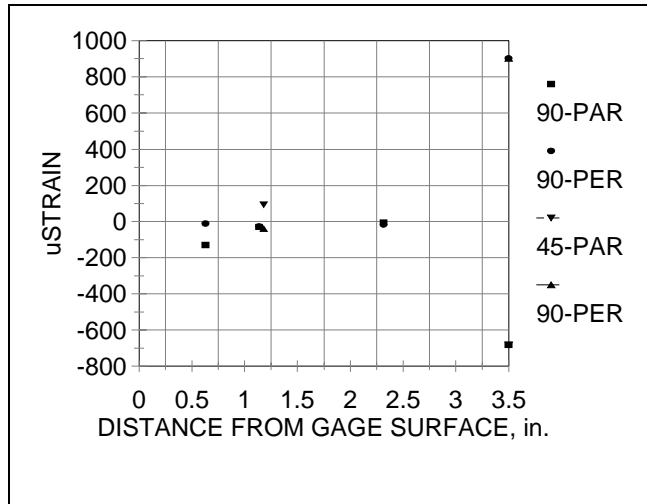


Figure B-10: Measured strain relieved during coring and sectioning for the heat affected zone core D7B1. PAR = parallel; PER = perpendicular; 90 = 90° two-gage strain rosette; 45 = 45° three-gage strain rosette.

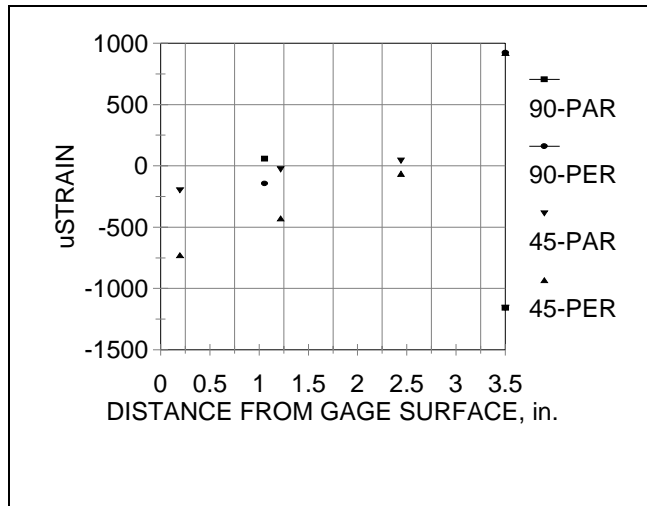


Figure B-11: Measured strain relieved during coring and sectioning for the heat affected zone core C3B1. PAR = parallel; PER = perpendicular; 90 = 90° two-gage strain rosette; 45 = 45° three-gage strain rosette.

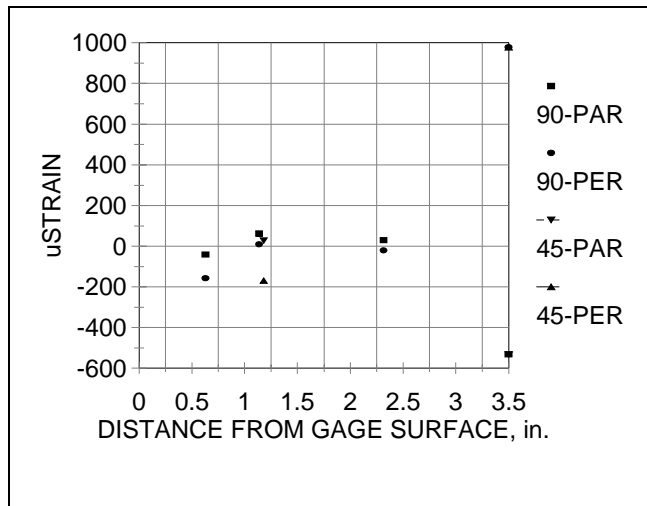


Figure B-12: Measured strain relieved during coring and sectioning for the heat affected zone core C7B1. PAR = parallel; PER = perpendicular; 90 = 90° two-gage strain rosette; 45 = 45° three-gage strain rosette.

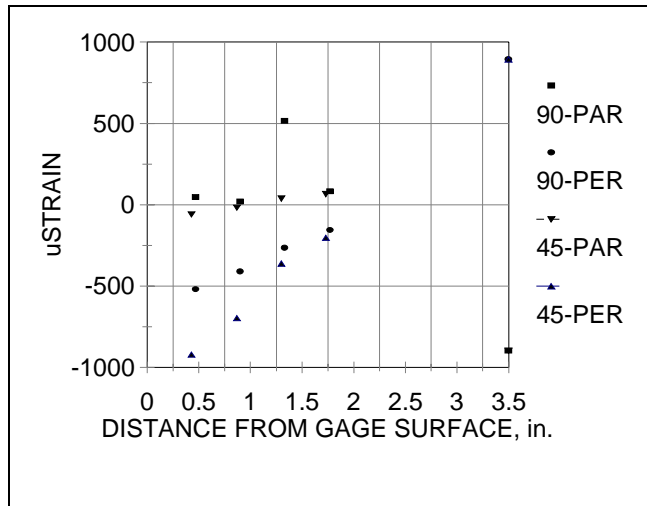


Figure B-13: Measured strain relieved during coring and sectioning for the heat affected zone core D3B2. PAR = parallel; PER = perpendicular; 90 = 90° two-gage strain rosette; 45 = 45° three-gage strain rosette.

APPENDIX C: BRIDGE-RELATED RESIDUAL STRESSES

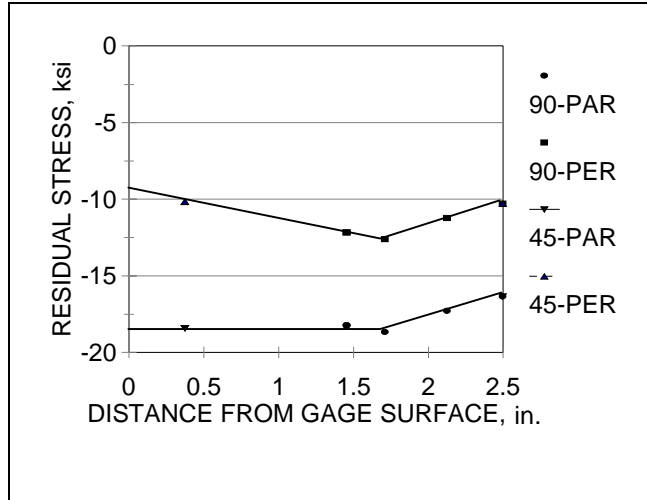


Figure C-1: Calculated residual stress for base metal core B1+4. PAR = parallel; PER = perpendicular; 90 = 90° two-gage strain rosette; 45 = 45° three-gage strain rosette

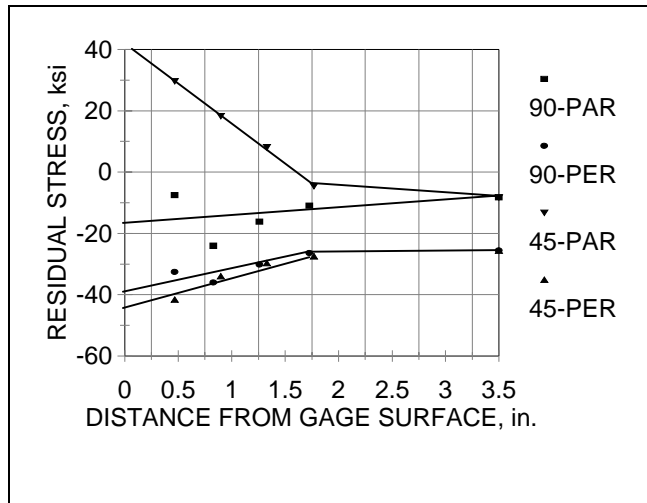


Figure C-2: Calculated residual stress for core D3B1+8. PAR = parallel; PER = perpendicular; 90 = 90° two-gage strain rosette; 45 = 45° three-gage strain rosette

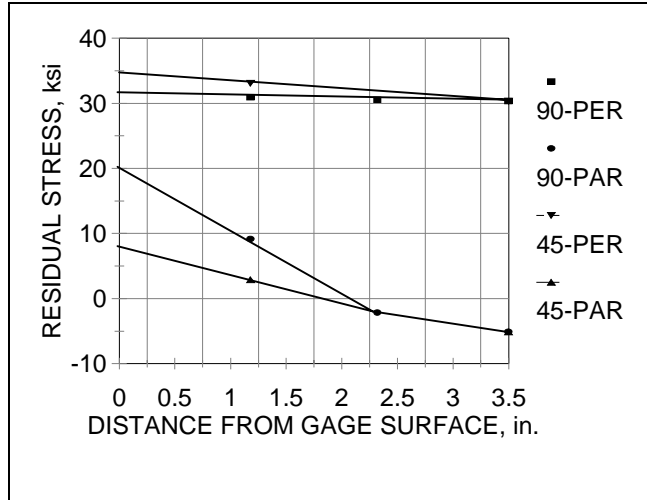


Figure C-3: Calculated residual stress for the weld centerline core D3B1. PAR = parallel; PER = perpendicular; 90 = 90° two-gage strain rosette; 45 = 45° three-gage strain rosette.

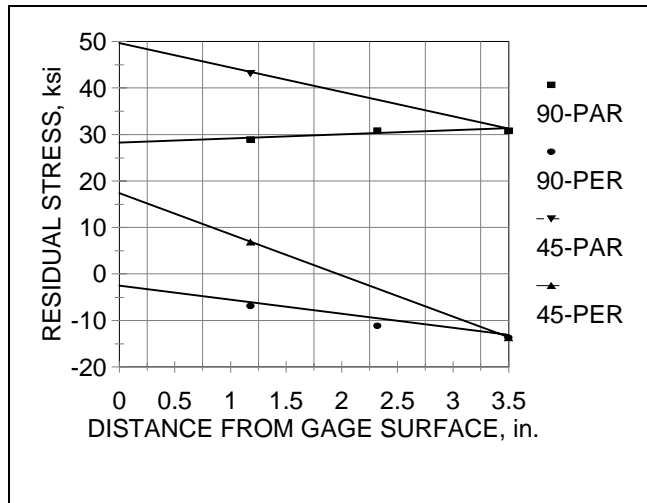


Figure C-4: Calculated residual stress for the weld centerline core B3B1. PAR = parallel; PER = perpendicular; 90 = 90° two-gage strain rosette; 45 = 45° three-gage strain rosette.

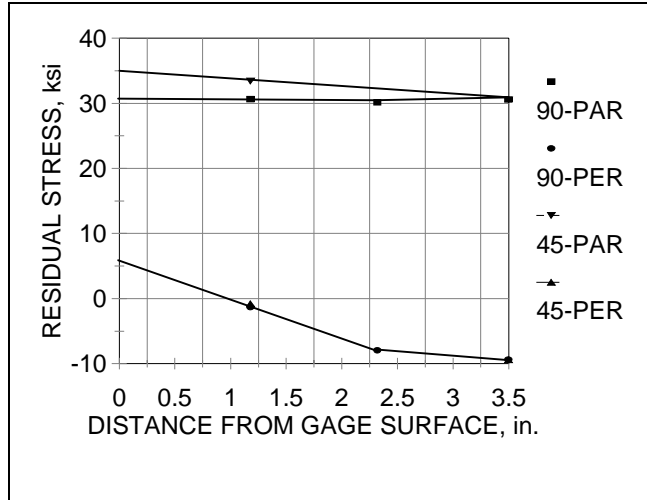


Figure C-5: Calculated residual stress for the weld centerline core C3B2. PAR = parallel; PER = perpendicular; 90 = 90° two-gage strain rosette; 45 = 45° three-gage strain rosette.

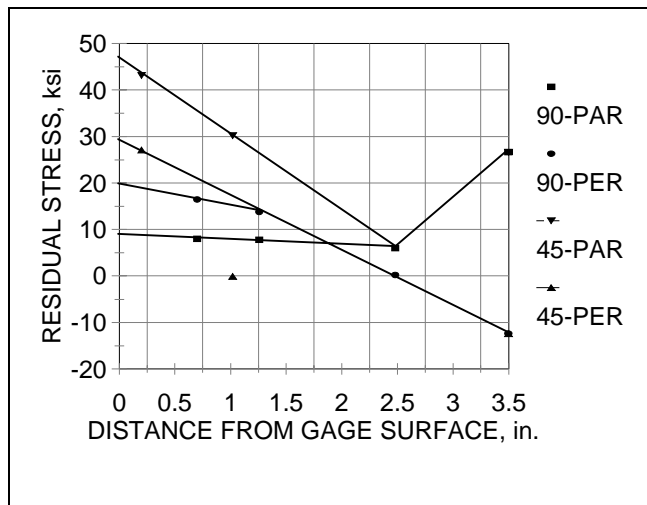


Figure C-6: Calculated residual stress for the weld centerline core C7B2. PAR = parallel; PER = perpendicular; 90 = 90° two-gage strain rosette; 45 = 45° three-gage strain rosette.

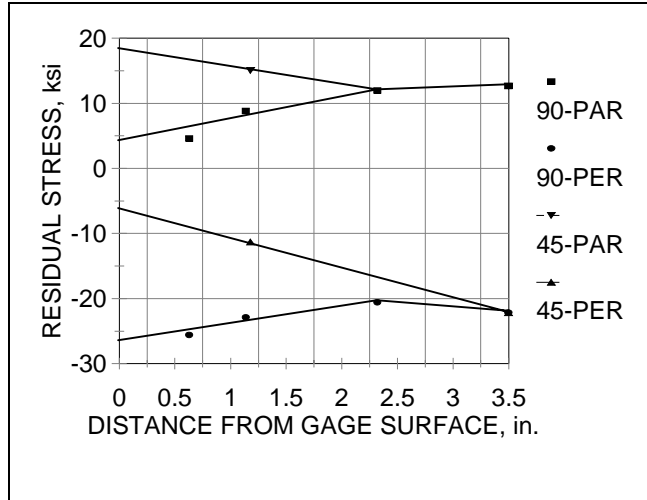


Figure C-7: Calculated residual stress for the heat affected zone core B7B1. PAR = parallel; PER = perpendicular; 90 = 90° two-gage strain rosette; 45 = 45° three-gage strain rosette.

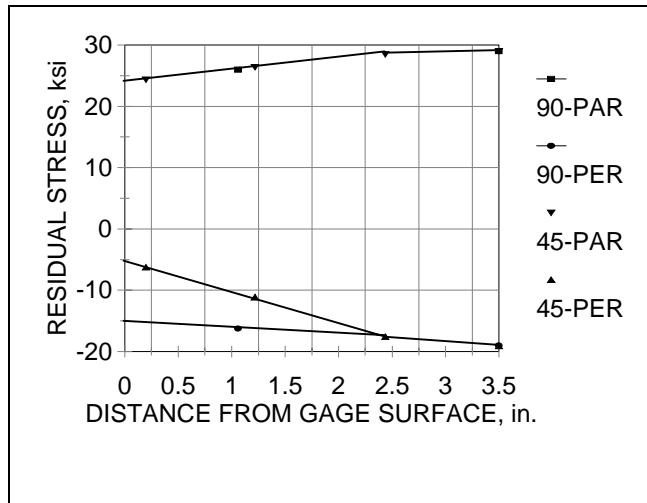


Figure C-8: Calculated residual stress for the heat affected zone core B3B2. PAR = parallel; PER = perpendicular; 90 = 90° two-gage strain rosette; 45 = 45° three-gage strain rosette.

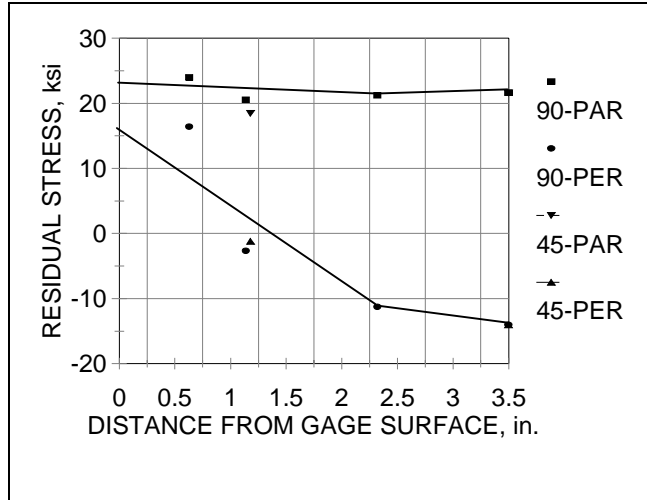


Figure C-9: Calculated residual stress for the heat affected zone core B7B2. PAR = parallel; PER = perpendicular; 90 = 90° two-gage strain rosette; 45 = 45° three-gage strain rosette.

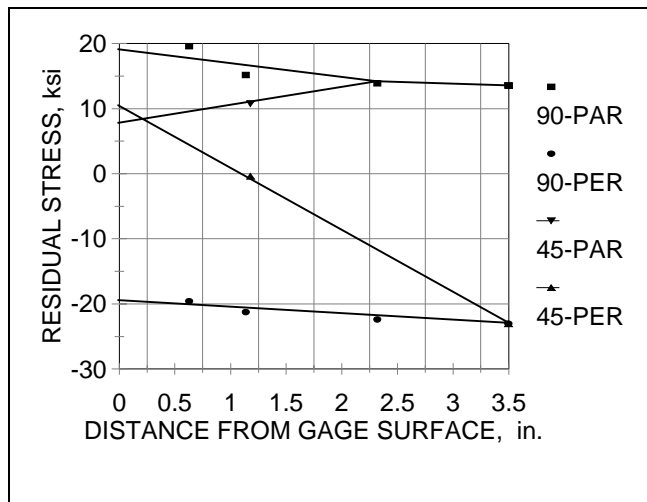


Figure C-10: Calculated residual stress for the heat affected zone core D7B1. PAR = parallel; PER = perpendicular; 90 = 90° two-gage strain rosette; 45 = 45° three-gage strain rosette.

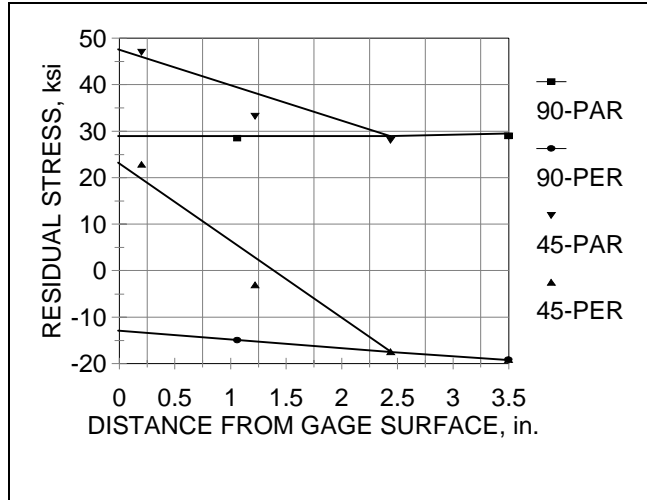


Figure C-11: Calculated residual stress for the heat affected zone core C3B1. PAR = parallel; PER = perpendicular; 90 = 90° two-gage strain rosette; 45 = 45° three-gage strain rosette.

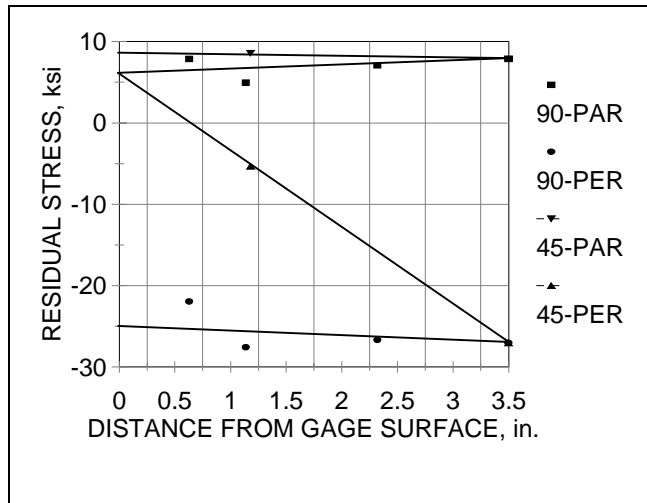


Figure C-12: Calculated residual stress for the heat affected zone core C7B1. PAR = parallel; PER = perpendicular; 90 = 90° two-gage strain rosette; 45 = 45° three-gage strain rosette.

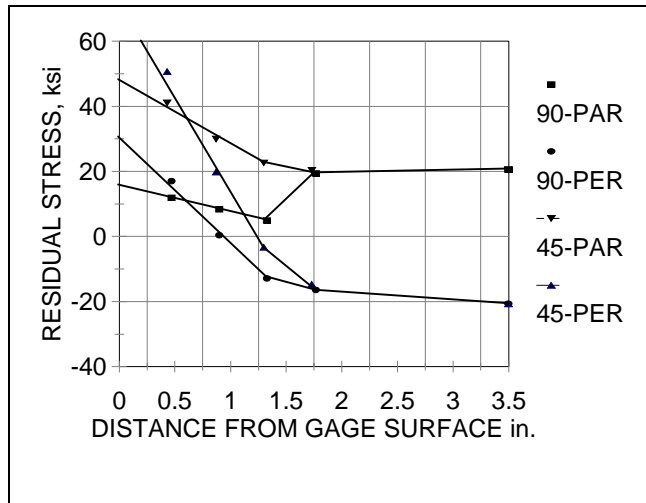


Figure C-13: Calculated residual stress for the heat affected zone core D3B2. PAR = parallel; PER = perpendicular; 90 = 90° two-gage strain rosette; 45 = 45° three-gage strain rosette.